

# **Real-Time Cloud Simulation and Rendering**

by  
Mark Jason Harris

A dissertation submitted to the faculty of the University of North Carolina at Chapel Hill in partial fulfillment of the requirements for the degree of Doctor of Philosophy in the Department of Computer Science.

Chapel Hill  
2003

Approved by:

---

Anselmo Lastra, Advisor

---

Gary Bishop, Reader

---

Ming C. Lin, Reader

---

David Leith, Reader

---

Frederick P. Brooks, Jr., Committee Member



© 2003  
Mark Jason Harris  
ALL RIGHTS RESERVED



## ABSTRACT

**MARK JASON HARRIS: Real-Time Cloud Simulation and Rendering.**  
**(Under the direction of Anselmo Lastra.)**

Clouds are a ubiquitous, awe-inspiring, and ever-changing feature of the outdoors. They are an integral factor in Earth’s weather systems, and a strong indicator of weather patterns and changes. Their effects and indications are important to flight and flight training. Clouds are an important component of the visual simulation of any outdoor scene, but the complexity of cloud formation, dynamics, and light interaction makes cloud simulation and rendering difficult in real time. In an interactive flight simulation, users would like to fly in and around realistic, volumetric clouds, and to see other aircraft convincingly pass within and behind them. Ideally, simulated clouds would grow and disperse as real clouds do, and move in response to wind and other forces. Simulated clouds should be realistically illuminated by direct sunlight, internal scattering, and reflections from the sky and the earth below. Previous real-time techniques have not provided users with such experiences.

I present a physically-based, visually-realistic cloud simulation suitable for interactive applications such as flight simulators. Clouds in the system are modeled using partial differential equations describing fluid motion, thermodynamic processes, buoyant forces, and water phase transitions. I also simulate the interaction of clouds with light, including self-shadowing and multiple forward light scattering. I implement both simulations—dynamic and radiometric—entirely on programmable floating point graphics hardware. The speed and parallelism of graphics hardware enables simulation of cloud dynamics in real time. I exploit the relatively slow evolution of clouds in calm skies to enable interactive visualization of the simulation. The work required to simulate a single time step is automatically spread over many frames while the user views the results of the previous time step. I use dynamically-generated impostors to accelerate cloud rendering. These techniques enable incorporation of realistic, simulated clouds into real applications without sacrificing interactivity.

Beyond clouds, I also present general techniques for using graphics hardware to simulate dynamic phenomena ranging from fluid dynamics to chemical reaction-diffusion. I demonstrate that these simulations can be executed faster on graphics hardware than on traditional CPUs.



# ACKNOWLEDGMENTS

I would like to thank Anselmo Lastra, who is always available and attentive, and has patiently guided me through the steps of my Ph.D. I thank him for being a great advisor, teacher, and friend. Anselmo convinced me that my initial work on clouds was a good start at a Ph.D. topic. Without his honest encouragement I may have left graduate school much earlier.

I thank my committee—Professors Fred Brooks, Gary Bishop, David Leith, Ming Lin, and Parker Reist—for their feedback and for many enlightening discussions. I thank Parker Reist for many interesting conversations about clouds and light scattering, and David Leith for later filling in for Professor Reist. I also thank Dinesh Manocha for his guidance, especially during my first year at UNC as part of the Walkthrough Group. I would not have completed this work without Fred Brooks, Mary Whitton, and the Effective Virtual Environments group, who were kind enough to let me “wildcat” with research outside of the group’s primary focus.

I began working on cloud rendering at iROCK Games during an internship in the summer and fall of 2000. Robert Stevenson gave me the task of creating realistic, volumetric clouds for the game *Savage Skies* (iROCK Games, 2002). I thank Robert and the others who helped me at iROCK, including Brian Stone, Wesley Hunt, and Paul Rowan.

NVIDIA Corporation has given me wonderful help and support over the past two years, starting with an internship in the Developer Technology group during the summer of 2001, followed by two years of fellowship support. I also thank everyone from NVIDIA who provided help, especially John Spitzer, David Kirk, Steve Molnar, Chris Wynn, Sébastien Dominé, Greg James, Cass Everritt, Ashu Rege, Simon Green, Jason Allen, Jeff Juliano, Stephen Ehmann, Pat Brown, Mike Bunnell, Randy Fernando, and Chris Seitz. Also, Section 4.2, which will appear as an article in (Fernando, 2004), was edited by Randy Fernando, Simon Green, and Catherine Kilkenny, and Figures 4.2, 4.3, 4.4, 4.5, and 4.6 were drawn by Spender Yuen.

Discussions with researchers outside of UNC have been enlightening. I have enjoyed conversations about general purpose computation on GPUs with Nolan Goodnight, Cliff Woolley, and Dave Luebke of the University of Virginia, Aaron Lefohn of the University of Utah, and Tim Purcell of Stanford University. Recently, Kirk Riley of Purdue University helped me with scattering phase function data and the *MiePlot* software (Laven, 2003).

I am especially thankful for my fellow students. On top of being great friends, they have been a constant source of encouragement and creative ideas. Rui Bastos gave me help with global illumination as well as general guidance over the years. Bill Baxter, Greg Coombe, and Thorsten Scheuermann collaborated with me on two of the papers that became parts of this dissertation. Some students were my teachers as much as they were my classmates. I can always turn to Bill Baxter for help with fluid dynamics and numerical methods. Wesley Hunt is an expert programmer and has been helpful in answering many software engineering questions. Sharif Razzaque provides creative insight with a side of goofiness.

Computer science graduate students at UNC would have a rough time without the daily help of the staff of our department. I am grateful for the support of these people, especially Janet Jones, David Harrison, Sandra Neely, Tim Quigg, Karen Thigpen, and the department facilities staff.

The research reported in this dissertation was supported in parts by an NVIDIA Fellowship and funding from iROCK Games, The Link Foundation, NIH National Center for Research Resources grant P41 RR 02170, Department of Energy ASCI program, National Science Foundation grants ACR-9876914, IIS-0121293, and ACI-0205425, Office of Naval Research grant N00014-01-1-0061, and NIH National Institute of Biomedical Imaging and Bioengineering grant P41 EB-002025.

My friends in Chapel Hill helped me maintain sanity during stressful times. Bill Baxter, Mike Brown, Greg Coombe, Scott Cooper, Caroline Green, David Marshburn, Samir Naik, Andrew Nashel, Chuck Pisula, Sharif Razzaque, Stefan Sain, Alicia Tribble, Kelly Ward, and Andrew Zaferakis helped ensure that no matter how hard I worked, I played just as hard.

Finally, I thank my parents, Jay and Virginia Harris, who inspire me with their dedication, attention to detail, and ability to drop everything and go to the beach.

# Contents

<b>List of Figures</b>	<b>xiii</b>
<b>List of Tables</b>	<b>xv</b>
<b>List of Abbreviations</b>	<b>xvii</b>
<b>List of Symbols</b>	<b>xix</b>
<b>1 Introduction</b>	<b>1</b>
1.1 Overview . . . . .	2
1.1.1 Cloud Dynamics Simulation . . . . .	3
1.1.2 Cloud Radiometry Simulation . . . . .	3
1.1.3 Efficient Cloud Rendering . . . . .	4
1.1.4 Physically-based Simulation on GPUs . . . . .	4
1.2 Thesis . . . . .	5
1.3 Organization . . . . .	6
<b>2 Cloud Dynamics and Radiometry</b>	<b>8</b>
2.1 Cloud Dynamics . . . . .	9
2.1.1 The Equations of Motion . . . . .	10
2.1.2 The Euler Equations . . . . .	12
2.1.3 Ideal Gases . . . . .	12
2.1.4 Parcels and Potential Temperature . . . . .	13
2.1.5 Buoyant Force . . . . .	14
2.1.6 Environmental Lapse Rate . . . . .	14
2.1.7 Saturation and Relative Humidity . . . . .	15
2.1.8 Water Continuity . . . . .	16
2.1.9 Thermodynamic Equation . . . . .	16

2.1.10	Dynamics Model Summary . . . . .	18
2.2	Cloud Radiometry . . . . .	19
2.2.1	Absorption, Scattering, and Extinction . . . . .	19
2.2.2	Optical Properties . . . . .	19
2.2.3	Single and Multiple Scattering . . . . .	20
2.2.4	Optical Depth and Transparency . . . . .	21
2.2.5	Phase Function . . . . .	21
2.2.6	Light Transport . . . . .	23
2.3	Summary . . . . .	28
<b>3</b>	<b>Related Work</b>	<b>29</b>
3.1	Cloud Modeling . . . . .	29
3.1.1	Particle Systems . . . . .	30
3.1.2	Metaballs . . . . .	31
3.1.3	Voxel Volumes . . . . .	31
3.1.4	Procedural Noise . . . . .	32
3.1.5	Textured Solids . . . . .	32
3.2	Cloud Dynamics Simulation . . . . .	32
3.3	Light Scattering and Cloud Radiometry . . . . .	35
3.3.1	Spherical Harmonics Methods . . . . .	35
3.3.2	Finite Element Methods . . . . .	37
3.3.3	Discrete Ordinates . . . . .	38
3.3.4	Monte Carlo Integration . . . . .	39
3.3.5	Line Integral Methods . . . . .	40
<b>4</b>	<b>Physically-Based Simulation on Graphics Hardware</b>	<b>43</b>
4.1	Why Use Graphics Hardware? . . . . .	44
4.1.1	Classes of GPUs . . . . .	46
4.1.2	General-Purpose Computation on GPUs . . . . .	47
4.2	Fluid Simulation on the GPU . . . . .	49
4.2.1	The Navier-Stokes Equations . . . . .	50
4.2.2	A Brief Vector Calculus Review . . . . .	51
4.2.3	Solving the Navier-Stokes Equations . . . . .	53
4.2.4	Implementation . . . . .	59
4.2.5	Performance . . . . .	68
4.2.6	Applications . . . . .	69

4.2.7	Extensions . . . . .	72
4.2.8	Vorticity Confinement . . . . .	72
4.3	Simulation Techniques for DX8 GPUs . . . . .	73
4.3.1	CML and Related Work . . . . .	75
4.3.2	Common Operations . . . . .	77
4.3.3	State Representation and Storage . . . . .	79
4.3.4	Implementing CML Operations . . . . .	79
4.3.5	Numerical Range of CML Simulations . . . . .	81
4.3.6	Results . . . . .	82
4.3.7	Discussion of Precision Limitations . . . . .	88
4.4	Summary . . . . .	89
<b>5</b>	<b>Simulation of Cloud Dynamics</b>	<b>91</b>
5.1	Solving the Dynamics Equations . . . . .	92
5.1.1	Fluid Flow . . . . .	92
5.1.2	Water Continuity . . . . .	93
5.1.3	Thermodynamics . . . . .	93
5.2	Implementation . . . . .	94
5.3	Hardware Implementation . . . . .	95
5.4	Flat 3D Textures . . . . .	96
5.4.1	Vectorized Iterative Solvers . . . . .	97
5.5	Interactive Applications . . . . .	100
5.5.1	Simulation Amortization . . . . .	100
5.6	Results . . . . .	101
5.7	Summary . . . . .	104
<b>6</b>	<b>Cloud Illumination and Rendering</b>	<b>107</b>
6.1	Cloud Illumination Algorithms . . . . .	107
6.1.1	Light Scattering Illumination . . . . .	108
6.1.2	Validity of Multiple Forward Scattering . . . . .	109
6.1.3	Computing Multiple Forward Scattering . . . . .	113
6.1.4	Eye Scattering . . . . .	114
6.1.5	Phase Function . . . . .	115
6.1.6	Cloud Rendering Algorithms . . . . .	116
6.2	Efficient Cloud Rendering . . . . .	126
6.2.1	Head in the Clouds . . . . .	128

6.2.2	Objects in the Clouds . . . . .	128
6.3	Results . . . . .	131
6.3.1	Impostor Performance . . . . .	131
6.3.2	Illumination Performance . . . . .	132
6.4	Summary . . . . .	132
<b>7</b>	<b>Conclusion</b>	<b>133</b>
7.1	Limitations and Future Work . . . . .	134
7.1.1	Cloud Realism . . . . .	134
7.1.2	Creative Control . . . . .	138
7.1.3	GPGPU and Other phenomena . . . . .	139
<b>Bibliography</b>		<b>141</b>

# List of Figures

1.1	Interactive flight through clouds at sunset. . . . .	7
1.2	Simulated cumulus clouds roll above a valley. . . . .	7
2.1	Definition of scattering angle. . . . .	22
2.2	An example of strong forward scattering from a water droplet. . . . .	24
2.3	Droplet size spectra in cumulus clouds. . . . .	25
2.4	Light transport in clouds. . . . .	27
4.1	Historical performance comparison of CPUs and GPUs. . . . .	45
4.2	GPU fluid simulator results. . . . .	49
4.3	Fluid simulation grid. . . . .	51
4.4	Computing fluid advection. . . . .	57
4.5	Updating grid boundaries and interior. . . . .	62
4.6	Boundary update mechanism. . . . .	68
4.7	2D fluid simulation performance comparison. . . . .	70
4.8	3D coupled map lattice simulations. . . . .	74
4.9	2D coupled map lattice boiling simulation. . . . .	74
4.10	Mapping of CML operations to graphics hardware. . . . .	80
4.11	Using dependent texturing to compute arbitrary functions. . . . .	81
4.12	CMLlab: an interative framework for constructing CML simulations. . . . .	83
4.13	A 3D CML boiling simulation. . . . .	83
4.14	A 2D CML simulation of Rayleigh-Bénard convection. . . . .	84
4.15	Reaction-diffusion in 3D. . . . .	84
4.16	A variety of 2D reaction diffusion results. . . . .	89
4.17	Reaction-diffusion used to create a dynamic bump-mapped disease texture. . . . .	90
5.1	2D cloud simulation sequence. . . . .	93
5.2	Flat 3D Texture layout. . . . .	96
5.3	Vectorized Red-Black grid. . . . .	98
5.4	Interactive flight through simulated clouds in SkyWorks. . . . .	98
5.5	2D cloud simulation performance comparison. . . . .	105
5.6	3D cloud simulation performance comparison. . . . .	106

6.1	Accuracy of the multiple forward scattering approximation. . . . .	110
6.2	Clouds rendered with single scattering. . . . .	111
6.3	Clouds rendered with multiple forward scattering. . . . .	111
6.4	Clouds rendered with isotropic scattering. . . . .	112
6.5	Clouds rendered with anisotropic scattering. . . . .	112
6.6	Approximating skylight with multiple light sources. . . . .	121
6.7	An oriented light volume (OLV). . . . .	121
6.8	Dynamically generated cloud impostors. . . . .	129
6.9	Impostor translation error metric. . . . .	129
6.10	Impostor splitting. . . . .	130
6.11	Impostor performance chart. . . . .	130

# List of Tables

2.1	Constant values and user-specified dynamics parameters. . . . .	18
3.1	A categorization of previous work in computer graphics on clouds. . . . .	30
4.1	Vector calculus operators. . . . .	52
4.2	CML boiling simulation performance . . . . .	86
5.1	Iterative solver convergence comparison. . . . .	99
5.2	2D cloud simulation performance. . . . .	101
5.3	3D cloud simulation performance. . . . .	102
5.4	Advection cost comparison. . . . .	103



## List of Abbreviations

<b>CCN</b>	Cloud Condensation Nuclei
<b>GPU</b>	Graphics Processing Unit
<b>GPGPU</b>	General-Purpose Computation on GPUs
<b>OLV</b>	Oriented Light Volume
<b>RGBA</b>	Red, Green, Blue, Alpha



# List of Symbols

## Cloud dynamics symbols

$\alpha$	Specific volume, page 16
$\delta x$	Grid spacing
$\Gamma$	Lapse rate, see Equation (2.11), page 15
$\hat{p}$	Standard pressure, page 13
$\mathbb{P}$	Helmholtz-hodge projection operator, page 54
$\nu$	Kinematic viscosity, page 11
$\Pi$	Exner Function, see Equation (2.8)
$\rho$	Density
$\theta$	Potential temperature, see Equation (2.8)
$\theta_v$	Virtual potential temperature, page 14
$\theta_{v_0}$	Reference virtual potential temperature, page 14
$\vec{F}$	External forces, page 11
$\vec{f}_{vc}$	Vorticity confinement force, see Equation (4.17), page 72
$\vec{x}$	Spatial position
$\vec{\Psi}$	Normalized vorticity gradient field, page 72
$\vec{\psi}$	Vorticity, page 72
$\vec{u}$	Velocity

$B$	Buoyancy magnitude, see Equation (2.10), page 14
$C$	Condensation rate, see Equation (2.14), page 16
$c_p$	specific heat capacity of dry air at constant pressure, page 13
$c_v$	specific heat capacity of dry air at constant volume, page 13
$dQ$	Heating rate, see Equation (2.15), page 16
$e_s$	Saturation water vapor pressure, see Equation (2.12), page 15
$g$	Gravitational acceleration
$L$	Latent heat of vaporization of water, page 17
$p$	Air pressure
$q_c$	Condensed cloud water mixing ratio
$q_H$	Hydrometeor mass mixing ratio, page 14
$q_s$	Saturation water vapor mixing ratio, see Equation (2.13), page 16
$q_v$	Water vapor mixing ratio
$R$	Ideal gas constant, page 12
$R_d$	Ideal gas constant for dry air, page 12
$RH$	Relative humidity, page 15
$T$	Temperature
$t$	Time
$T_v$	Virtual temperature, see Equation (2.4), page 12
$z$	Altitude

### Cloud radiometry symbols

$\alpha$	Opacity, page 21
$\eta$	Material number density

$\lambda$	Light wavelength
$\sigma_a$	Particle absorption cross section, page 20
$\sigma_s$	Particle scattering cross section
$\tau$	Optical Depth, see Equation (2.19), page 21
$\varpi$	Single scattering albedo, page 20
$\vec{\omega}$	Light direction
$K$	Extinction coefficient, page 19
$K_a$	Absorption coefficient, page 20
$K_s$	Scattering coefficient, page 20
$L$	Radiance, page 24
$P$	Phase function, page 22
$P_{HG}$	Henyey-Greenstein phase function, see Equation (2.22), page 23
$P_{iso}$	Isotropic phase function, see Equation (2.22), page 24
$P_{ray}$	Rayleigh phase function, see Equation (2.21), page 23
$T$	Transmittance, see Equation (2.20), page 21



# Chapter 1

## Introduction

If Clouds were the mere result of the condensation of Vapour in the masses of atmosphere which they occupy, if their variations were produced by the movements of the atmosphere alone, then indeed might the study of them be deemed an useless pursuit of shadows, an attempt to describe forms which, being the sport of winds, must be ever varying, and therefore not to be defined... But the case is not so with clouds...

So began Luke Howard, the “Godfather of the Clouds”, in his ground-breaking 1802 essay on the classification of the forms of clouds (Howard, 1804). Howard’s classification system—most noted for its three main classes *cirrus*, *stratus*, and *cumulus*—is still in use today, and is well-known even among lay people. Howard’s work and its influence on the world exemplify the importance of clouds to humankind. Long before his time, people had looked to the clouds as harbingers of changing weather, but Howard knew that understanding and predicting changes in the weather required a better understanding of clouds. This understanding could not be improved without a concrete yet flexible nomenclature with which clouds could be discussed among scientists. Howard’s contemporaries were immediately taken with his classification, and his fame quickly expanded outside of the circle of amateur scientists to which he presented his work. His fans included the landscape painter John Constable and Johann Wolfgang von Goethe, who immortalized Howard and his classification in a poem, *Howards Ehrengedächtnis* (“In Honor of Howard”) (Hamblyn, 2001).

As Howard, Goethe, and Constable knew so well, clouds are a ubiquitous feature of our world. They provide a fascinating dynamic backdrop to the outdoors, creating an endless array of formations and patterns. As with stars, observers often attribute fanciful creatures to the shapes they form; but this game is endless, because unlike constellations, cloud shapes change within minutes. Beyond their visual fascination,

clouds are also an integral factor in Earth’s weather systems. Clouds are the vessels from which rain pours, and the shade they provide can cause temperature changes below. The vicissitudes of temperature and humidity that create clouds also result in tempestuous winds and storms. Their stunning beauty, physical and visual complexity, and pertinence to weather has made clouds an important area of study for meteorology, physics, art, and computer graphics.

Cloud realism is especially important to flight simulation. Nearly all pilots these days spend time training in flight simulators. To John Wojnaroski, a former USAF fighter pilot and an active developer of the open-source *FlightGear* Flight Simulator project (*FlightGear*, 2003), realistic clouds are an important part of flight that is missing from current professional simulators (Wojnaroski, 2003):

One sensation that clouds provide is the sense of motion, both in the sim and in real life. Not only are clouds important, they are absolutely essential to give the sky substance. Like snowflakes, no two clouds are alike and when you talk to folks involved in soaring<sup>1</sup> you realize that clouds are the fingerprints that tell you what the air is doing.

The complexity of cloud formation, dynamics, and light interaction makes cloud simulation and rendering difficult in real time. In an interactive flight simulation, users would like to fly in and around realistic, volumetric clouds, and to see other aircraft convincingly pass within and behind them. Ideally, simulated clouds would grow and disperse as real clouds do; get blown by the wind; and move in response to forces induced by passing aircraft. Simulated clouds should be realistically illuminated by direct sunlight, internal scattering, and reflections from the sky and the earth below. Previous real-time techniques have not provided users with such experiences.

## 1.1 Overview

My research goal has been to produce a system that allows users to fly through dynamic, realistically illuminated clouds. Thus, the two main functional goals of my research are cloud simulation and cloud rendering. Cloud simulation itself has two components: cloud dynamics simulation and cloud radiometry simulation—to use Luke Howard’s words, the “sport of winds” and the “pursuit of shadows”. These functional goals, along with the use of graphics hardware as a tool to achieve them, lead to a natural

---

<sup>1</sup>Soaring, also called gliding, is motorless flight.

decomposition of my work into four areas: cloud dynamics simulation, cloud radiometry simulation, efficient cloud rendering, and physically-based simulation on graphics hardware.

### 1.1.1 Cloud Dynamics Simulation

Clouds are the visible manifestation of complex and invisible atmospheric processes. The atmosphere is a fluid. *Fluid dynamics* therefore governs the motion of the air, and as a result, of clouds. Clouds are composed of small particles of liquid water carried by currents in the air. The water in clouds condenses from water vapor that is carried up from the earth to higher altitudes, and eventually evaporates. The balance of evaporation and condensation is called *water continuity*. The convective currents that carry water vapor and other gases are caused by temperature variations in the atmosphere, and can be described using *thermodynamics*.

Fluid dynamics, thermodynamics, and water continuity are the major processes that must be modeled in order to simulate realistic clouds. The physics of clouds are complex, but by breaking them down into simple components, accurate models are achievable. In this dissertation I present a realistic model for the simulation of clouds based on these processes. I take advantage of the parallelism and flexibility of modern graphics processors to implement interactive simulation. I also describe a technique, *simulation amortization*, for improving application performance by spreading the work required for each simulation step over multiple rendering frames.

### 1.1.2 Cloud Radiometry Simulation

Clouds absorb very little light energy. Instead, each water droplet reflects, or *scatters* nearly all incident light. Clouds are composed of millions of these tiny water droplets. Nearly every photon that enters a cloud is scattered many times before it emerges. The light exiting the cloud reaches your eyes, and is therefore responsible for the cloud's appearance. Accurate generation of images of clouds requires simulation of the *multiple light scattering* that occurs within them. The complexity of the scattering makes exhaustive simulation impossible. Instead, approximations must be used to reduce the cost of the simulation.

I present a useful approximation for multiple scattering that works well for clouds. This approximation, called *multiple forward scattering* takes advantage of the fact that water droplets scatter light mostly in the *forward* direction—the direction in which it

was traveling before interaction with the droplet. This approximation leads to simple algorithms that take advantage of graphics hardware features, resulting in fast cloud illumination simulation.

### 1.1.3 Efficient Cloud Rendering

After efficiently computing the dynamics and illumination of clouds, there remains the task of generating a cloud image. The translucent nature of clouds means that they cannot be represented as simple geometric “shells”, like the polygonal models commonly used in computer graphics. Instead, a volumetric representation must be used to capture the variations in density within the cloud. Rendering such volumetric models requires much computation at each pixel of the image. This computation can result in excessive rendering times for each frame.

In order to make cloud rendering feasible for interactive applications, I have developed a technique for amortizing the rendering cost of clouds over multiple frames. The technique that I use borrows the concept of *dynamically-generated impostors* from traditional geometric model rendering. A dynamically-generated impostor is an image of an object. The image is generated at a given viewpoint, and then rendered in place of the object until movement of the viewpoint introduces excessive error in the image. The result is that the cost of rendering the image is spread over many frames. In this dissertation I show that impostors are especially useful for accelerating cloud rendering. I also introduce some modifications to traditional impostors that allow them to be used even when objects such as aircraft pass through clouds, and when the user’s viewpoint is inside a cloud.

### 1.1.4 Physically-based Simulation on GPUs

Central to my research is the use of graphics hardware to perform the bulk of the computation. The recent rapid increase in the speed and programmability of graphics processors has enabled me to use graphics processing units (GPUs) for more than just rendering clouds. I perform all cloud simulation—both dynamics and radiometry—entirely on the GPU.

Using the GPU for simulation does more than just free the CPU for other computations; it results in an overall faster simulation. In this dissertation I demonstrate that GPU implementations of a variety of physically-based simulations outperform implementations that perform all computation on the CPU. Also, because my goal is to

render the results of the simulation, performing simulation on the rendering hardware obviates any cost for transferring the results to GPU memory. General-purpose computation on GPUs has recently become an active research area in computer graphics. Section 4.1.2 provides an overview of much of the recent and past work in the area.

## 1.2 Thesis

My thesis is

*Realistic, dynamic clouds can be simulated and rendered in real time using efficient algorithms executed entirely on programmable graphics processors.*

In support of my thesis, I have investigated and implemented real-time cloud illumination techniques as well as cloud simulation techniques to produce dynamic models of realistic clouds. I have exploited the parallelism of graphics hardware to implement efficient simulation and rendering. To support my goal of interactive visualization, I have also developed techniques for amortizing simulation and rendering costs over multiple rendering frames. The end result is a fast, visually realistic cloud simulation system suitable for integration with interactive applications. To my knowledge, my work is the first to perform simulation of both cloud dynamics and radiometry in an interactive application (See Table 3.1). Figures 1.1 and 1.2 show examples of the results of my work.

Simulation on graphics hardware results in high performance—my 3D cloud simulation operates at close to 30 iterations per second on a  $32 \times 32 \times 32$  grid, and about 4 iterations per second on a  $64 \times 64 \times 64$  grid. Because the components of the simulation are stable for large time steps, I can use an iteration time step size of a few seconds. Therefore, I am able to simulate the dynamics of clouds *faster* than real time. This, when combined with the smooth interactive frame rates I achieve through simulation amortization, supports my thesis goal of real-time cloud dynamics simulation.

Using the multiple forward scattering approximation, I have developed a graphics hardware algorithm for computing the illumination of the volumetric cloud that results from my cloud dynamics simulation. This radiometry simulation requires only 20–50 ms to compute. By applying the simulation amortization approach to both the dynamics and radiometry simulations, I am able to simulate cloud dynamics and radiometry in real time.

To accelerate cloud rendering, I employ dynamically generated impostors. Impostors allow an image of a cloud to be re-used for several rendering frames. This reduces the overall rendering cost per frame, allowing the application to run at high frame rates. Through the combination of these efficient algorithms executed on graphics hardware, I have achieved my thesis goals of real-time simulation and rendering of realistic clouds.

### 1.3 Organization

This dissertation is organized as follows. The next chapter provides a brief introduction to the physical principles of cloud dynamics and radiometry. Chapter 3 describes previous work in cloud rendering and simulation. Chapter 4 presents techniques I have developed for implementing physically-based simulations on graphics hardware. It also describes in detail the solution of the Navier-Stokes equations for incompressible fluid flow. Chapter 5 extends this fluid simulation to a simulation of cloud dynamics, including thermodynamics and water continuity. Chapter 6 presents the multiple forward scattering approximation that I use to simulate cloud radiometry, and then describes efficient algorithms for computing the illumination of both static and dynamic cloud models. Finally, Chapter 7 concludes and describes directions for future work.



Figure 1.1: This image, captured in my *SkyWorks* cloud rendering engine, shows a scene from interactive flight through static particle-based clouds at sunset. Efficient cloud rendering techniques enable users to fly around and through clouds like these at over 100 frames per second.

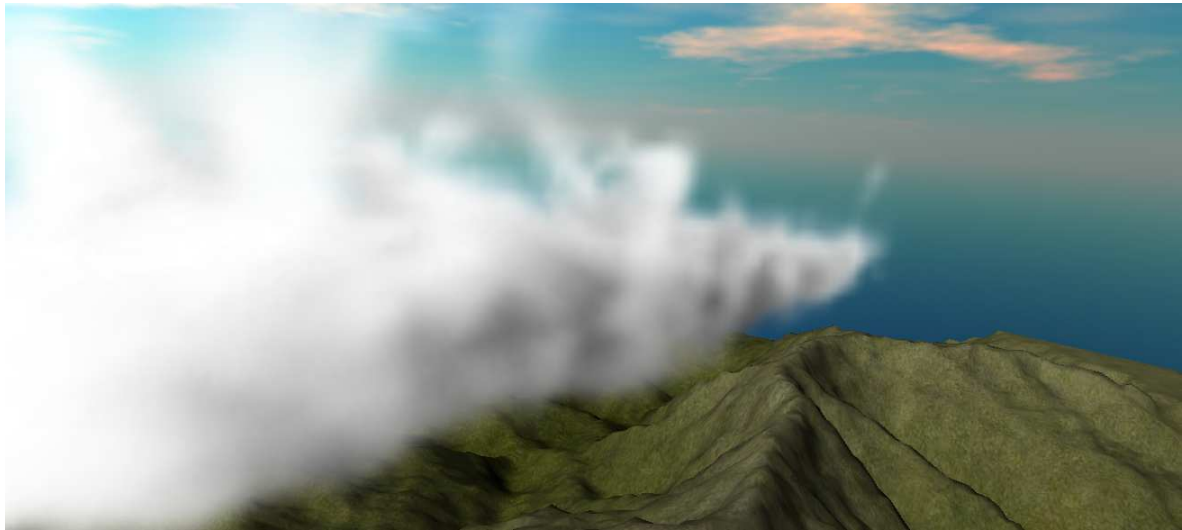


Figure 1.2: Simulated cumulus clouds roll above a valley. This simulation, running on a  $64 \times 32 \times 32$  grid, can be viewed at over 40 frames per second while the simulation updates at over 10 iterations per second.



# Chapter 2

## Cloud Dynamics and Radiometry

Realistic visual simulation of clouds requires simulation of two distinct aspects of clouds in nature: dynamics and radiometry. *Cloud dynamics* includes the motion of air in the atmosphere, the condensation and evaporation of water, and the exchanges of heat that occur as a result of both of these. *Cloud radiometry* is the study of how light interacts with clouds. Both cloud dynamics and radiometry are sufficiently complex that efficient simulation is difficult without the use of simplifying assumptions. In this chapter I present the mathematics of cloud dynamics and radiometry, and propose some useful simplifications that enable efficient simulation. My intent is to provide a brief introduction to the necessary physical concepts and equations at a level useful to computer scientists. Readers familiar with these subjects may prefer to skip or skim this chapter. In most cases, I provide only equations that I use in my simulation models, and omit extraneous details.

### 2.1 Cloud Dynamics

The dynamics of cloud formation, growth, motion and dissipation are complex. In the development of a cloud simulation, it is important to understand these dynamics so that good approximations can be chosen that allow efficient implementation without sacrificing realism. The outcome of the following discussion is a system of partial differential equations that I solve at each time step of my simulation using numerical integration. In Section 2.1.10, I summarize the model to provide the reader a concise listing of the equations. All of the equations that make up my cloud dynamics model originate from the atmospheric physics literature. All can be found in most cloud and atmospheric dynamics texts, including (Andrews, 2000; Houze, 1993; Rogers and Yau,

1989). I refer the reader to these books for much more detailed information.

The basic quantities<sup>1</sup> necessary to simulate clouds are the velocity,  $\vec{u} = (u, v, w)$ , air pressure,  $p$ , temperature,  $T$ , water vapor,  $q_v$ , and condensed cloud water,  $q_c$ . These water content variables are mixing ratios—the mass of vapor or liquid water per unit mass of air. The visible portion of a cloud is its condensed water,  $q_c$ . Therefore this is the desired output of a cloud simulation for my purposes. Cloud simulation requires a system of equations that models cloud dynamics in terms of these variables. These equations are the equations of motion, the thermodynamic equation, and the water continuity equations.

### 2.1.1 The Equations of Motion

To simplify computation, I assume that air in the atmosphere (and therefore any cloud it contains) is an incompressible, homogeneous fluid. A fluid is incompressible if the volume of any sub-region of the fluid is constant over time. A fluid is homogeneous if its density,  $\rho$ , is constant in space. The combination of incompressibility and homogeneity means that density is constant in both space and time. These assumptions are common in fluid dynamics, and do not decrease the applicability of the resulting mathematics to the simulation of clouds. Clearly, air is a compressible fluid—if sealed in a box and compressed its density (and temperature) will increase. However the atmosphere cannot be considered a sealed box—air under pressure is free to move. As a result, little compression occurs at the velocities that interest us for cloud dynamics.

I simulate fluids (and clouds) on a regular Cartesian grid with spatial coordinates  $\vec{x} = (x, y, z)$  and time variable  $t$ . The fluid is represented by its velocity field  $\vec{u}(\vec{x}, t) = (dx/dt, dy/dt, dz/dt) = (u(\vec{x}, t), v(\vec{x}, t), w(\vec{x}, t))$  and a scalar pressure field  $p(\vec{x}, t)$ . These fields vary in both space and time. If the velocity and pressure are known for the initial time  $t = 0$ , then the state of the fluid over time can be described by the *Navier-Stokes equations for incompressible flow*.

$$\frac{\partial \vec{u}}{\partial t} = -(\vec{u} \cdot \nabla) \vec{u} - \frac{1}{\rho} \nabla p + \nu \nabla^2 \vec{u} + \vec{F} \quad (2.1)$$

$$\nabla \cdot \vec{u} = 0 \quad (2.2)$$

---

<sup>1</sup>I define each symbol or variable as I come to it. The List of Symbols in the front matter provides references to the point of definition of most symbols.

In Equation (2.1),  $\rho$  is the (constant) fluid density,  $\nu$  is the kinematic viscosity, and  $\vec{F} = (f_x, f_y, f_z)$  represents any external forces that act on the fluid. Equation (2.1) is called the *momentum equation*, and Equation (2.2) is the *continuity equation*. The Navier-Stokes equations can be derived from the conservation principles of momentum and mass, respectively, as shown in (Chorin and Marsden, 1993). Because  $\vec{u}$  is a vector quantity, there are four equations and four unknowns ( $u$ ,  $v$ ,  $w$ , and  $p$ ). The four terms on the right-hand side of Equation (2.1) represent accelerations. I will examine each of them in turn.

## Advection

The velocity of a fluid causes the fluid to transport objects, densities, and other quantities along with the flow. Imagine squirting dye into a moving fluid. The dye is transported, or *advected*, along the fluid's velocity field. In fact, the velocity of a fluid carries itself along just as it carries the dye. The first term on the right-hand side of Equation (2.1) represents this *self-advection* of the velocity field, and is called the advection term.

## Pressure

Because the molecules of a fluid can move around each other, they tend to “squish” and “slosh”. When force is applied to a fluid, it does not instantly propagate through the entire volume. Instead, the molecules close to the force push on those farther away, and pressure builds up. Because pressure is force per unit area, any pressure in the fluid naturally leads to acceleration. (Think of Newton's second law,  $\vec{F} = m\vec{a}$ .) The second term, called the pressure term, represents this acceleration.

## Diffusion

Some fluids are “thicker” than others. For example, molasses and maple syrup flow slowly, but rubbing alcohol flows quickly. We say that thick fluids have a high *viscosity*. Viscosity is a measure of how resistive a fluid is to flow. This resistance results in diffusion of the momentum (and therefore velocity), so the third term is called the diffusion term.

## External Forces

The fourth term of the momentum equation encapsulates acceleration due to external forces applied to the fluid. These forces may be either *local forces* or *body forces*. Local forces are applied to a specific region of the fluid—for example, the force of a fan blowing air. Body forces, such as the force of gravity, apply evenly to the entire fluid.

### 2.1.2 The Euler Equations

Air in Earth's atmosphere has very low viscosity. Therefore, at the scales that interest us, the diffusion term of the momentum equation is negligible, and the motion of air in the atmosphere can be described by the simpler *Euler equations of incompressible fluid motion*.

$$\frac{\partial \vec{u}}{\partial t} = -(\vec{u} \cdot \nabla) \vec{u} - \frac{1}{\rho} \nabla p + B\hat{k} + \vec{F} \quad (2.3)$$

$$\nabla \cdot \vec{u} = 0 \quad (2.4)$$

In these equations I have separated the buoyancy force,  $B\hat{k}$ , from the rest of the external forces,  $\vec{F}$ , because buoyancy is handled separately in my implementation. Buoyancy is described in Section 2.1.5.

### 2.1.3 Ideal Gases

Air is a mixture of several gases, including nitrogen and oxygen (78% and 21% by volume, respectively), and a variety of trace gases. This mixture is essentially uniform over the entire earth and up to an altitude of about 90 km. There are a few gases in the atmosphere whose concentrations vary, including water vapor, ozone, and carbon dioxide. These gases have a large influence on The Earth's weather, due to their effects on radiative transfer and the fact that water vapor is a central factor in cloud formation and atmospheric thermodynamics (Andrews, 2000). All of the gases mentioned above are ideal gases. An ideal gas is a gas that obeys the ideal gas law, which states that at the same pressure,  $p$ , and temperature,  $T$ , any ideal gas occupies the same volume:

$$p = \rho RT, \quad (2.5)$$

where  $\rho$  is the gas density and  $R$  is known as the gas constant. For dry air, this constant is  $R_d = 287 \text{ J kg}^{-1} \text{ K}^{-1}$ . In meteorology, air is commonly treated as a mixture of two ideal gases: “dry air” and water vapor. Together, these are referred to as moist air

(Rogers and Yau, 1989). For moist air, Equation (2.5) can be modified to

$$p = \rho R_d T_v, \quad (2.6)$$

where  $T_v$  is the *virtual temperature*, which is approximated by

$$T_v \approx T (1 + 0.61q_v). \quad (2.7)$$

Virtual temperature accounts for the effects of water vapor,  $q_v$ , on air temperature, and is defined as the temperature that dry air would have if its pressure and density were equal to those of a given sample of moist air.

#### 2.1.4 Parcels and Potential Temperature

A conceptual tool used in the study of atmospheric dynamics is the *air parcel*—a small mass of air that can be thought of as “traceable” relative to its surroundings. The parcel approximation is useful in developing the mathematics of cloud simulation. We can imagine following a parcel throughout its lifetime. As the parcel is warmed at constant pressure, it expands and its density decreases. It becomes buoyant and rises through the cooler surrounding air. Conversely, when a parcel cools, it contracts and its density decreases. It then falls through the warmer surrounding air. When an air parcel changes altitude without a change in heat (not to be confused with temperature), it is said to move *adiabatically*. Because air pressure (and therefore temperature) varies with altitude, the parcel’s pressure and temperature change. The ideal gas law and the laws of thermodynamics can be used to derive Poisson’s equation for adiabatic processes, which relates the temperature and pressure of a gas under adiabatic changes (Rogers and Yau, 1989):

$$\left(\frac{T}{T_0}\right) = \left(\frac{p}{p_0}\right)^\kappa, \quad (2.8)$$

$$\kappa = \frac{R_d}{c_p} = \frac{c_p - c_v}{c_p} \approx 0.286.$$

Here,  $T_0$  and  $p_0$  are initial values of temperature and pressure, and  $T$  and  $p$  are the values after an adiabatic change in altitude. The constants  $c_p = 1005 \text{ J kg}^{-1} \text{ K}^{-1}$  and  $c_v = 718 \text{ J kg}^{-1} \text{ K}^{-1}$  are the specific heat capacities of dry air at constant pressure and volume, respectively.

We can more conveniently account for adiabatic changes of temperature and pres-

sure using the concept of potential temperature. The *potential temperature*,  $\theta$ , of a parcel of air can be defined (using Equation (2.8)) as the final temperature that a parcel would have if it were moved adiabatically from pressure  $p$  and temperature  $T$  to pressure  $\hat{p}$ :

$$\theta = \frac{T}{\Pi} = T \left( \frac{\hat{p}}{p} \right)^\kappa \quad (2.9)$$

$\Pi$  is called the *Exner function*, and the typical value of  $\hat{p}$  is standard pressure at sea level, 100 kPa. Potential temperature is convenient to use in atmospheric modeling because it is constant under adiabatic changes of altitude, while absolute temperature must be recalculated at each altitude.

### 2.1.5 Buoyant Force

Changes in the density of a parcel of air relative to its surroundings result in a buoyant force on the parcel. If the parcel's density is less than the surrounding air, the buoyant force is upward; if the density is greater, the force is downward. Equation (2.5) relates the density of an ideal gas to its temperature and pressure. A common simplification in cloud modeling is to regard the effects of local pressure changes on density as negligible, resulting in the following equation for the buoyant force per unit mass (Houze, 1993):

$$B = g \left( \frac{\theta_v}{\theta_{v_0}} - q_H \right) \quad (2.10)$$

Here,  $g$  is the acceleration due to gravity,  $q_H$  is the mass mixing ratio of *hydrometeors*, which includes all forms of water other than water vapor, and  $\theta_{v_0}$  is the reference virtual potential temperature, usually between 290 and 300 K. In the case of the simple two-state bulk water continuity model to be described in Section 2.1.8,  $q_H$  is just the mixing ratio of liquid water,  $q_c$ .  $\theta_v$  is the virtual potential temperature, which accounts for the effects of water vapor on the potential temperature of air. Virtual potential temperature is approximated (using Equations (2.7) and (2.9)) by  $\theta_v \approx \theta (1 + 0.61q_v)$ .

### 2.1.6 Environmental Lapse Rate

The Earth's atmosphere is in static equilibrium. The so-called hydrostatic balance of the opposing forces of gravity and air pressure results in an exponential decrease of

pressure with altitude (Rogers and Yau, 1989):

$$p(z) = p_0 \left(1 - \frac{z\Gamma}{T_0}\right)^{g/(\Gamma R_d)} \quad (2.11)$$

Here,  $z$  is altitude in meters,  $g$  is gravitational acceleration,  $9.81 \text{ m s}^{-2}$  and  $p_0$  and  $T_0$  are the pressure and temperature at the base altitude. Typically,  $p_0 \approx 100 \text{ kPa}$  and  $T_0$  is in the range 280–310 K. The lapse rate,  $\Gamma$ , is the rate of decrease of temperature with altitude. In the Earth's atmosphere, temperature decreases approximately linearly with height in the *troposphere*, which extends from sea level to about 15 km (the *tropopause*). Therefore, I assume that  $\Gamma$  is a constant. A typical value for  $\Gamma$  is around  $10 \text{ K km}^{-1}$ . I use Equations (2.9) and (2.11) to compute the environmental temperature and pressure of the atmosphere in the absence of disturbances, and as I describe in Section 2.1.7, compare them to the local temperature and pressure to compute the saturation point of the air.

### 2.1.7 Saturation and Relative Humidity

Cloud water continuously changes phases from liquid to vapor and vice versa. When the rates of condensation and evaporation are equal, air is *saturated*. The water vapor pressure at saturation is called the *saturation vapor pressure*, denoted by  $e_s(T)$ . When the water vapor pressure exceeds the saturation vapor pressure, the air becomes *super-saturated*. Rather than remain in this state, condensation may occur, leading to cloud formation. A useful empirical approximation for saturation vapor pressure is

$$e_s(T) = 611.2 \exp\left(\frac{17.67T}{T + 243.5}\right), \quad (2.12)$$

with  $T$  in  $^{\circ}\text{C}$  and  $e_s(T)$  in Pa. This is the formula for a curve fit to data in standard meteorological tables to within 0.1% over the range  $-30^{\circ}\text{C} \leq T \leq 30^{\circ}\text{C}$  (Rogers and Yau, 1989).

A useful measure of moisture content of air is relative humidity, which is the ratio of water vapor pressure,  $e$ , in the air to the saturation vapor pressure (usually expressed as a percentage):  $RH = e/e_s(T)$ . Because vapor mixing ratio is directly proportional to vapor pressure ( $q_v \approx 0.622e/p$ ), I use the equivalent definition  $RH = q_v/q_{vs}$  (because  $q_{vs} \approx 0.622e_s/p$ ). Combining this with Equation (2.12) results in an empirical

expression for the *saturation vapor mixing ratio*:

$$q_s(T) = \frac{380.16}{p} \exp\left(\frac{17.67T}{T + 243.5}\right). \quad (2.13)$$

### 2.1.8 Water Continuity

I use a simple *Bulk Water Continuity* model as described in (Houze, 1993) to describe the evolution of the water vapor mixing ratio,  $q_v$ , and the condensed cloud water mixing ratio,  $q_c$ . Cloud water is water that has condensed but whose droplets have not grown large enough to precipitate. The water mixing ratios at a given location are affected by both advection and phase changes (from gas to liquid and vice versa). In this model, the rates of evaporation and condensation must be balanced, resulting in the water continuity equation,

$$\frac{\partial q_v}{\partial t} + (\mathbf{u} \cdot \nabla) q_v = - \left( \frac{\partial q_c}{\partial t} + (\mathbf{u} \cdot \nabla) q_c \right) = C, \quad (2.14)$$

where  $C$  is the condensation rate.

### 2.1.9 Thermodynamic Equation

Changes of temperature of an air parcel are governed by the *First Law of Thermodynamics*, which is an expression of conservation of energy. For an ideal gas, the *thermodynamic energy equation* can be written

$$c_v dT + p d\alpha = dQ, \quad (2.15)$$

where  $dQ$  is the heating rate and  $\alpha$  is the specific volume,  $\rho^{-1}$ . The first term in Equation (2.15) is the rate of change of internal energy of the parcel, and the second term is the rate at which work is done by the parcel on its environment (Rogers and Yau, 1989). Equation (2.5) is equivalent to  $p\alpha = R_d T$ . Taking the derivative of both sides results in  $p d\alpha + \alpha dp = R_d dT$ . Using this equation and the fact that  $c_p = R_d + c_v$ , Equation (2.15) becomes

$$c_p dT - \alpha dp = dQ. \quad (2.16)$$

It is helpful to express the thermodynamic energy equation in terms of potential

temperature, because  $\theta$  is the temperature variable that I use in my model. Differentiating both sides of  $T = \Pi\theta$  results in

$$dT = \Pi d\theta + \theta d\Pi = \Pi d\theta + T \frac{d\Pi}{\Pi}.$$

We substitute this into Equation (2.16) and simplify the result using the following steps.

$$\begin{aligned} c_p \Pi d\theta + c_p T \frac{d\Pi}{\Pi} - \alpha dp &= dQ, \\ c_p \Pi d\theta + \frac{c_p \kappa T}{p} dp - \alpha dp &= dQ, \\ c_p \Pi d\theta &= dQ. \end{aligned}$$

The resulting simplified thermodynamic energy equation is

$$d\theta = \frac{1}{c_p \Pi} dQ.$$

While adiabatic motion is a valid approximation for air that is not saturated with water vapor, the potential temperature of saturated air cannot be assumed to be constant. If expansion of a moist parcel continues beyond the saturation point, water vapor condenses and releases latent heat, warming the parcel. A common assumption in cloud modeling is that this latent heating and cooling due to condensation and evaporation are the only non-adiabatic heat sources (Houze, 1993). This assumption results in a simple expression for the change in heat,  $dQ = -L dq_v$ , where  $L$  is the latent heat of vaporization of water,  $2.501 \text{ J kg}^{-1}$  at  $0^\circ\text{C}$  ( $L$  changes by less than 10% within  $\pm 40^\circ\text{C}$ ). In this situation, the following form of the thermodynamic equation can be used:

$$d\theta = \frac{-L}{c_p \Pi} dq_v. \quad (2.17)$$

Because both temperature and water vapor are carried along with the velocity of the air, advection must be taken into account in the thermodynamic equation. The thermodynamic energy equation that I solve in my simulation is

$$\frac{\partial \theta}{\partial t} + (\mathbf{u} \cdot \nabla) \theta = \frac{-L}{c_p \Pi} \left( \frac{\partial q_v}{\partial t} + (\mathbf{u} \cdot \nabla) q_v \right). \quad (2.18)$$

Notice from Equation (2.14) that we can substitute  $-C$  for the quantity in parentheses.

constant	description	value
$\hat{p}$	Standard pressure at sea level	100 kPa
$g$	Gravitational acceleration	9.81 m s <sup>-2</sup>
$R_d$	Ideal gas constant for dry air	287 J kg <sup>-1</sup> K <sup>-1</sup>
$L$	Latent heat of vaporization of water	2.501 J kg <sup>-1</sup>
$c_p$	Specific heat capacity (dry air, constant pressure)	1005 J kg <sup>-1</sup> K <sup>-1</sup>
parameter	description	default / range
$p_0$	Pressure at sea level	100 kPa
$T_0$	Temperature at sea level	280–310 K
$\Gamma$	Temperature lapse rate	10 K km <sup>-1</sup>

Table 2.1: Constant values and user-specified parameters in the cloud dynamics model.

### 2.1.10 Dynamics Model Summary

The three main components of my cloud dynamics model are the Euler equations for incompressible motion, (2.3) and (2.4) (Section 2.1.2); the thermodynamic equation, (2.18) (Section 2.1.9); and the water continuity equation, (2.14) (Section 2.1.8). These equations depend on other equations to compute some of their variable quantities.

The equations of motion depend on buoyant acceleration, Equation (2.10) (Section 2.1.5). The method of solving the equations of motion is given in Chapter 4. The water continuity equations depend on the saturation mixing ratio, which is computed using Equation (2.13) (Section 2.1.7). The equation for saturation mixing ratio depends on the temperature,  $T$ , which must be computed from potential temperature using Equation (2.8) (Section 2.1.4). It also depends on the pressure,  $p$ . Rather than solve for the exact pressure, I assume that local variations are very small<sup>2</sup>, and use Equation (2.11) (Section 2.1.6) to compute the pressure at a given altitude.

The unknowns in the equations are velocity,  $\vec{u}$ , pressure  $p$ , potential temperature,  $\theta$ , water vapor mixing ratio,  $q_v$ , and condensed cloud water mixing ratio,  $q_c$ . Table 2.1 summarizes the constants and user defined parameters in the dynamics model, and chapter 5 discusses the boundary conditions and initial values I use in the simulation.

---

<sup>2</sup>The result of this pressure assumption is that pressure changes due to air motion are not accounted for in phase changes (and therefore thermodynamics). For visual simulation, this is not a big loss, because clouds behave visually realistically despite the omission. Computing the pressure exactly is difficult and expensive. The equations of motion depend on the gradient of the pressure, not its absolute value. The solution method that I use computes pressure accurate to within a constant factor. The gradient is correctly computed, but the absolute pressure cannot be assumed to be accurate.

## 2.2 Cloud Radiometry

Clouds appear as they do because of the way in which light interacts with the matter that composes them. The study of light and its interaction with matter is called Radiometry. In order to generate realistic images of clouds, one needs an understanding of the radiometry of clouds. The visible portions of clouds are made up of many tiny droplets of condensed water. The most common interaction between light and these droplets is light scattering. In this section I define some important radiometry terminology, and present the mathematics necessary to simulate light scattering in clouds and other scattering media.

There are many excellent resources on radiometry and light scattering. The material in this chapter is mostly compiled from (Bohren, 1987; Premože et al., 2003; van de Hulst, 1981).

### 2.2.1 Absorption, Scattering, and Extinction

Once a photon is emitted, one of two fates awaits it when it interacts with matter: absorption and scattering. *Absorption* is the phenomenon by which light energy is converted into another form upon interacting with a medium. For example, black pavement warms in sunlight because it absorbs light and transforms it into heat energy. *Scattering*, on the other hand, can be thought of as an elastic collision between matter and a photon in which the direction of the photon may change. Both scattering and absorption remove energy from a beam of light as it passes through a medium, attenuating the beam. *Extinction* describes the total attenuation of light energy by absorption and scattering. The amount of extinction in a medium is measured by its extinction coefficient,  $K = K_s + K_a$ , where  $K_s$  is the scattering coefficient and  $K_a$  is the absorption coefficient (defined in Section 2.2.2). Any light that interacts with a medium undergoes either scattering or absorption. If it does not interact, then it is *transmitted*. Extinction (and therefore scattering and absorption) is proportional to the number of particles per unit volume. Non-solid media that scatter and absorb light are commonly called *participating media*.

### 2.2.2 Optical Properties

Several optical properties determine how any medium interacts with light, and thus how it appears to an observer. These optical properties, which may vary spatially

( $\vec{x} = (x, y, z)$  represents spatial position), depend on physical properties such as the material number density,  $\eta(\vec{x})$  (the number of particles per unit volume), the phase function (see Section 2.2.5), and the absorption and scattering cross sections of particles in the medium,  $\sigma_a$  and  $\sigma_s$ , respectively. The cross sections are proportional (but not identical) to the physical cross sections of particles, and thus have units of area. The scattering cross section accounts for the fraction of the total light incident on a particle that is scattered, and the absorption cross section accounts for the fraction that is absorbed. These cross sections depend on the type and size of particles.

Computing scattering for every particle in a medium is intractable. Instead, coefficients are used to describe the bulk optical properties at a given location in a medium. The scattering coefficient describes the average scattering of a medium, and is defined  $K_s(\vec{x}) = \sigma_s \eta(\vec{x})$ . Similarly, the absorption coefficient is  $K_a(\vec{x}) = \sigma_a \eta(\vec{x})$ . These coefficients assume that either the cross sections of particles in the medium are uniform, or that any variation is accounted for (perhaps via statistical methods) in  $\sigma_s$  and  $\sigma_a$ . The coefficients are measured in units of inverse length ( $\text{cm}^{-1}$  or  $\text{m}^{-1}$ ), and therefore their reciprocals have units of length and may be interpreted as the mean free paths for scattering and absorption. In other words  $1/\sigma_s$  is related to the average distance between scattering events. Another interpretation is that the absorption (scattering) coefficient is the probability of absorption (scattering) per unit length traveled by a photon in the medium.

The single scattering albedo  $\varpi = K_s/(K_s + K_a)$  is the fraction of attenuation by extinction that is due to scattering, rather than absorption. Single scattering albedo is the probability that a photon “survives” an interaction with a medium.  $\varpi$  varies between 0 (no scattering) and 1 (no absorption). In reality, neither of these extremes is ever reached, but for water droplets in air, absorption is essentially negligible at the wavelength of visible light. Thus, cloud appearance is entirely attributable to scattering (Bohren, 1987). The dark areas in clouds are caused by scattering of light out of the cloud, rather than by absorption (See “Out-scattering” in Section 2.2.6).

### 2.2.3 Single and Multiple Scattering

The previous section discussed the mean free path between scattering events,  $1/\sigma_s$ . If the physical extents of a medium are smaller than this distance, then on average a photon passing through it is scattered at most once. Scattering of light by a single particle is called *single scattering*. Media that are either physically very thin or very

transparent are *optically thin*. For such media, light scattering can be approximated using single scattering models. Clear air and “steam” (actually droplets of condensed water vapor) from a cup of coffee are examples of this.

*Multiple scattering* is scattering of light from multiple particles in succession. Models that account for only single scattering cannot accurately represent media such as clouds and fallen snow, which are *optically thick* (Bohren, 1987). Because these media have very high single scattering albedo (close to 1), and are often optically thick, nearly all light that enters them exits, but only after many scattering events. Multiple scattering explains the bright white and diffuse appearance of clouds.

### 2.2.4 Optical Depth and Transparency

*Optical Depth* is a dimensionless measure of how opaque a medium is to light passing through it. For a homogeneous medium, or a homogeneous segment of medium, it is the product of the physical material thickness,  $ds$ , and the extinction coefficient  $K$ . For an inhomogeneous medium, the optical depth  $\tau(s, s')$  of an arbitrary segment between the parameters  $s$  and  $s'$  is

$$\tau(s, s') = \int_s^{s'} K(\vec{x} + t\vec{\omega}) dt, \quad (2.19)$$

where  $\vec{\omega}$  is the direction of propagation of light.

A more intuitively grasped concept is that of *transmittance* (also known as transparency). Transmittance  $T(s, s')$  is computed from optical depth as

$$T(s, s') = e^{-\tau(s, s')} \quad (2.20)$$

Transmittance is the percentage of light leaving point  $\vec{x}$  at parameter  $s$  that reaches point  $\vec{x}'$  at parameter  $s'$ . The opacity of the segment is the inverse of the transmittance:  $\alpha(s, s') = 1 - T(s, s')$ . An optical depth of  $\tau(s, s') = 1$  indicates that there is  $e^{-1} \approx 37\%$  chance that the light will travel at least the length of the segment without being scattered or absorbed. An infinite optical depth means that the medium is opaque.

### 2.2.5 Phase Function

The optical properties discussed so far characterize the relative amounts of scattering and absorption, but they do nothing to account for the directionality of scattering. A

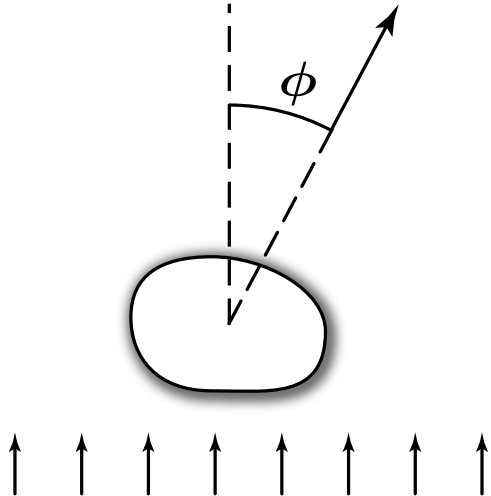


Figure 2.1: The scattering angle,  $\phi$ , is the angle between the incident (denoted by the vertical arrows) and scattered light directions.

*phase function* is a function of direction that determines how much light from incident direction  $\vec{\omega}'$  is scattered into the exitant direction  $\vec{\omega}$ . The use of the term “phase” derives from astronomy (lunar phase), and is unrelated to the phase of a wave (Blinn, 1982b; van de Hulst, 1981). The phase function depends on the *phase angle*  $\phi$  between  $\vec{\omega}'$  and  $\vec{\omega}$  (see Figure 2.1), and on the wavelength of the incident light. The phase function is dimensionless, and is normalized, because it is a probability distribution (Premože et al., 2003):

$$\int_{4\pi} P(\vec{\omega}, \vec{\omega}') d\vec{\omega}' = 1.$$

The phase function also satisfies reciprocity, so  $P(\vec{\omega}, \vec{\omega}') = P(\vec{\omega}', \vec{\omega})$ .

The shape of a phase function is highly dependent on the size, refractive index, and shape of the particle, and therefore differs from particle to particle. Given knowledge of the type and size distribution of particles, it is common to use an average phase function that captures the most important features of scattering in the medium. (Hence I dropped the positional dependence of the phase function in the previous equation.) There are a number of commonly used phase functions that have arisen from the study of different classes of particles that occur in Earth’s atmosphere. Each has advantages for different applications. A useful survey of several phase functions can be found in (Premože et al., 2003).

## Rayleigh Phase Function

Scattering by very small particles such as those found in clear air can be approximated using Rayleigh scattering, developed by Lord Rayleigh (Strutt, 1871). The phase function for Rayleigh scattering is

$$P_{ray}(\phi) = \frac{3}{4} \frac{(1 + \cos^2 \phi)}{\lambda^4}, \quad (2.21)$$

where  $\lambda$  is the wavelength of the incident light. The dependence on wavelength explains many well-known phenomena, including the blueness of the sky—blue light ( $\sim 0.4 \mu\text{m}$ ) is scattered about ten times more than red ( $\sim 0.7 \mu\text{m}$ ).

## Mie Scattering and the Henyey-Greenstein Phase Function

Gustav Mie developed a theory of scattering by larger particles (Mie, 1908). Mie scattering theory is much more complicated and expensive to evaluate than Rayleigh scattering, but some simplifying assumptions can be made. A popular approximation for Mie scattering is the Henyey-Greenstein phase function (Henyey and Greenstein, 1941):

$$P_{HG}(\phi) = \frac{1}{4\pi} \frac{1 - g^2}{(1 - 2g \cos \phi + g^2)^{3/2}}. \quad (2.22)$$

This is the polar form for an ellipse centered at one of its foci. Anisotropy of the scattering is controlled by the symmetry parameter  $g$ , which defines the eccentricity of the ellipse. Positive values of  $g$  indicate that most of the incident light is scattered in the forward direction, negative values indicate backward scattering, and  $g = 0$  indicates isotropic scattering. A useful result of Mie scattering is that particles that are large with respect to the wavelength of light result in highly anisotropic scattering. In particular, large particles scatter much more strongly in the *forward direction* (A phase angle of  $0^\circ$ —the scattering direction is equal to the incident direction.), as shown in Figure 2.2. Cloud droplets vary in size, but a typical cloud has droplets that range from  $1\text{--}50 \mu\text{m}$ . The wavelength of visible light is in the range  $0.4\text{--}0.7 \mu\text{m}$ . Figure 2.3 shows an example distribution of particle sizes in a cumulus cloud.

### 2.2.6 Light Transport

The previous sections discussed the optical properties of light scattering media, and how they affect the way in which materials interact with light. In order to fully describe this

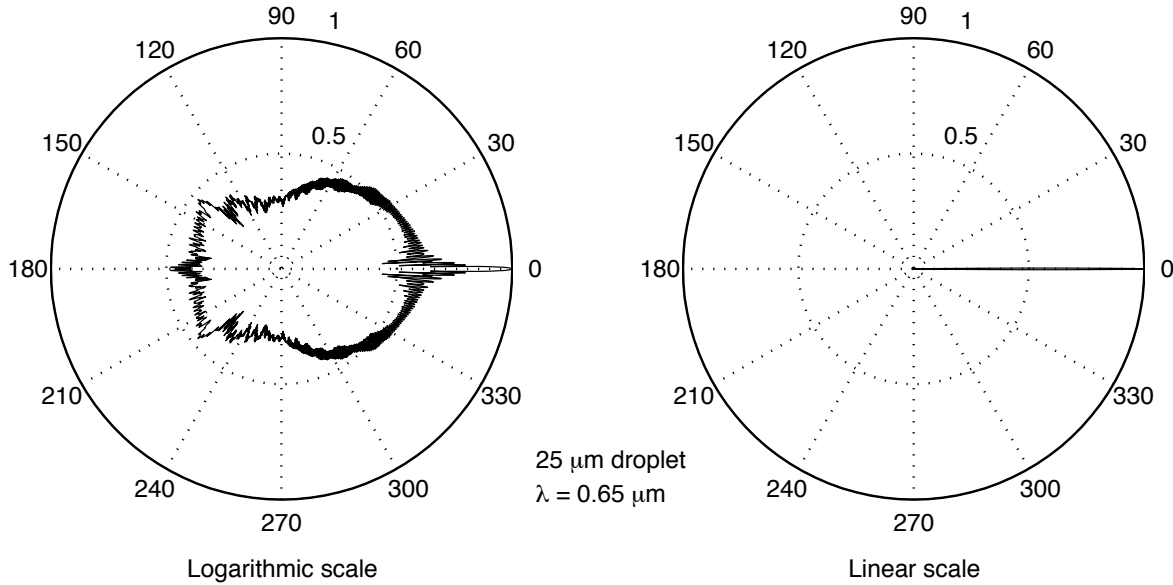


Figure 2.2: An example of strong forward scattering from a water droplet. These polar plots display relative scattering intensity with respect to scattering angle for  $0.65\mu\text{m}$  (red) light incident on a  $25\mu\text{m}$  spherical water droplet. The left plot uses a logarithmic intensity scale to provide a detailed representation of the scattering function. The right plot uses a linear scale to show clearly that scattering from large water droplets is strongly dominated by scattering in the forward direction (notice that it appears as a simple line at zero degrees). The plot data were generated with *MiePlot* software (Laven, 2003).

interaction, I need to present the mathematics of light transport. These mathematics describe the intensity distribution of light exiting a medium, given the incident intensity distribution and the optical properties and geometry of the medium.

When light passes through a highly scattering medium, it undergoes a series of interactions with particles. These scattering and absorption events modify the direction and intensity distribution of the incoming light field. The light in a beam with extant direction  $\vec{\omega}$  can be both attenuated and intensified. Intensity is attenuated due to absorption and out-scattering—scattering of light from direction  $\vec{\omega}$  into other directions. The light can be intensified due to in-scattering—scattering of light from other directions into direction  $\vec{\omega}$ . In this section I discuss each of the factors in attenuation and intensification in order to present a single light transport equation, as in (Premož et al., 2003).

In what follows, I use the term *radiance* to describe the intensity of light. Radiance,  $L$ , is a measure of light intensity. It is defined as radiant power per unit area per

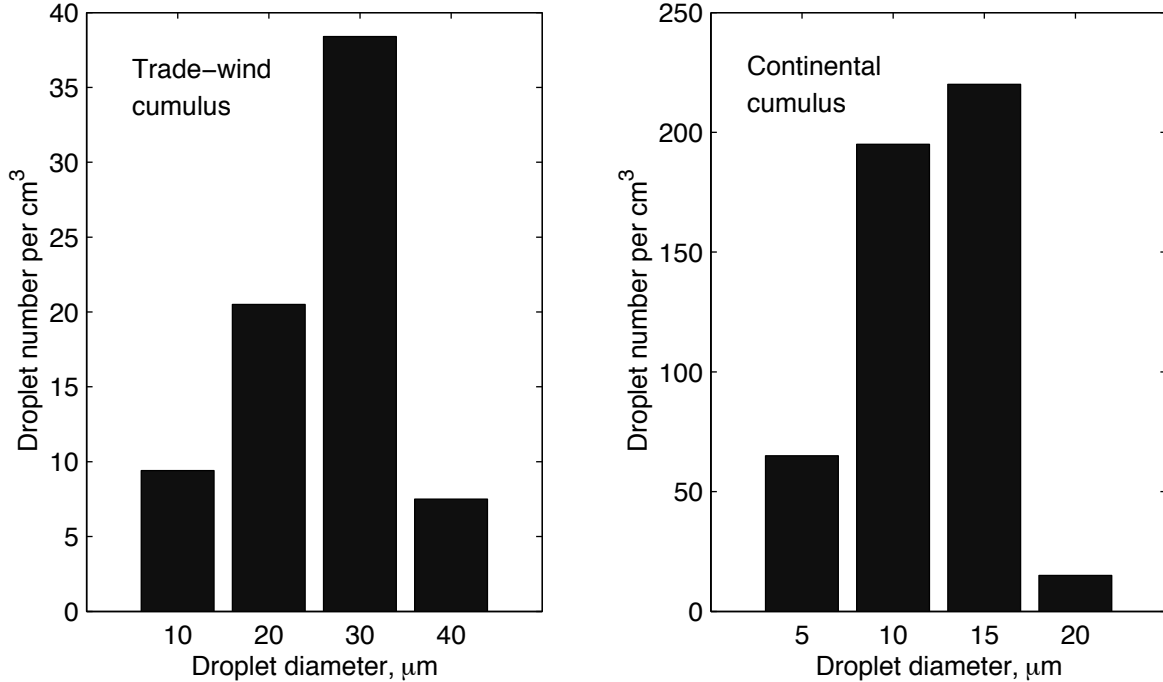


Figure 2.3: Droplet size spectra in trade-wind cumulus off the coast of Hawaii (left) and continental cumulus over the Blue Mountains near Sydney, Australia (right) (Based on (Rogers and Yau, 1989)).

unit solid angle, and is usually measured in watts per square meter per steradian ( $\text{W m}^{-2} \text{ sr}^{-1}$ ).

## Absorption

As I mentioned before, the absorption coefficient  $K_a$  is the probability of absorption per unit length. Thus, the change in radiance  $dL$  due to absorption over distance  $ds$  in direction  $\vec{\omega}$  is

$$\frac{dL(\vec{x}, \vec{\omega})}{ds} = -K_a(\vec{x})L(\vec{x}, \omega). \quad (2.23)$$

## Out-scattering

Out-scattering is computed in the same way as absorption, with the substitution of the coefficient of scattering. The change in radiance  $dL$  due to out-scattering over distance  $ds$  in direction  $\vec{\omega}$  is

$$\frac{dL(\vec{x}, \vec{\omega})}{ds} = -K_s(\vec{x})L(\vec{x}, \omega). \quad (2.24)$$

## Extinction

Because  $K = K_s + K_a$ , Equations (2.23) and (2.24) can be combined into a single equation,

$$\frac{dL(\vec{x}, \vec{\omega})}{ds} = -K(\vec{x})L(\vec{x}, \omega). \quad (2.25)$$

The solution of this equation is the origin of Equation (2.20) for transmittance.

## In-scattering

To compute the effects of in-scattering, we must account not only for the amount of scattering, but also the directionality of the scattering. For this we need to incorporate the phase function. Also, because light from any incident direction may be scattered into direction  $\vec{\omega}$ , we must integrate over the entire sphere of incoming directions. Thus, the change in radiance  $dL$  due to in-scattering over distance  $ds$  in direction  $\vec{\omega}$  is

$$\frac{dL(\vec{x}, \vec{\omega})}{ds} = K_s(\vec{x}) \int_{4\pi} P(\vec{x}, \vec{\omega}, \vec{\omega}') L(\vec{x}, \vec{\omega}') d\vec{\omega}', \quad (2.26)$$

where  $\vec{\omega}'$  is the incoming direction of the in-scattered light. In general, this can be computationally expensive to evaluate due to the spherical integral, so in practice, simplifying assumptions are used to reduce the expense.

## Light Transport

Equations (2.25) and (2.26) combine to form a single differential equation for light transport in a scattering and absorbing medium:

$$\frac{dL(\vec{x}, \vec{\omega})}{ds} = -K(\vec{x})L(\vec{x}, \vec{\omega}) + K_s(\vec{x}) \int_{4\pi} P(\vec{x}, \vec{\omega}, \vec{\omega}') L(\vec{x}, \vec{\omega}') d\vec{\omega}', \quad (2.27)$$

As pointed out in (Max, 1995), this equation can be solved by bringing the extinction term to the left-hand side and multiplying by the integrating factor

$$\exp \left( \int_0^s K(t) dt \right).$$

Integration of the resulting equation along the ray parameterized by  $t$  between  $t = 0$  (the edge of the medium where the light is incident) and  $t = D$  (the edge of the medium where the light exits) produces the following expression for the exitant radiance at  $t = D$

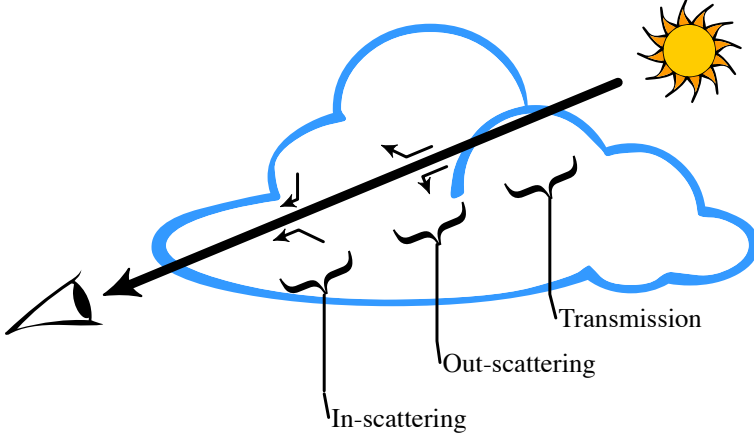


Figure 2.4: An overview of light transport in clouds. As labeled, the arrows demonstrate light paths for in-scattering, out-scattering, and transmission. To accurately render images of clouds, the effects of all three of these must be integrated along light paths through the cloud. Due to the expense of integrating in-scattering for all incident directions, computational simplifications are used in practice.

(Max, 1995):

$$L(D, \vec{\omega}) = L(0, \vec{\omega})T(0, D) + \int_0^D g(s)T(s, D)ds. \quad (2.28)$$

Here  $L(0, \vec{\omega})$  is the incident radiance,

$$g(s) = K_s(\vec{x}(s)) \int_{4\pi} P(\vec{x}, \vec{\omega}, \vec{\omega}') L(\vec{x}(s), \vec{\omega}') d\vec{\omega}' \quad (2.29)$$

and  $T(s, s')$  is the transmittance as defined in Equation (2.20). For consistency, I have parameterized the position  $\vec{x}$  along the ray by  $s$ .

To understand Equation (2.28), it makes sense for our purposes to examine it in terms of cloud illumination. Imagine a person observing a cloud along the viewing direction  $-\vec{\omega}$  as in Figure 2.4. Then the first term represents the intensity of light from behind the cloud traveling in direction  $\vec{\omega}$  that reaches the observer. This is the *extinction term*. The second term is the *in-scattering term*, which represents light scattered into the view direction over the entire traversal of the cloud from all other directions  $\vec{\omega}$ . Notice that the in-scattering term incorporates the transmittance  $T(s, D)$ . This is because light may be attenuated after it is scattered into the view direction.

In order to determine the intensity of light scattered to any point  $\vec{p}$  in the cloud from another point  $\vec{p}'$ , we must first determine the intensity of light at point  $\vec{p}$ . Because this intensity also depends on absorption and scattering, the problem is recursive. This

is the multiple scattering problem, and it is clear why accurate solutions are very expensive. Fortunately, as mentioned in Section 2.2.5, scattering in clouds is strongly peaked in the forward direction. I save computation by approximating the spherical integral in (2.29) with an integral over a small solid angle around the forward direction. This simplification focuses computation in the directions of greatest importance. In Chapter 6 I present details of this simplification and use it to derive algorithms for efficiently computing cloud illumination.

## 2.3 Summary

In this chapter, I have described the mathematics necessary for simulation of cloud dynamics and radiometry. The equations of my cloud dynamics model are summarized in Section 2.1.10. The equations needed for radiometry simulation are more concise. They are the light transport equation, (2.28), along with the phase function (Section 2.2.5), transmittance (Equation (2.20)), and the in-scattering term (Equation (2.29)). In Chapter 4, I introduce the concepts necessary to perform dynamics simulation on the GPU, and complete the discussion of cloud dynamics simulation in Chapter 5. I give details of cloud radiometry simulation in Chapter 6. The following chapter covers related work in both areas.

# Chapter 3

## Related Work

Much effort has been made in computer graphics on the synthesis of real-world imagery. The sky is an essential part of realistic outdoor scenery. Because of this, cloud rendering has been an active area of research in computer graphics for the past twenty years. In Chapter 2, I described two important aspects of visual simulation of clouds—radiometry and dynamics. In this chapter I cover related work in those areas. To demonstrate where my work fits in among the related works, Table 3.1 provides a representative list of previous work categorized by contributions in cloud dynamics, cloud radiometry, and interactivity.

While simulation and illumination of clouds are essential to this dissertation, a survey of previous work on clouds would be incomplete without a description of the variety of methods that have been used to model clouds, so this is where I begin.

### 3.1 Cloud Modeling

As is true for any object or phenomenon, there are multiple ways to model clouds. An explicit representation of every water droplet in a cloud would require far too much computation and storage, so most researchers have used much coarser models. In this section I describe five general methods that have been used to model and render clouds: particle systems, metaballs, voxel volumes, procedural noise, and textured solids. Note that these techniques are not mutually exclusive; multiple techniques have been combined with good results.

	Citation	Dynamics	Radiometry	Interactive
Kajiya and Von Herzen, 1984			★	
Gardner, 1985				
Lewis, 1989				
Nishita et al., 1996			★	
Ebert, 1997	Procedural			
Dobashi et al., 2000	★	★		
Elinas and Stürzlinger 2001			★	
Harris and Lastra 2001		★	★	
Miyazaki et al., 2001	★	★		
Overby et al., 2002	★			Near
Schpok et al., 2003	Procedural			★
Harris et al., 2003	★	★	★	

Table 3.1: A representative selection of previous work on clouds in the field of computer graphics. The works are categorized with respect to contributions on cloud dynamics simulation, cloud radiometry simulation, and interactivity. The works without any stars presented static cloud modeling or rendering methods.

### 3.1.1 Particle Systems

Particle systems model objects as a collection of *particles*—simple primitives that can be represented by a single 3D position and a small number of attributes such as radius, color, and texture. Reeves introduced particle systems in (Reeves, 1983) as an approach to modeling clouds and other “fuzzy” phenomena, and described approximate methods of shading particle models in (Reeves and Blau, 1985). Particles can be created by hand using a modeling tool, procedurally generated, or created with some combination of the two. Particles can be rendered in a variety of ways. In the cloud rendering technique that I describe in detail in Chapter 6, I model static clouds with particles, and render each particle as a small, textured sprite (or “splat” (Westover, 1990)). I originally described this technique in (Harris and Lastra, 2001).

Particles have the advantage that they usually require only very simple and inexpensive code to maintain and render. Because a particle implicitly represents a spherical volume, a cloud built with particles usually requires much less storage than a similarly

detailed cloud represented with other methods. This advantage may diminish as detail increases, because many tiny particles are needed to achieve high detail. In this situation other techniques, such as those described in the following sections, may be more desirable.

### 3.1.2 Metaballs

Metaballs (or “blobs”) represent volumes as the superposition of potential fields of a set of sources, each of which is defined by a center, radius, and strength (Blinn, 1982a). These volumes can be rendered in a number of ways, including ray tracing and splatting. Alternatively, isosurfaces can be extracted and rendered, but this might not be appropriate for clouds. Nishita et al. used metaballs to model clouds by first creating a basic cloud shape by hand-placing a few metaballs, and then adding detail via a fractal method of generating new metaballs on the surfaces of existing ones (Nishita et al., 1996). Dobashi et al. used metaballs to model clouds extracted from satellite images (Dobashi et al., 1999). In (Dobashi et al., 2000), clouds simulated on a voxel grid were converted into metaballs for rendering with splatting.

### 3.1.3 Voxel Volumes

Voxels are another common representation for clouds. A *voxel* is the three-dimensional analog of a pixel. It is a single cell of a regular grid subdivision of a rectangular prism. Voxel models provide a uniform sampling of the volume, and can be rendered with both forward and backward methods. There is a large body of existing work on volume rendering that can be drawn upon when rendering clouds represented as voxel volumes (Levoy, 1988; Westover, 1990; Wilson et al., 1994; Cabral et al., 1994; Kniss et al., 2002). Voxel grids are typically used when physically-based simulation is involved. Kajiya and Von Herzen performed a simple physical cloud simulation and stored the results in a voxel volume which they rendered using ray tracing (Kajiya and Von Herzen, 1984). Dobashi, et al. simulated clouds on a voxel grid using a cellular automata model similar to (Nagel and Raschke, 1992), converted the grid to metaballs, and rendered them using splatting (Dobashi et al., 2000). Miyazaki, et al. 2001 also performed cloud simulation on a grid using a method known as a Coupled Map Lattice (CML), and then rendered the resulting clouds in the same way as Dobashi et al. (Miyazaki et al., 2001). (Overby et al., 2002) solved a set of partial differential equations to generate clouds on a voxel grid and rendered them using my *SkyWorks* (Harris and Lastra, 2001)

rendering engine. I have solved a similar set of PDEs on a voxel grid using graphics hardware (Harris et al., 2003). I describe my simulation technique in detail in Chapter 5 and the rendering in Chapter 6.

### 3.1.4 Procedural Noise

Procedural solid noise techniques are another important technique for generating models of clouds. These methods use noise as a basis, and perform various operations on the noise to generate random but continuous density data to fill cloud volumes (Lewis, 1989; Perlin, 1985). Ebert has done much work in modeling “solid spaces” using procedural solid noise, including offline computation of realistic images of smoke, steam, and clouds (Ebert and Parent, 1990; Ebert, 1997; Ebert et al., 2002). Ebert modeled clouds using a union of implicit functions. He then perturbed the solid space defined by the implicit functions using procedural solid noise, and rendered it using a scan line renderer. Schpok et al. recently extended Ebert’s techniques to take advantage of programmable graphics hardware for fast animation and rendering (Schpok et al., 2003).

### 3.1.5 Textured Solids

Others have chosen surface representations of clouds rather than volume representations. Gardner used fractal texturing on the surface of ellipsoids to simulate the appearance of clouds (Gardner, 1985). By combining multiple textured and shaded ellipsoids, he was able to create convincing cloudy scenes reminiscent of the landscape paintings of John Constable. Lewis also used ellipsoids for clouds, but with procedural solid noise (Lewis, 1989). More recently, Elinas and Stürzlinger used a variation of Gardner’s method to interactively render clouds composed of multiple ellipsoids (Elinas and Stürzlinger, 2001).

## 3.2 Cloud Dynamics Simulation

Cloud simulation has been of interest to meteorologists and atmospheric scientists since the advent of high performance computing, but it has only recently drawn much interest from the computer graphics community. Scientific simulations of clouds and weather are typically very complex, requiring many hours of computation to simulate a relatively short time of cloud development.

The earliest simulations in atmospheric science were simple one-dimensional models such as the one presented by (Srivastava, 1967). His model represented only vertical motion and computed changes under the influences of condensation and precipitation. Later models extended the simulation to two dimensions, but the extreme computational expense of three dimensions was prohibitive, so researchers tended to resort to slab symmetry or axial symmetry (Rogers and Yau, 1989). These symmetries limit simulation to two dimensions, but they at least provide the ability to simulate horizontal wind shear, which is important to cloud dynamics. One of the earliest such simulations was presented in (Takeda, 1971). Because rotational flow—including vortices with both horizontal and vertical axes of rotation—is common in real clouds, three dimensional simulation is essential for high accuracy. Steiner presented the first fully three-dimensional model, and in a comparison with a similar two-dimensional model, he showed important differences in the rotational motion of the clouds (Steiner, 1973). Three-dimensional cloud simulation has progressed since then. For a more detailed survey of cloud simulation in atmospheric physics, see (Rogers and Yau, 1989).

Simulations from atmospheric physics are too expensive for computer graphics applications other than scientific visualization. Because they are used to understand our atmosphere and weather, many of them include a high level of detail that is not visible in nature, including very specific tracking of water state and droplet size distributions, complex microphysics, and detailed fluid dynamics at a variety of scales. If the goal is simply to create realistic images and animations of clouds, much less detailed *visual simulations* can be used.

Kajiya and Von Herzen were the first in computer graphics to demonstrate a visual cloud simulation (Kajiya and Von Herzen, 1984). They solved a very simple set of partial differential equations to generate cloud data sets for their ray tracing algorithm. The PDEs they solved were the Navier-Stokes equations of incompressible fluid flow; a simple thermodynamic equation to account for advection of temperature and latent heat effects; and a simple water continuity equation. The simulation required about 10 seconds per time step (one second of cloud evolution) to update a  $10 \times 10 \times 20$  grid on a VAX 11/780. Overby et al. described a similar but slightly more detailed physical model based on PDEs (Overby et al., 2002). They used the stable fluid simulation algorithm of (Stam, 1999) to solve the Navier-Stokes equations. The stability of this method allows much larger time steps, so Overby et al. were able to achieve simulation rates of one iteration per second on a  $15 \times 50 \times 15$  grid using an 800MHz Pentium III. I have implemented a faster and slightly more realistic cloud simulation using pro-

grammable floating point graphics hardware. This work is described briefly in (Harris et al., 2003), and in more detail in Chapter 5.

Other researchers have tried simpler, but less realistic rule-based simulation techniques. Neyret used an animated particle system to model cloud behavior, using a set of heuristics to approximate the rolling behavior of convective clouds (Neyret, 1997). (Dobashi et al., 2000) used a simple cellular automata (CA) model of cloud formation to animate clouds offline. The model was based on the simple CA introduced by (Nagel and Raschke, 1992). Nagel and Raschke's original CA had rules for the spread of humidity between neighboring cells and for the formation of clouds in humid cells, but included no mechanism for evaporation. Dobashi et al. added a stochastic rule for evaporation so that the clouds would appear to grow and dissipate. Their model achieved a simulation time of about 0.5 seconds on a  $256 \times 256 \times 20$  volume using a dual 500 MHz Pentium III.

In similar work, Miyazaki et al. used a coupled map lattice (Kaneko, 1993) rather than a cellular automaton (Miyazaki et al., 2001). This model was an extension of an earlier coupled map lattice model from the physics literature (Yanagita and Kaneko, 1997). Coupled map lattices (CML) are an extension of CA with continuous state values at the cells, rather than discrete values. In Chapter 4, I describe work I have done on performing CML simulations on programmable graphics hardware (Harris et al., 2002). The CML of Miyazaki et al. used rules based on atmospheric fluid dynamics, including a rule used to approximate incompressibility and rules for advection, vapor and temperature diffusion, buoyancy, and phase changes. They were able to simulate a 3–5 s time step on a  $256 \times 256 \times 40$  lattice in about 10 s on a 1 GHz Pentium III.

Of the previous work in cloud simulation for computer graphics, my work is most similar to the work by Kajiya and Von Herzen and Overby et al. However, there are several differences. Both Overby et al. and Kajiya and Von Herzen use a buoyancy force that is proportional to potential temperature. My model also accounts for the negative buoyancy effects of condensed water mass and the positive buoyancy effects of water vapor (see Section 2.1.5). This increases the realism of air currents. Overby et al. also assume that saturation is directly proportional to pressure, but they provide no information about how they model pressure in their system. My system uses a well-known exponential relationship between saturation and temperature (described in Section 2.1.7), and does not explicitly model pressure. In addition, Overby et al. introduce two effects that are physically unrealistic. One is a computation meant to account for the expansion of rising air. The other is an artificial momentum-conservation

computation. These computations are superfluous because the Navier-Stokes equations already account for these phenomena. Overby et al. were able to achieve rates of one simulation iteration per second. Extrapolating to the fastest current CPU speeds, their system would likely improve to a few iterations per second. I achieve similar rates on volumes that are larger by a factor of about 20 ( $64 \times 64 \times 64$  vs.  $15 \times 50 \times 15$ ) due to the speed of the graphics hardware. Finally, none of the previous simulations have been integrated into truly interactive, high frame rate applications. I describe the integration of cloud simulation with an interactive flight application in Section 5.5.

### 3.3 Light Scattering and Cloud Radiometry

Some of the earliest work on simulating light scattering for computer graphics was presented in (Blinn, 1982b). Motivated by the need to render the rings of Saturn, Blinn described an approximate method for computing the appearance of cloudy or dusty surfaces via statistical simulation of the light-matter interaction. Blinn made a simplifying assumption in his model—that the primary effect of light scattering is due to reflection from a single particle in the medium, and multiple reflections can be considered negligible. This *single scattering assumption* has become common in computer graphics, but as Blinn and others have noted (Bohren, 1987), it is only valid for media with particles of low single scattering albedo. Blinn also simplified the problem by limiting application of his model to plane parallel atmospheres, rather than handling scattering in arbitrary domains.

As I discussed in Chapter 2, accurate computation of light scattering in media with high single scattering albedo is expensive, because it requires evaluation of a double integral equation. In practice, researchers either use simplifying assumptions to reduce the complexity of the problem, or perform long offline computations. There are multiple ways to compute light scattering, and many simplifications that can be applied. I will group previous work in this area into five categories: Spherical Harmonics Methods, Finite Element Methods, Discrete Ordinates, Monte Carlo Integration, and Line Integral Methods.

#### 3.3.1 Spherical Harmonics Methods

The spherical harmonics  $Y_l^m(\theta, \phi)$  are the angular portion of the solution of Laplace's equation in spherical coordinates (Weisstein, 1999). The spherical harmonics form a

complete orthonormal basis. This means that an arbitrary function  $f(\theta, \phi)$  can be represented by an infinite series expansion in terms of spherical harmonics:

$$f(\theta, \phi) = \sum_{l=0}^{\infty} \sum_{m=0}^l A_l^m Y_l^m(\theta, \phi).$$

The method of determining the coefficients,  $A_l^m$ , of the series is analogous to determining the coefficients of a Fourier series expansion of a function. If the value of  $f$  is known at a number of samples, then a series of linear equations can be formulated and solved for the coefficients. Spherical harmonics methods have been used by (Bhate and Tokuta, 1992; Kajiya and Von Herzen, 1984; Stam, 1995) to compute multiple scattering.

Kajiya and Von Herzen presented a ray tracing technique for rendering arbitrary volumes of scattering media. In addition to a simple single scattering model, they also described a solution method for multiple scattering that uses spherical harmonics (Kajiya and Von Herzen, 1984). Their single scattering simulation method stored the cloud density and illumination data on voxel grids, and their algorithm required two passes. In the first pass, scattering and absorption were integrated along paths from the light source through the cloud to each voxel where the resulting intensities were stored. In the second pass, eye rays were traced through the volume of intensities and scattering of light to the eye was computed, resulting in a cloud image. For multiple scattering, the authors derived a discrete spherical harmonics approximation to the multiple scattering equation, and solved the resulting matrix of partial differential equations using relaxation. This matrix solution replaces the first integration pass of the single scattering algorithm. As mentioned in (Stam, 1995), this method is known as the  $P_N$ -method in the transport theory literature, where  $N$  is the degree of the highest harmonic in the spherical harmonic expansion.

Following Kajiya and Von Herzen's lead, two pass algorithms for computing light scattering in volumetric media—including the algorithms I will present later in this dissertation—are now common. Interestingly, (Max, 1994) points out that while Kajiya and Von Herzen attempted to compute multiple scattering for the case of an isotropic phase function, it is not clear if they succeeded; all of the images in the paper seem to have been computed with the simpler single scattering model.

Stam explained in (Stam, 1995) that while (Kajiya and Von Herzen, 1984) derived a very general  $N$ -term expression for multiple scattering using a spherical harmonics

expansion, they truncated the expansion after the first term to produce their results. He showed that this truncation results in a diffusion type equation for the scattered portion of the illumination field. In media where scattering events are very frequent—“optically thick” media—multiple scattering can be approximated as diffusion of the light energy. In other words, at any location in the medium, photons can be found traveling in arbitrary directions. The light is said to be *diffuse*. Stam presented this diffusion approximation in more detail. Like Kajiya and Von Herzen, Stam represented the scattering medium on a voxel grid. He described two ways to solve for the intensity. In the first method, he discretized the diffusion approximation on the grid to formulate a system of linear equations that he then solved using the *multigrid* method. (See (Briggs et al., 2000) for more information on multigrid methods.) The second method is a finite element method (see Section 3.3.2) in which he used a series expansion of basis functions, specifically Gaussian kernel functions of distance. This expansion led to a matrix system that he solved using *LU* decomposition.

### 3.3.2 Finite Element Methods

The *finite element method* is another technique for solving integral equations that has been applied to light transport. In the finite element method, an unknown function is approximated by dividing the domain of the function into a number of small pieces, or *elements*, over which the function can be approximated using simple *basis functions* (often polynomials). As a result, the unknown function can be represented with a finite number of unknowns and solved numerically (Cohen and Wallace, 1993).

A common application of finite elements in computer graphics is the *radiosity method* for computing diffuse reflection among surfaces. In the radiosity method, the surfaces of a scene represent the domain of the radiosity function. An integral equation characterizes the intensity, or *radiosity*, of light reflected from the surfaces. To solve the radiosity equation, the surfaces are first subdivided into a number of small elements on which the radiosity will be represented by a sum of weighted basis functions. This formulation results in a system of linear equations that can be solved for the weights. The coefficients of this system are integrals over parts of the surfaces. Intuitively, light incident on an arbitrary point in the scene can be reflected to any other point; hence the coefficients are integrals over the scene. In the finite element case, these integrals are evaluated for every pair of elements in the scene, and are called *form factors* (Cohen and Wallace, 1993).

Rushmeier and Torrance extended the radiosity method to include radiative transfer in volumes of participating media (Rushmeier and Torrance, 1987). This *zonal method*, like the radiosity method, was originally developed for radiant heat transfer analysis. The zonal method divides the volume of a participating medium into finite elements which are assumed to have constant radiosity. As with the radiosity method, form factors are computed for every pair combination of surface elements in the scene, as well as every pair of volume elements and all surface-volume pairs. This is complicated by the fact that the form factors involve a double integral over points in both elements, as well as along the path between the elements. As in the radiosity method, a system of simultaneous linear radiosity equations is formulated based on these form factors. The solution of this system is the steady-state diffuse radiosity at each element of the environment, including the effects of scattering and absorption by the participating medium. Rushmeier and Torrance's presentation of the zonal method was limited to isotropic scattering media, with no mention of phase functions.

Nishita et al. introduced approximations and a rendering technique for global illumination of clouds, accounting for multiple anisotropic scattering and skylight (Nishita et al., 1996). This method can also be considered a finite element method, because the volume is divided into voxels and radiative transfer between voxels is computed. Nishita et al. made two simplifying observations that reduced the cost of the computation. The first observation was that the phase function of cloud water droplets is highly anisotropic, favoring forward scattering (see Section 2.2.5). The result of this is that not all directions contribute strongly to the illumination of a given volume element. Therefore, Nishita et al. computed a “reference pattern” of voxels that contributed significantly to a given point. This pattern is constant at every position in the volume, because the sun can be considered to be infinitely distant. Thus, the same sampling pattern can be used to update the illumination of each voxel. The second observation they made was that only the first few orders of scattering contribute strongly to the illumination of a given voxel. Therefore, Nishita et al. only computed up to the third order of scattering. In my cloud illumination algorithms, I also take advantage of the anisotropy of scattering by cloud droplets (see Chapter 6).

### 3.3.3 Discrete Ordinates

The method of *discrete ordinates* allocates the radiosity exiting each volume element into a collection of  $M$  discrete directions. The intensity is assumed to be constant over

each direction “bin”. This method can be used to account for anisotropic scattering. If an interaction between a pair of elements can be represented by only one direction bin (this is unreasonable for elements that are close), then the number of non-zero elements in the matrix of linear coefficients is  $MN^2$ , where  $N = n^3$  is the number of elements in the volume (Max, 1994). Chandrasekhar used the discrete ordinates method in early radiative transfer work (Chandrasekhar, 1960). However, Max points out that this method introduces sampling artifacts because it effectively shoots energy from elements in infinitesimal beams along the discrete directions, missing the regions between them. In work inspired by (Patmore, 1993), Max improved on the basic method of discrete ordinates by efficiently spreading the shot radiosity over an entire direction bin, rather than along discrete directions. The method achieves a large speedup by handling a whole plane of source elements simultaneously, which reduces the computation time to  $O(MN \log N + M^2N)$ .

### 3.3.4 Monte Carlo Integration

*Monte Carlo Integration* is a statistical method that uses sequences of random numbers to solve integral equations. In complex problems like light transport, where computing all possible light-matter interactions would be impossible, Monte Carlo methods reduce the complexity by randomly sampling the integration domain. With enough samples, chosen intelligently based on importance, an accurate solution can be found with much less computation than a complete model would require. The technique of intelligently choosing samples is called *importance sampling*, and the specific method depends on the problem being solved. A common application of Monte Carlo methods in computer graphics is *Monte Carlo ray tracing*. In this technique, whenever a light ray traversing a scene interacts with matter (either a solid surface or a participating medium), statistical methods are used to determine whether the light is absorbed or scattered (for solids, this scattering may be thought of as reflection or refraction). If the light is scattered, the scattered ray direction is also chosen using stochastic methods. Importance sampling is typically used to determine the direction via the evaluation of a probability function. A useful introduction to Monte Carlo ray tracing can be found in (Veach, 1997).

Blasi, et al. presented a technique for rendering arbitrary volumes of participating media using Monte Carlo ray tracing (Blasi et al., 1993). They placed no restrictions on the medium, allowing arbitrary distributions of density and phase function, and accounting for multiple scattering. They demonstrated an importance sampling tech-

nique that uses the phase function as a probability function to determine the outgoing direction of scattered rays. This way, the in-scattering integral of Equation (2.27) does not have to be evaluated over the entire sphere of incoming directions, and a large amount of computation is saved. Using the phase function for importance sampling ensures that the most significant contributions of scattering are used to determine the intensity. In this way, the technique is similar to the “reference pattern” technique used by (Nishita et al., 1996).

Photon mapping is a variation of pure Monte Carlo ray tracing in which photons (particles of radiant energy) are traced through a scene (Jensen, 1996). Many photons are traced through the scene, starting at the light sources. Whenever a photon lands on a nonspecular surface it is stored in a *photon map*—a data structure that stores the position, incoming direction, and radiance of each photon hit. The radiance on a surface can be estimated at any point from the photons closest to that point. Photon mapping requires two passes; the first pass builds the photon map, and the second generates an image from the photon map. Image generation is typically performed using ray tracing from the eye. The photon map exhibits the flexibility of Monte Carlo ray tracing methods, but avoids the grainy noise that often plagues them. Jensen and Christensen extended the basic photon map to incorporate the effects of participating media (Jensen and Christensen, 1998). To do so, they introduced a *volume photon map* to store photons within participating media, and derived a formula for estimating the radiance in the media using this map. Their techniques enable simulation of multiple scattering, volume caustics (focusing of light onto participating media caused by specular reflection or refraction), and color transfer between surfaces and volumes of participating media.

### 3.3.5 Line Integral Methods

Recently, interest in simulating light scattering has grown among developers of interactive applications. For view-dependent effects and dynamic phenomena, the techniques described in the previous sections are not practical. While those techniques accurately portray the effects of multiple scattering, they require a large amount of computation. For interactive applications, simplifications must be made.

A first step in simplifying the computation is to ignore volumetric scattering altogether. With or without scattering, visualization of the shadowing effects of absorption by the medium is desirable. This requires at least one pass through the volume (along the direction of light propagation) to integrate the intensity of transmitted light. Be-

cause methods that make this simplification perform the intensity integration along lines from the light source through the volume, I call them *line integral methods*. Kajiya and Von Herzen’s original single scattering algorithm, described in Section 3.3.1, is a line integral method. Intuitively, line integral methods are limited to single scattering because they cannot propagate light back to points already traversed. In Chapter 6, I demonstrate that line integral methods can be used to compute multiple scattering in the forward direction, and that they are therefore useful for interactive cloud rendering.

(Dobashi et al., 2000) described a simple line integral technique for computing the illumination of clouds using the standard blending operations provided by computer graphics APIs such as OpenGL (Segal and Akeley, 2001). Dobashi et al. represented clouds as collections of large “particles” represented by textured billboards. To compute illumination, they rendered the particles in order of increasing distance from the sun into an initially white frame buffer. They configured OpenGL blending operations so that each pixel covered by a particle was darkened by an amount proportional to attenuation by the particle. After rendering a particle, they read the color of the pixel at the center of projection of the particle from the frame buffer. They stored this value as the intensity of incident light that reached the particle through the cloud. Traversal of the particles in order of increasing distance from the light source evaluates the line integral of extinction through each pixel (see Chapter 6). Because pixels are darkened by every particle that overlaps them, this method computes accurate self-shadowing of the cloud. After this first pass, they rendered particles from back to front with respect to the view point, using the intensities computed in the first pass. They configured blending to integrate absorption and single scattering along lines through each pixel of the image, resulting in a realistic image of the clouds. Dobashi et al. further enhanced this realism by computing the shadowing of the terrain by the clouds and shafts of light between the clouds.

As I mentioned previously, the volume must be traversed at least once to integrate attenuation due to absorption. During this traversal, it makes sense to also integrate scattering along the direction of traversal. In Chapter 6, I show how the method of (Dobashi et al., 2000) can be extended to compute this *multiple forward scattering*. I originally presented this technique in (Harris and Lastra, 2001), and extended it to voxel clouds in (Harris et al., 2003).

Kniss, et al. presented a similar line integral approach for absorption and multiple forward scattering in the context of direct volume rendering (Kniss et al., 2002). They rendered volumes of translucent media from 3D textures by rendering slices of the

volume oriented to face along the halfway vector between the light and view directions. This “half angle slice” technique allowed them to interleave light transport integration with the display of the volume. The method traverses the volume slices in order of increasing distance from the light source, performing alternate display and illumination passes. Three buffers are maintained: two for the computation of the illumination of the volume (*current* and *next*), and one (typically the frame buffer) for display of the volume. During the display pass, the current slice is rendered from the observer’s point of view. The slice is textured with the 3D volume texture blended with the *current* illumination buffer. This results in self-shadowing of the volume as in (Dobashi et al., 2000), as well as incorporating the scattering computed during the illumination pass as in (Harris and Lastra, 2001). During the illumination pass, the slice is rendered into the *next* illumination buffer from the light’s point of view, and blended with the *current* illumination buffer to compute the next step in the line integral of extinction and forward in-scattering. During this blending, the *current* buffer is sampled multiple times at jittered locations, and the samples are averaged. This accomplishes a blurring of the forward-scattered light—an ad hoc approximation of multiple scattering over a small solid angle around the forward direction. Even though this method is ad hoc, it is physically-based because multiple scattering in media with a high single scattering albedo results in “blurring” of the light intensity (the light is diffuse).

# Chapter 4

## Physically-Based Simulation on Graphics Hardware

Interactive 3D graphics environments, such as games, virtual environments, and flight simulators are becoming increasingly visually realistic, in part due to the power of graphics hardware. However, these applications often lack rich dynamic phenomena, such as fluids, clouds, and smoke, which are common in the real world. A large body of work in computer graphics has been dedicated to simulating and modeling natural dynamics. One of my goals has been to accelerate such physically-based simulations by performing the computation on graphics hardware.

Graphics hardware is an efficient processor of images—it can use texture images as input, and it outputs images via rendering. Techniques for physically-based simulation of volumetric dynamic phenomena often represent the state of simulations as grids or lattices of values. Images—arrays of values—map well to state values on a grid. Two-dimensional lattices can be represented by 2D textures, and 3D lattices can be represented by 3D textures or collections of 2D textures. This natural correspondence, as well as the programmability and performance of graphics hardware, motivated my research.

In this chapter I discuss techniques for simulation of dynamic phenomena on graphics hardware. Section 4.1 motivates the use of graphics hardware for general purpose computation, and Section 4.1.2 describes previous work in this area. Air is a fluid, so cloud dynamics are first and foremost fluid dynamics. In Section 4.2 I discuss the solution of the Navier-Stokes equations for incompressible fluid flow. I then describe in detail some techniques for performing fluid simulation on a Graphics Processing Unit (GPU). In the next chapter, I discuss the application of these techniques to cloud sim-

ulation. In Section 4.3 I discuss methods for performing physically-based simulation on the previous, less-capable generation of GPUs.

## 4.1 Why Use Graphics Hardware?

GPUs are designed to be efficient coprocessors for rendering and shading. The programmability now available in GPUs such as the NVIDIA GeForce FX (NVIDIA Corporation, 2003) and the ATI Radeon 9800 (ATI Technologies, Inc., 2003) makes them useful coprocessors for more diverse applications. Because the time between new generations of GPUs is currently much less than for CPUs, faster coprocessors are available more often than faster central processors (see Figure 4.1). GPU performance tracks rapid improvements in semiconductor technology more closely than CPU performance. This is because CPUs are designed for low latency computations, while GPUs are optimized for high throughput of vertices and fragments (Lindholm et al., 2001). Low latency on memory-intensive applications typically requires large caches, which use a lot of silicon area. Additional transistors are used to greater effect in GPU architectures because they are applied to additional processors and functional units that increase throughput. In addition, programmable GPUs are inexpensive, readily available, easily upgradeable, and compatible with multiple operating systems and hardware architectures.

More importantly, interactive computer graphics applications have many components vying for processing time. Often it is difficult to efficiently perform simulation, rendering, and other computational tasks simultaneously without a drop in performance. Because my intent is visual simulation, rendering is an essential part of any solution. Moving simulation onto the GPU that renders the results of a simulation not only reduces computational load on the main CPU, but also avoids the substantial bus traffic required to transmit the results of a CPU simulation to the GPU for rendering. In this way, methods of dynamic simulation on the GPU provide an additional tool for load balancing in complex interactive applications.

Graphics hardware also has disadvantages. My first work on GPU simulation was done in collaboration with Greg Coombe, Thorsten Scheuermann, and Anselmo Lastra (Harris et al., 2002). In this work, we used NVIDIA GeForce 3 (NVIDIA Corporation, 2001) and GeForce 4 (NVIDIA Corporation, 2002a) GPUs. The main problems we encountered with these GPUs were the difficulty of programming them and the lack of high precision fragment operations and storage. These problems were related—

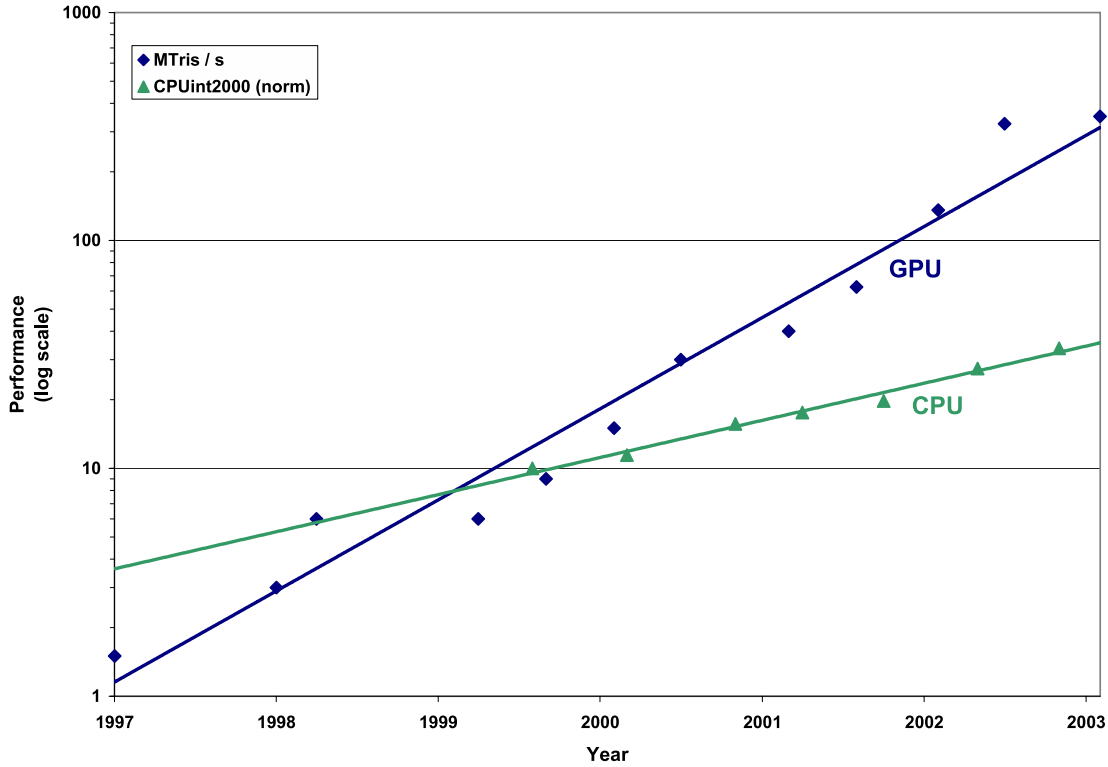


Figure 4.1: A graph of performance increase over time for CPUs and GPUs. GPU performance has increased at a faster rate than CPUs. (Graph and data courtesy of Anselmo Lastra.)

programming difficulty increased with the effort required to ensure that we conserved precision wherever possible.

Within a year of our first experiments, these issues were mostly resolved by the latest GPUs and software. Following a recent research trend in the use of high-level shading languages to program graphics hardware (Peercy et al., 2000; Proudfoot et al., 2001), NVIDIA released its *Cg* shading language (Mark et al., ). *Cg* has greatly increased the ease with which GPUs can be used for general-purpose computation. Also, the new generation of GPUs, the NVIDIA GeForce FX series (NVIDIA Corporation, 2003) and the ATI Radeon 9700/9800 (ATI Technologies, Inc., 2003), provide floating point precision throughout the graphics pipeline. This has enabled the application of GPUs to high-fidelity visual simulations of natural phenomena and other systems of partial differential equations that require storage and computation of high dynamic range numbers. Previously, the lack of floating point capability limited the application of GPUs to either low dynamic range simulations or more ad hoc techniques such as cellular automata (Harris et al., 2002). Future generations of GPUs will likely continue

to improve in flexibility and performance.

### 4.1.1 Classes of GPUs

Graphics processors are evolving rapidly. Manufacturers such as NVIDIA and ATI typically launch a new architecture once a year, with an update about six months later. As a result I have used processors of varying speed and capability in my research. In this chapter, I discuss techniques for performing physically-based simulation on two generations of GPUs. To improve clarity, I will rely on a common classification used in the graphics industry.

There are two standard graphics programming interfaces that are used for most commercial applications: OpenGL (Segal and Akeley, 2001) and DirectX (DX) (Microsoft, 2003). While the core of OpenGL does not change very often,<sup>1</sup> Microsoft has released new versions of DirectX on a schedule very similar to GPU release schedules. As a result, it has become convenient to classify GPUs by the DirectX version that they support. In what follows, I will use the following classification of GPUs.

**Pre-DX8 GPUs** These GPUs are not programmable beyond advanced texture blending capabilities, and fragment precision is limited to eight bits per channel. This class includes NVIDIA GPUs prior to the GeForce 3, and ATI GPUs prior to the Radeon 8500. Per-pixel lighting and bump mapping require multiple passes on these processors.

**DX8 GPUs** These GPUs are the first to include an assembly language for vertex processing (“vertex programs” or “vertex shaders”). Vertex programs cannot branch. Fragment precision is limited to eight bits per channel, except for some proprietary 16-bit dual channel formats. Fragment and texture processing is much more configurable, with enough functionality for simple programmability. Bump mapping and simple per-pixel lighting models can be computed in a single pass. Examples of DX8 GPUs are the ATI Radeon 8500 and NVIDIA GeForce 3.

**DX9 GPUs** These GPUs extend vertex programs to enable data-dependent branching, and add a fragment program assembly language. Fragment programs cannot branch, but support conditional writes of the result of instructions. Floating point

---

<sup>1</sup>Nevertheless, new GPU features are typically exposed earlier in OpenGL, through its standardized extension protocol.

fragment precision is now supported, although not standardized.<sup>2</sup> Complex rendering, shading, and even simulation operations can be computed in a single pass. Examples of DX9 GPUs are the NVIDIA GeForce FX 5900 Ultra and the ATI Radeon 9800.

**DX9+ GPUs** The first of these GPUs are in production as I write this, but their details have not been announced. One can speculate on the features these processors will introduce, such as branching in fragment programs, or the ability to read texture memory in vertex programs. More advanced features may include primitive- or object-level programmability, with the ability to generate vertices on the fly. Whether GPUs will move further toward general-purpose programmability or continue to add more advanced application specific functionality—for example, custom support for global illumination algorithms—remains to be seen.

#### 4.1.2 General-Purpose Computation on GPUs

The use of computer graphics hardware for general-purpose computation has been an area of active research for many years, beginning on machines like the Ikonas (England, 1978), the Pixel Machine (Potmesil and Hoffert, 1989), and Pixel-Planes 5 (Rhoades et al., 1992). The wide deployment of GPUs in the last several years has resulted in an increase in experimental research with graphics hardware. Trendall and Steward give a detailed summary of the types of computation available on modern GPUs (Trendall and Steward, 2000).

Within the realm of graphics applications, programmable graphics hardware has been used for procedural texturing and shading (Rhoades et al., 1992; Olano and Lastra, 1998; Peercy et al., 2000; Proudfoot et al., 2001). Graphics hardware has also been used for volume visualization (Cabral et al., 1994; Wilson et al., 1994; Kniss et al., 2002). Recently, new methods have been developed for using current GPUs for global illumination, including ray tracing (Carr et al., 2002; Purcell et al., 2002), photon mapping (Purcell et al., 2003), and radiosity (Carr et al., 2003; Coombe et al., 2003).

Other researchers have found ways to use graphics hardware for non-graphics applications. The use of rasterization hardware for robot motion planning was described in (Lengyel et al., 1990). (Hoff et al., 1999) described the use of z-buffer techniques for the computation of Voronoi diagrams. The PixelFlow SIMD graphics computer (Eyles et al., 1997) was used to crack UNIX password encryption (Kedem and Ishihara, 1999),

---

<sup>2</sup>The ATI Radeon 9700/9800 provides 24-bit (per channel) floating point, while the NVIDIA GeForce FX family supports 16- and 32-bit formats.

and graphics hardware has been used in the computation of artificial neural networks (Bohn, 1998).

My initial work in this area used a Coupled Map Lattice (CML) to simulate dynamic phenomena that can be described by partial differential equations. Related to this is the visualization of flows described by PDEs, which has been implemented using graphics hardware to accelerate line integral convolution and Lagrangian-Eulerian advection (Heidrich et al., 1999; Jobard et al., 2001; Weiskopf et al., 2001). Greg James of NVIDIA has demonstrated the “Game of Life” cellular automata and a 2D physically-based water simulation running on NVIDIA GPUs (James, 2001a; James, 2001b; James, 2001c). More recently, Kim and Lin used GPUs to simulate dendritic ice crystal growth (Kim and Lin, 2003), and Li et al. used them to perform Lattice Boltzmann simulation of fluid flow (Li et al., 2003).

Research on general-purpose uses of GPUs, which I call “GPGPU”, has seen a minor boom in the time since we began our work on simulation using GPUs. Strzodka showed how to combine multiple 8-bit texture channels to create virtual 16-bit precise operations (Strzodka, 2002). Level set segmentation of images and volume data on GPUs has been demonstrated by (Strzodka and Rumpf, 2001; Lefohn and Whitaker, 2002; Lefohn et al., 2003). Other recent GPGPU research includes image-based modeling (Yang et al., 2002; Hillesland et al., 2003), collision detection (Hoff et al., 2001; Govindaraju et al., 2003), and computational geometry (Mustafa et al., 2001; Krishnan et al., 2002; Guha et al., 2003; Stewart et al., 2003).

Researchers have recently embraced the power of the GPU for performing matrix computations. Larsen and McAllister used texturing operations to perform large matrix-matrix multiplies (Larsen and McAllister, 2001). This work preceded our own, and was mostly a proof-of-concept application, because they used GPUs without support for floating point textures. Thompson, et al. used the programmable vertex processor of an NVIDIA GeForce 3 GPU to solve the 3-Satisfiability problem and to perform matrix multiplication (Thompson et al., 2002). Others have used the GPU to solve sparse linear systems, using techniques such as Red-Black Jacobi iteration, Conjugate Gradient and multigrid methods (Bolz et al., 2003; Goodnight et al., 2003; Harris et al., 2003; Krüger and Westermann, 2003). These four papers also all demonstrate fluid simulation on the GPU.

This wide variety of applications demonstrates that the GPU has become an extremely powerful computational workhorse. It is especially adept at SIMD computation applied to grid or matrix data. The GPU has proven to be a nearly ideal platform for

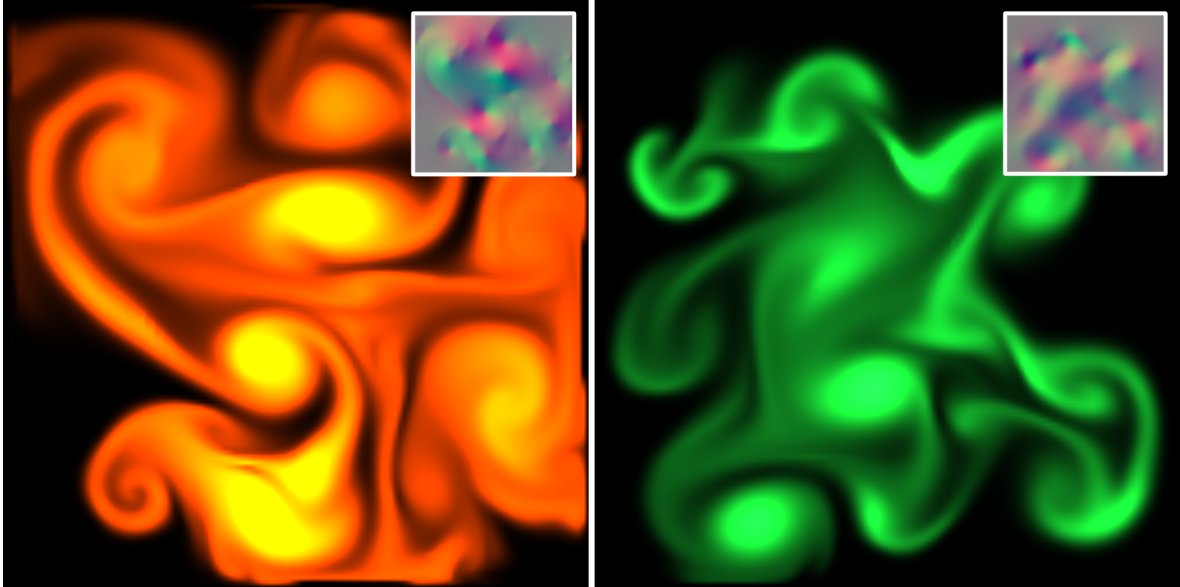


Figure 4.2: Colored “dye” carried by a swirling fluid. The inset images show the velocity field of each fluid. Velocity in the  $x$  and  $y$  directions are stored in the red and green color channels, respectively.

visual simulation of fluids, which I discuss in the following section. I extend the simulation to clouds in Chapter 5.

## 4.2 Fluid Simulation on the GPU

Clouds are only one example of fluids in nature; other examples include the flow of rivers, smoke curling from a glowing cigarette, steam rushing from a teapot, weather patterns, and the mixing of paint. All are phenomena that we would like to portray realistically in interactive graphics applications. Fluid simulation is a useful building block that is the starting point to simulating a variety of natural phenomena. Because of the large amount of parallelism in graphics hardware and the parallel nature of the computations required to simulate fluids, fluid simulation can be performed significantly faster on GPUs than on CPUs. Using an NVIDIA GeForce FX, I have achieved a two- to four-times speedup over an equivalent CPU simulation. Figure 4.2 shows some results from my simple GPU fluid simulator.

The techniques I describe are based on the “Stable Fluids” method of (Stam, 1999). However, while Stam’s simulations used a CPU implementation, I use graphics hardware because GPUs are well suited to the type of computations required by fluid simu-

lation. The simulation I describe is performed on a grid of cells. Programmable GPUs are designed to perform computations on pixels, which can be used to represent a grid of cells. GPUs achieve high performance because they contain multiple simple processors that can process several pixels in parallel. They are also optimized to perform multiple texture lookups per cycle. Because my simulation grids are stored in textures, this speed and parallelism are just what I need for fast fluid simulation.

The scope of the simulation concepts that I can cover here is necessarily limited. Cloud simulation requires simulation of a continuous volume of fluid on a two-dimensional rectangular domain, and I use these requirements to limit my discussion. I do not simulate free surface boundaries between fluids, such as the interface between sloshing water and air, because clouds are a mixture of air, water vapor, and condensed water droplets. There are many extensions to the basic techniques I use, some of which I mention later in this chapter.

### 4.2.1 The Navier-Stokes Equations

The most important quantity to represent in a fluid simulation is the velocity of the fluid, because velocity determines how the fluid moves itself and the things that are in it. I define the velocity vector field of a fluid on a Cartesian grid such that for every discrete position  $\vec{x} = (x, y)$ , there is an associated velocity at time  $t$ ,  $\vec{u}(\vec{x}, t) = (u(\vec{x}, t), v(\vec{x}, t))$ , as shown in Figure 4.3. I restrict discussion here to two dimensions for simplicity. Extension of the mathematics to three dimensions is straightforward. In the next chapter, I discuss issues in implementing 3D fluid simulations on the GPU.

The key to fluid simulation is to take steps in time, and at each time step, correctly determine the current velocity field. I do this by solving the Navier-Stokes equations for incompressible flow. Once I have the velocity field, I can do interesting things with it, like use it to move objects, smoke densities, cloud water concentrations, and other quantities that can be displayed in applications. For the sake of convenience, I repeat the Navier-Stokes equations here. Refer to Section 2.1.1 for more details.

$$\frac{\partial \vec{u}}{\partial t} = -(\vec{u} \cdot \nabla) \vec{u} - \frac{1}{\rho} \nabla p + \nu \nabla^2 \vec{u} + \vec{F} \quad (4.1)$$

$$\nabla \cdot \vec{u} = 0 \quad (4.2)$$

As described in Chapter 2, the four terms on the right-hand side of Equation 4.1 represent acceleration due to advection, pressure, diffusion, and external forces, respectively.

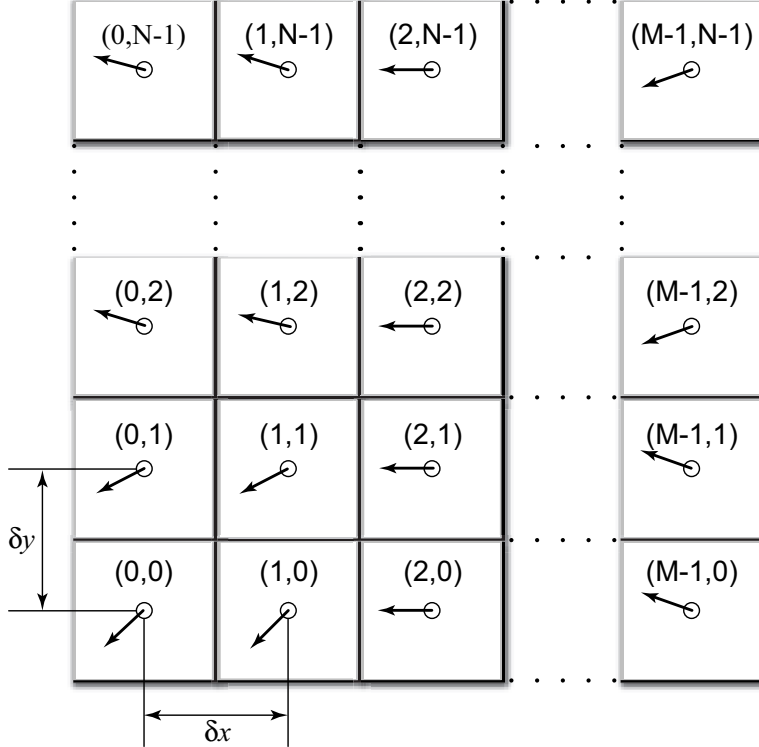


Figure 4.3: The state of the fluid simulation is represented on an  $M \times N$  grid like the one shown here. The arrows represent velocity.

I will return to the Navier-Stokes equations after a quick review of the vector calculus needed to solve them. For a detailed derivation and more details, I recommend (Chorin and Marsden, 1993) and (Griebel et al., 1998).

Visual simulation of fluids has recently been a popular topic of computer graphics research. Foster and Metaxas presented techniques for simulating the motion of hot gases (Foster and Metaxas, 1997). Stam described a stable numerical technique for interactive simulation of fluid motion (Stam, 1999). The method I use for fluid simulation on the GPU is based on Stam's algorithm. Fedkiw, et al. extended Stam's stable fluid simulation techniques to simulate realistic smoke (Fedkiw et al., 2001). My cloud simulation implements some key features of their simulation on the GPU.

#### 4.2.2 A Brief Vector Calculus Review

Equations 4.1 and 4.2 contain three different uses of the symbol  $\nabla$  (often pronounced “del”), which is also known as the *nabla* operator. The three applications of nabla are the gradient, divergence, and Laplacian operators, as shown in Table 1. The subscripts

Operator	Type	Definition	Finite Difference Form
Gradient	Scalar	$\nabla p = \left( \frac{\partial p}{\partial x}, \frac{\partial p}{\partial y} \right)$	$\nabla p = \left( \frac{p_{i+1,j} - p_{i-1,j}}{2\delta x}, \frac{p_{i,j+1} - p_{i,j-1}}{2\delta y} \right)$
Divergence	Vector	$\nabla \cdot \mathbf{u} = \frac{\partial u}{\partial x} + \frac{\partial v}{\partial y}$	$\nabla \cdot \mathbf{u} = \frac{u_{i+1,j} - u_{i-1,j}}{2\delta x} + \frac{v_{i,j+1} - v_{i,j-1}}{2\delta y}$
Laplacian	Scalar	$\nabla^2 p = \frac{\partial^2 p}{\partial x^2} + \frac{\partial^2 p}{\partial y^2}$	$\nabla^2 p = \frac{p_{i+1,j} - 2p_{i,j} + p_{i-1,j}}{(\delta x)^2} + \frac{p_{i,j+1} - 2p_{i,j} + p_{i,j-1}}{(\delta y)^2}$

Table 4.1: Vector calculus operators used in fluid simulation.

$i$  and  $j$  used in the expressions in the table refer to discrete locations on a Cartesian grid, and  $\delta x$  and  $\delta y$  are the grid spacing in the  $x$  and  $y$  dimensions, respectively (see Figure 4.3).

The gradient of a scalar field is a vector of partial derivatives of the scalar field. Divergence, which appears in Equation (4.2), has an important physical significance. It is the rate at which “density” exits a given region of space. In the Navier-Stokes equations it is applied to the velocity of the flow, and measures the net change in velocity across a surface surrounding a small piece of the fluid. Equation (4.2), the *continuity equation*, enforces the incompressibility assumption by ensuring that the fluid always has zero divergence. This means that velocity is neither created nor destroyed (except by external forces), and that momentum is conserved. The dot product in the divergence operator results in a sum of partial derivatives (rather than a vector, as with the gradient operator). This means that the divergence operator can only be applied to a vector field, such as the velocity  $\vec{u} = (u, v)$ .

Notice that the gradient of a scalar field is a vector field, and the divergence of a vector field is a scalar field. If the divergence operator is applied to the result of the gradient operator, the result is the *Laplacian* operator  $\nabla \cdot \nabla = \nabla^2$ . If the grid cells are square ( $\delta x = \delta y$ , which we assume for the remainder of this dissertation), the Laplacian simplifies to

$$\nabla^2 p = \frac{p_{i+1,j} + p_{i-1,j} + p_{i,j+1} + p_{i,j-1} - 4p_{i,j}}{(\delta x)^2} \quad (4.3)$$

The Laplacian operator appears commonly in physics, most notably in the form of diffusion equations, such as the heat equation. Equations of the form  $\nabla^2 x = b$  are known as *Poisson equations*. The case where  $b = 0$  is *Laplace’s Equation*, which is the origin of the Laplacian operator. In Equation (4.1), the Laplacian is applied to a

vector field. This is a notational simplification—the operator is applied separately to each scalar component of the vector field.

### 4.2.3 Solving the Navier-Stokes Equations

Analytical solutions of the Navier-Stokes equations can only be found for a few simple physical configurations. However, it is possible to use numerical integration techniques to solve them incrementally. My goal is to display the evolution of the flow over time, so an incremental numerical solution works well. The algorithm I use to solve the Navier-Stokes equations is based on the “stable fluids” technique described in (Stam, 1999). In this section I describe the mathematics of each step in the algorithm, following the derivations presented in (Chorin and Marsden, 1993; Stam, 1999). In Section 4.2.4 I describe my implementation on the GPU using the *Cg* shading language (Mark et al., ).

First I need to transform the equations into a form that is more amenable to numerical solution. Recall that the two-dimensional Navier-Stokes equations are three equations that we can solve for the quantities  $u$ ,  $v$ , and  $p$ . However it is not obvious how to solve them. The following section describes a transformation that leads to a straightforward algorithm.

### The Helmholtz-Hodge Decomposition

Basic vector calculus says that any vector  $\vec{v}$  can be decomposed into a set of basis vector components whose sum is  $\vec{v}$ . For example, we commonly represent vectors on a Cartesian grid as a pair of distances along the grid axes:  $\vec{v} = (x, y)$ . The same vector can be written  $\vec{v} = x\hat{i} + y\hat{j}$ , where  $\hat{i}$  and  $\hat{j}$  are unit basis vectors aligned to the axes of the grid.

In the same way that we can decompose a vector into a sum of vectors, we can also decompose a vector field into a sum of vector fields. Let  $D$  be the region in space, or in this case the plane, on which a fluid is defined. Let this region have a smooth (in other words, it has no discontinuities) boundary,  $\partial D$ , with normal direction  $\hat{n}$ . We can use the following theorem.

**Helmholtz-Hodge Decomposition Theorem** *A vector field  $\vec{w}$  on  $D$  can be uniquely decomposed in the form*

$$\vec{w} = \vec{u} + \nabla p \tag{4.4}$$

where  $\vec{u}$  has zero divergence and is parallel to  $\partial D$ ; that is,  $\vec{u} \cdot \hat{n} = 0$  on  $\partial D$ .

I use the theorem without proof. For details and a proof of this theorem, refer to Section 1.3 of (Chorin and Marsden, 1993).

This theorem states that any vector field can be decomposed into the sum of two other vector fields: a divergence-free vector field, and the gradient of a scalar field. It is a powerful tool, leading to two useful realizations.

**First Realization** Solution of the Navier-Stokes equations involves several computations to update the velocity at each time step: advection, diffusion and force application. The result is a new velocity field,  $\vec{w}$ , with *nonzero* divergence. But the continuity equation requires that each time step ends with a *divergence-free* velocity. Fortunately, the Helmholtz-Hodge Decomposition Theorem states that the divergence of the velocity can be corrected by subtracting the gradient of the pressure field:

$$\vec{u} = \vec{w} - \nabla p. \quad (4.5)$$

**Second Realization** The theorem also leads to a method for computing the pressure field. If we apply the divergence operator to both sides of Equation (4.4), we obtain

$$\nabla \cdot \vec{w} = \nabla \cdot (\vec{u} + \nabla p) = \nabla \cdot \vec{u} + \nabla^2 p.$$

But Equation (4.2) enforces that  $\nabla \cdot \vec{u} = 0$ , so this simplifies to

$$\nabla^2 p = \nabla \cdot \vec{w}, \quad (4.6)$$

which is a Poisson equation (see Section 4.2.2) for the pressure of the fluid, sometimes called the *Poisson-pressure equation*. This means that after we arrive at our divergent velocity,  $\vec{w}$ , we can solve Equation (4.6) for  $p$ , and then use  $\vec{w}$  and  $p$  to compute the new divergence free field,  $\vec{u}$ , using Equation (4.5). We return to this later.

Now we need a way to compute  $\vec{w}$ . To do this, we return to the comparison of vectors and vector fields. We know, given the definition of the dot product, that we can find the projection of a vector  $\vec{r}$  onto a unit vector  $\hat{s}$  by computing the dot product of  $\vec{r}$  and  $\hat{s}$ . The dot product is a projection operator for vectors that maps a vector  $\vec{r}$  onto its component in the direction of  $\hat{s}$ . We can use the Helmholtz-Hodge Decomposition Theorem to define a projection operator,  $\mathbb{P}$ , that projects a vector field  $\vec{w}$  onto its

divergence-free component,  $\vec{u}$ . If we apply  $\mathbb{P}$  to Equation (4.4), we get

$$\mathbb{P}\vec{w} = \mathbb{P}\vec{u} + \mathbb{P}(\nabla p).$$

However, by the definition of  $\mathbb{P}$ ,  $\mathbb{P}\vec{w} = \mathbb{P}\vec{u} = \vec{u}$ . Therefore,  $\mathbb{P}(\nabla p) = 0$ . Now we use these ideas to simplify the Navier-Stokes equations.

First, apply the new projection operator to both sides of Equation (4.1):

$$\mathbb{P} \frac{\partial \vec{u}}{\partial t} = \mathbb{P} \left( -(\vec{u} \cdot \nabla) \vec{u} - \frac{1}{\rho} \nabla p + \nu \nabla^2 \vec{u} + \vec{F} \right).$$

Because  $\vec{u}$  is divergence-free, so is the derivative on the left-hand side, so  $\mathbb{P}(\partial \vec{u}/\partial t) = \partial \vec{u}/\partial t$ . Also,  $\mathbb{P}(\nabla p) = 0$ , so the pressure term drops out. We are left with the following equation:

$$\frac{\partial \vec{u}}{\partial t} = \mathbb{P} \left( -(\vec{u} \cdot \nabla) \vec{u} + \nu \nabla^2 \vec{u} + \vec{F} \right). \quad (4.7)$$

The great thing about this equation is that it symbolically encapsulates the algorithm for simulating fluid flow. We first compute what is inside the parentheses on the right-hand side. From left to right, we compute the advection, diffusion, and force terms. Application of these three steps results in a divergent velocity field,  $\vec{w}$ , to which we apply the projection operator  $\mathbb{P}$  to get a new divergence-free field,  $\vec{u}$ . To do so, we solve Equation (4.6) for  $p$ , and then subtract the gradient of  $p$  from  $\vec{w}$  as in Equation (4.5).

In a typical implementation, the various components are not computed and added together, as in Equation (4.7). Instead, the solution is found via composition of transformations on the state; in other words, each component is a step that takes a field as input, and produces a new field as output. We can define an operator  $\mathbb{S}$  which is equivalent to the solution of Equation (4.7) over a single time step. The operator is defined as the composition of operators for advection ( $\mathbb{A}$ ), diffusion ( $\mathbb{D}$ ), force application ( $\mathbb{F}$ ), and projection ( $\mathbb{P}$ ):

$$\mathbb{S} = \mathbb{P} \circ \mathbb{F} \circ \mathbb{D} \circ \mathbb{A} \quad (4.8)$$

Thus, a step of the simulation algorithm can be expressed as  $\mathbb{S}(\vec{u}) = \mathbb{P} \circ \mathbb{F} \circ \mathbb{D} \circ \mathbb{A}(\vec{u})$ . The operators are applied right-to-left; first advection, followed by diffusion, force application and projection. This is exactly the algorithm that I describe in Section 4.2.4. Note that time is omitted above for clarity, but in practice, the time step must

be used in the computation of each operator. Next I look more closely at the advection and diffusion steps, and then approach the solution of the Poisson equations.

## Advection

Advection is the process by which a fluid’s velocity transports itself and other quantities in the fluid. To compute the advection of a quantity, we must update the quantity at each grid point. Because we are computing how a quantity moves along the velocity field, it helps to imagine that each grid cell is represented by a particle. A first attempt at computing the result of advection might be to update the grid as we would update a particle system. Just move the position,  $\vec{r}$ , of each particle forward along the velocity field the distance it would travel in time  $\delta t$ :

$$\vec{r}(t + \delta t) = \vec{r}(t) + \vec{u}(t)\delta t.$$

This is *Euler’s method*; it is a simple method for explicit (or forward) integration of ordinary differential equations. (There are more accurate methods, such as the midpoint method and the Runge-Kutta methods.)

There are two problems with this approach: The first is that simulations that use explicit methods for advection are unstable for large time steps, and can “blow up” if the magnitude of  $\vec{u}(t)\delta t$  is greater than the size of a single grid cell. The second problem is specific to GPU implementation. I implement my simulation in fragment programs, which cannot change the image-space output location of the fragments they write. This forward-integration method requires the ability to “move” the particle at each grid cell, so it cannot be implemented on current GPUs.

The solution is to invert the problem and use an implicit method (Stam, 1999). Rather than advecting quantities by computing where a particle moves over the current time step, trace the trajectory of the particle from each grid cell back in time to its former position, and copy the quantities at that position to the starting grid cell. To update a quantity  $q$  (this could be velocity, density, temperature, or any quantity carried by the fluid), use the following equation:

$$q(\vec{x}, t + \delta t) = q(\vec{x} - \vec{u}(\vec{x}, t)\delta t, t). \quad (4.9)$$

Not only is this method easily implemented on the GPU, but as Stam showed, it is stable for arbitrary time steps and velocities. Figure 4.4 depicts the advection

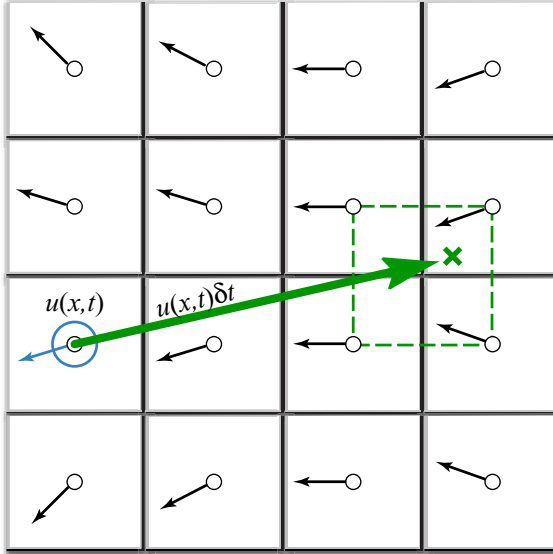


Figure 4.4: Computing fluid advection.

computation at the cell marked with a circle. Tracing the velocity field back in time leads to an ‘x.’ The four grid values nearest the ‘x’ (connected by a dashed square in the figure) are bilinearly interpolated and the result is written to the starting grid cell.

## Viscous Diffusion

As explained in Chapter 2, viscous fluids have a certain amount of resistance to flow, which results in diffusion (or dissipation) of velocity. A partial differential equation for viscous diffusion is

$$\frac{\partial \vec{u}}{\partial t} = \nu \nabla^2 \vec{u}. \quad (4.10)$$

As in advection, there are multiple ways to solve this equation. An obvious approach is to formulate an explicit, discrete form in order to develop a simple algorithm:

$$\vec{u}(\vec{x}, t + \delta t) = \vec{u}(\vec{x}, t) + \nu \delta t \nabla^2 \vec{u}(\vec{x}, t).$$

In this equation  $\nabla^2$  is the discrete form of the Laplacian operator, Equation (4.3). Like the explicit Euler method for computing advection, this method is unstable for large values of  $\delta t$  and  $\nu$  (Stam, 2003). I use Stam’s implicit formulation of Equation (4.10):

$$(\mathbf{I} - \nu \delta t \nabla^2) \vec{u}(\vec{x}, t + \delta t) = \vec{u}(\vec{x}, t). \quad (4.11)$$

Here,  $\mathbf{I}$  is the identity matrix. This formulation is stable for arbitrary time steps and viscosities. Equation (4.11) is a (somewhat disguised) Poisson equation for velocity. Remember that the use of the Helmholtz-Hodge decomposition results in a Poisson equation for pressure. These equations can be solved using an iterative relaxation technique.

## Solution of Poisson Equations

There are two Poisson equations that I must solve: the Poisson-pressure equation and the viscous diffusion equation. Poisson equations are common in physics and are well understood. I use an iterative solution technique that starts with an approximate solution and improves it every iteration.

The Poisson equation is a matrix equation of the form  $\mathbf{A}\vec{x} = \vec{b}$ , where  $\vec{x}$  is the vector of unknown values ( $p$  or  $\vec{u}$  in this case);  $\vec{b}$  is a vector of constants; and  $\mathbf{A}$  is a matrix. In the Poisson equations,  $\mathbf{A}$  is implicitly represented in the Laplacian operator  $\nabla^2$ , so it need not be explicitly stored as a matrix. Iterative solution techniques start with an initial “guess” for the solution,  $\vec{x}^{(0)}$ , and each step  $k$  produces an improved solution,  $\vec{x}^{(k)}$ . The superscript notation indicates the iteration number. The simplest iterative technique is called *Jacobi iteration*. A derivation of Jacobi iteration for general matrix equations can be found in (Golub and Van Loan, 1996).

More sophisticated methods (such as Conjugate Gradient and multigrid) converge faster, but I use Jacobi iteration because of its simplicity and ease of implementation. For details and examples of more sophisticated solvers, see (Bolz et al., 2003; Goodnight et al., 2003; Krüger and Westermann, 2003).

Equations (4.6) and (4.11) appear different, but both can be discretized using Equation (4.3) and rewritten in the form

$$x_{i,j}^{(k+1)} = \frac{x_{i-1,j}^{(k)} + x_{i+1,j}^{(k)} + x_{i,j-1}^{(k)} + x_{i,j+1}^{(k)} + \alpha b_{i,j}}{\beta}, \quad (4.12)$$

where  $\alpha$  and  $\beta$  are constants. The values of  $x$ ,  $b$ ,  $\alpha$ , and  $\beta$  are different for the two equations. In the Poisson-pressure equation,  $x$  represents  $p\delta t$ ,<sup>3</sup>  $b$  represents  $\nabla \cdot \vec{w}$ ,  $\alpha = (\delta x)^2$ , and  $\beta = 4$ . For the viscous diffusion equation,  $x$  and  $b$  both represent  $\vec{u}$ ,  $\alpha = (\delta x)^2/\nu\delta t$ , and  $\beta = 4 + \alpha$ .

---

<sup>3</sup>Note that the solution of this equation is actually  $p\delta t$ , not  $p$ . This is not a problem, because this pressure serves only to compute the pressure gradient used in the projection step. Because  $\delta t$  is constant over the grid, it does not affect the gradient.

I formulate the equations this way because it lets me use the same code to solve both equations. To solve the equations, I simply run a number of iterations in which I apply Equation (4.12) at every grid cell, using the results of the previous iteration as input to the next ( $x^{(k+1)}$  becomes  $x^{(k)}$ ). Because Jacobi iteration converges slowly, I need to execute many iterations. Fortunately, Jacobi iterations are cheap to execute on the GPU, so I can run many iterations in a very short time.

## Initial and Boundary Conditions

Any differential equation problem defined on a finite domain requires boundary conditions in order to be well-posed. The boundary conditions determine how values at the edges of the simulation domain are computed. Also, to compute the evolution of the flow over time, we must know how it started—in other words, its initial conditions. For my fluid simulation, I assume the fluid initially has zero velocity and zero pressure (that is, zero deviation from the environmental pressure) everywhere. Boundary conditions require a bit more discussion.

During each time step, I solve equations for two quantities—velocity and pressure—and I need boundary conditions for both. Because my fluid is simulated on a rectangular grid, I assume that it is a fluid in a box and cannot flow through the sides of the box. For velocity, I use the *no-slip* condition, which specifies that velocity goes to zero at the boundaries<sup>4</sup>. The correct solution of the Poisson-pressure equation requires pure Neumann boundary conditions:  $\partial p / \partial \hat{n} = 0$ . This means that at a boundary, the rate of change of pressure in the direction normal to the boundary is zero. I revisit boundary conditions at the end of Section 4.2.4.

### 4.2.4 Implementation

Now that I have described the problem and the basics of solving it, I can move forward with the implementation. A good place to start is to lay out some pseudocode for the algorithm. The algorithm is the same every time step, so this pseudocode represents a single time step. The variables  $u$  and  $p$  hold the velocity and pressure field data.

```
// Apply the first 3 operators in Equation (4.8).
u = advect(u);
u = diffuse(u);
```

---

<sup>4</sup>In cloud simulation, as I describe in Chapter 5, I use no-slip conditions only along the ground.

```

u = addForces(u);
// Now apply the projection operator to the result.
p = computePressure(u);
u = subtractPressureGradient(u, p);

```

In practice, temporary storage is needed because most of these operations cannot be performed in place. For example, the advection step in the pseudocode is more accurately written as

```

uTemp = advect(u);
swap(u, uTemp);

```

This pseudocode contains no implementation-specific details. In fact, the same pseudocode describes CPU and GPU implementations equally well. My goal is to perform all steps on the GPU. In order to clarify this type of general-purpose computation on GPUs, in the next section I make some analogies between operations in a typical CPU fluid simulation and their counterparts on the GPU.

## CPU-GPU Analogies

Fundamental to any computer are its memory and processing models, so any application must consider data representation and computation. In this section I discuss the differences between CPUs and GPUs with regard to both of these.

**Textures = Arrays** My simulation represents data on a two-dimensional grid. The natural representation for this grid on the CPU is an array. The analog of an array on the GPU is a texture. Although textures are not as flexible as arrays, their flexibility is improving as graphics hardware evolves. Textures on current GPUs support all basic operations necessary to implement a fluid simulation. Because textures usually have three or four color channels, they provide a natural data structure for vector data types with two to four components. Alternatively, multiple scalar fields can be stored in a single texture. The most basic operation is an array (or memory) read, which is accomplished by using a texture lookup. Thus, the GPU analog of an array index is a texture coordinate.

**Loop Bodies = Fragment Programs** A CPU implementation of the simulation performs the steps in the algorithm by looping, using a pair of nested loops to iterate

over each cell in the grid as in (Stam, 2003). At each cell, the same computation is performed. GPUs do not have the capability to perform this inner loop over each texel in a texture. However, the fragment pipeline is designed to perform identical computations at each fragment. To the programmer, it appears as if there is a processor for each fragment, and that all fragments are updated simultaneously. In the parlance of parallel programming, this model is known as Single Instruction Multiple Data (SIMD) computation. Thus, the GPU analog of computation inside nested loops over an array is a fragment program applied in SIMD fashion to each fragment.

**Feedback = Texture Update** In Section 4.2.3, I described how I use Jacobi iteration to solve Poisson equations. This type of iterative method uses the result of an iteration as input for the next iteration. This *feedback* is common in numerical methods. The outer loop of fluid simulation performs an iteration for each time step, and uses the results (velocity, etc.) of each iteration as input to the next.

In a CPU implementation, one typically does not even consider feedback, because it is trivially implemented using variables and arrays which can be both read and written. On the GPU, though, the output of fragment processors is always written to the frame buffer. Think of the frame buffer as a two-dimensional array that cannot be directly read. There are two ways to get the contents of the frame buffer into a texture which can be read:

1. *copy to texture* (CTT) copies from the frame buffer to a texture, and
2. *render to texture* (RTT) uses a texture as the frame buffer so the GPU can write directly to it.

CTT and RTT function equally well, but have a performance tradeoff. For the sake of generality, I do not assume the use of either, and refer to the process of writing to a texture as a *texture update*.

I mentioned earlier that, in practice, each of the five steps in the algorithm updates a temporary grid and then performs a swap. RTT requires the use of two textures to implement feedback, because rendering to a texture while it is bound for reading is illegal (under the current specification (Poddar and Womack, 2001)). The swap in this case is merely a swap of texture IDs. The performance cost of RTT is therefore constant. CTT, on the other hand, requires only one texture. The frame buffer acts as a temporary grid, and a swap is performed by copying the data from the frame buffer to the texture. The performance cost of this copy is proportional to the texture size.

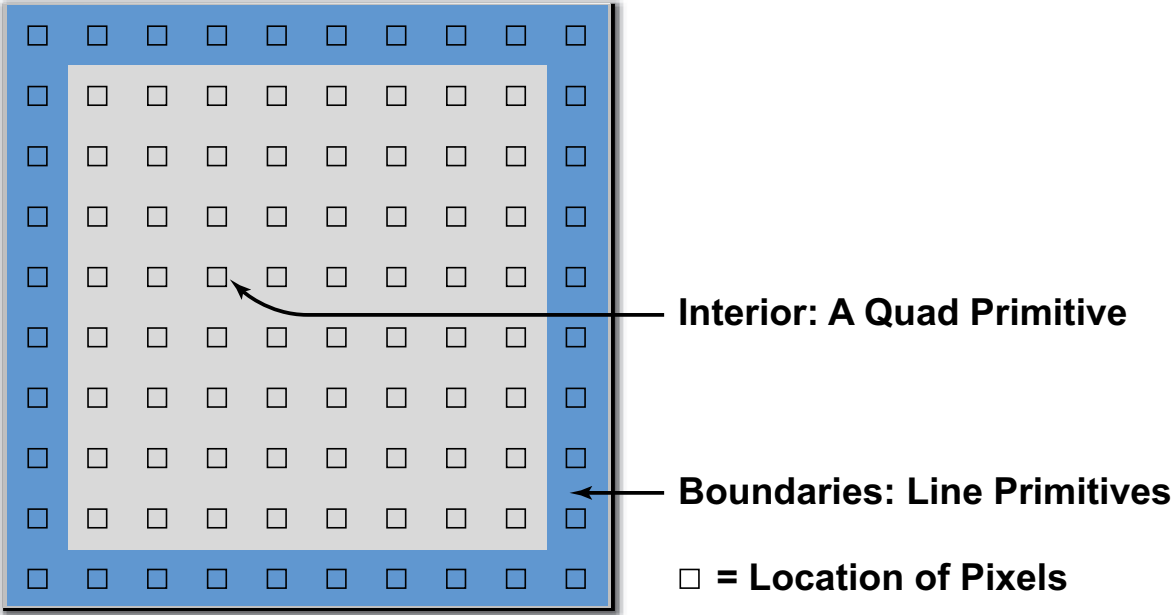


Figure 4.5: Updating a grid involves rendering a quad for the interior and lines for the boundaries. Separate fragment programs are applied to interior and border fragments.

## Slab Operations

I break down the steps of my simulation into what I call *slab operations*<sup>5</sup> (“slabop,” for short). Each slabop consists of processing one or more (often all) fragments in the frame buffer—usually with a fragment program active—followed by a texture update. Fragment processing is driven by rendering geometric primitives. For this application, the geometry I render is simple—just quad and line primitives.

There are two types of fragments to process in any slab operation: interior fragments and boundary fragments. My 2D grid reserves a single-cell perimeter to store and compute boundary conditions. Typically a different computation is performed on the interior and at the boundaries. To update the interior fragments, I render a quadrilateral primitive that covers all but a one-pixel border on the perimeter of the frame buffer. I render four line primitives to update the boundary cells. I apply separate fragment programs to interior and border fragments (see Figure 4.5).

---

<sup>5</sup>I call them slab operations because GPU simulation in 3D requires the 3D grid to be divided into a stack of 2D “slabs”, because the frame buffer is limited to two dimensions.

## Implementation in Fragment Programs

Now that I have described the steps of the algorithm, the data representation, and how to perform a slab operation, I can write the fragment programs that perform computations at each cell.

**Advection** The fragment program implementation of advection follows nearly exactly from Equation (4.9). There is one slight difference. Because texture coordinates are not in the same units as the simulation domain (the texture coordinates are in the range  $[0, N]$ , where  $N$  is the grid resolution), I must scale the velocity into grid space. This is reflected in the *Cg* code in Listing 4.1 with the multiplication of the local velocity by the parameter `rdx`, which represents the reciprocal of the grid scale  $\delta x$ . The texture wrap mode must be set to `CLAMP` so that back-tracing outside the range  $[0, N]$  will be clamped to the boundary texels. The boundary conditions described later correctly update these texels so that this situation operates correctly.

In this code, the parameter `u` is the velocity field texture, and `x` is the field that is to be advected. This could be the velocity or another quantity, such as dye concentration. The function `f4texRECTbilerp()` is a utility function that performs bilinear interpolation of the four texels closest to the texture coordinates passed to it. Because current GPUs do not support automatic bilinear interpolation in floating point textures, it must be implemented directly in the code.

**Viscous Diffusion** With the description of the Jacobi iteration technique given in Section 4.2.3, writing a Jacobi iteration fragment program is simple, as shown in Listing 4.2.

Notice that the `rBeta` parameter is the reciprocal of  $\beta$  from Section 4.2.3. To solve the diffusion equation, set `alpha` to  $(\delta x)^2/\nu\delta t$ , `rBeta` to  $1/(4 + (\delta x)^2/\nu\delta t)$ , and the `x` and `b` parameters to the velocity texture. Then, run a number of iterations (usually I use 20 to 50, but more can be used to reduce the error).

**Force Application** The simplest step in the algorithm is computing the acceleration caused by external forces. In my simple 2D fluid simulation, the user can apply an impulse to the fluid by clicking and dragging with the mouse. To implement this, I draw a spot into the velocity texture at the position of the click. The color of the

```

void advect(float2      coords : WPOS,    // grid coordinates
           out float4     xNew : COLOR,   // advected qty

           uniform float      timestep,
           uniform float      rdx,          // 1 / grid scale.
           uniform samplerRECT u,          // input velocity
           uniform samplerRECT x)          // qty to advect.

{
    // follow the velocity field ‘‘back in time’’
    float2 pos = coords - timestep * rdx * f2texRECT(u, coords);

    // Interpolate and write to the output fragment.
    xNew = f4texRECTbilerp(x, pos);
}

```

Listing 4.1: Advection *Cg* program.

```

void jacobi(half2      coords : WPOS,    // grid coordinates
            out half4     xNew : COLOR,   // result

            uniform half      alpha,
            uniform half      rBeta,        // reciprocal beta
            uniform samplerRECT x,          // x vector (Ax = b)
            uniform samplerRECT b)          // b vector (Ax = b)

{
    // left , right , bottom , and top x samples
    half4 xL = h4texRECT(x, coords - half2(1, 0));
    half4 xR = h4texRECT(x, coords + half2(1, 0));
    half4 xB = h4texRECT(x, coords - half2(0, 1));
    half4 xT = h4texRECT(x, coords + half2(0, 1));

    // b sample , from center
    half4 bC = h4texRECT(b, coords);

    // evaluate jacobi iteration
    xNew = (xL + xR + xB + xT + alpha * bC) * rBeta;
}

```

Listing 4.2: Jacobi iteration *Cg* program.

spot encodes the direction and magnitude of the impulse: the red channel contains the magnitude in  $x$ , and the green channel contains the magnitude in  $y$ . The spot is actually a two-dimensional Gaussian “splat.”

I use a fragment program to check each fragment’s distance from the impulse position and compute a quantity  $\vec{c}$  which is added to the velocity texture:

$$\vec{c} = \vec{F}\delta t \cdot e^{-[(x-x_p)^2 + (y-y_p)^2]/r}$$

Here,  $\vec{F}$  is the force computed from the direction and length of the mouse drag,  $r$  is the desired impulse radius, and  $(x, y)$  and  $(x_p, y_p)$  are the fragment position and impulse (click) position in window coordinates, respectively.

**Projection** In Section 4.2.3 I described how the projection step is divided into two operations: solving the Poisson-pressure equation for  $p$ , and subtracting the gradient of  $p$  from the intermediate velocity field. This requires three fragment programs: the Jacobi iteration program given previously, a program to compute the divergence of the intermediate velocity field, and a program to subtract the gradient of  $p$  from the intermediate velocity field.

The divergence program in Listing 4.3 takes the intermediate velocity field as parameter **w**, and the reciprocal of the grid scale as parameter **rdx**, and computes the divergence according to the finite difference formula given in Table 4.2.2.

The divergence is written to a temporary texture, which is then used as input to the **b** parameter of the Jacobi iteration program. The **x** parameter of the Jacobi program is set to the pressure texture, which is first cleared to all zero values (in other words, I use zero as an initial guess for the pressure field). The **alpha** and **rBeta** parameters are set to  $(\delta x)^2$  and  $1/4$ , respectively.

To achieve good convergence on the solution, I typically use 40 to 80 Jacobi iterations. Through experimentation, I have found that this results in visually convincing behavior, and that using more iterations does not provide much visual improvement. Section 5.4.1 provides more details about the solvers I use for cloud simulation.

After the Jacobi iterations are finished, I bind the pressure field texture to the parameter **p** in the program in Listing 4.4, which computes the gradient of  $p$  according to the definition in Table 4.2.2 and subtracts it from the intermediate velocity field texture in parameter **w**.

```

void divergence(half2      coords : WPOS,    // grid coordinates
                out half4      div     : COLOR,   // divergence (output)
                uniform half     halfrdx,   // 0.5 / gridscale
                uniform samplerRECT w)        // vector field
{
    half4 vL = h4texRECT(w, coords - half2(1, 0));
    half4 vR = h4texRECT(w, coords + half2(1, 0));
    half4 vB = h4texRECT(w, coords - half2(0, 1));
    half4 vT = h4texRECT(w, coords + half2(0, 1));

    div = halfrdx * ((vR.x - vL.x) + (vT.y - vB.y));
}

```

Listing 4.3: Divergence *Cg* program.

```

void gradient(half2      coords : WPOS,    // grid coordinates
              out half4     uNew    : COLOR,   // new velocity (output)
              uniform half     halfrdx,   // 0.5 / gridscale
              uniform samplerRECT p,       // pressure
              uniform samplerRECT w)        // velocity
{
    half pL = h1texRECT(p, coords - half2(1, 0));
    half pR = h1texRECT(p, coords + half2(1, 0));
    half pB = h1texRECT(p, coords - half2(0, 1));
    half pT = h1texRECT(p, coords + half2(0, 1));

    uNew = h4texRECT(w, coords);
    uNew.xy -= halfrdx * half2(pR - pL, pT - pB);
}

```

Listing 4.4: *Cg* program to subtract the pressure gradient.

```

void boundary(half2      coords : WPOS,    // grid coordinates
              half2      offset : TEX1,    // boundary offset
              out half4     bv       : COLOR,   // output value
              uniform half      scale,     // scale parameter
              uniform samplerRECT x)           // state field
{
    bv = scale * h4texRECT(x, coords + offset);
}

```

Listing 4.5: Boundary condition *Cg* program.

**Boundary Conditions** Section 4.2.3 explains that my “fluid in a box” requires no-slip (zero) velocity boundary conditions and pure Neumann pressure boundary conditions. In Section 4.2.4 I showed how I implement boundary conditions by reserving the one-pixel perimeter of the grid for storing boundary values. I update these values by drawing line primitives over the border, using a fragment program that sets the values appropriately.

The grid discretization affects the computation of boundary conditions. The no-slip condition dictates that velocity equals zero at the boundaries, and the pure Neumann pressure condition requires the normal pressure derivative to be zero at the boundaries. The boundary is defined to lie on the edge between the boundary cell and its nearest interior cell, but grid values are defined at cell centers. Therefore, boundary values must be computed such that the average of the two cells adjacent to any edge satisfies the boundary condition.

The equation for the velocity boundary on the left side, for example, is

$$\frac{\vec{u}_{0,j} + \vec{u}_{1,j}}{2} = 0, \quad (4.13)$$

for  $j \in [0, N]$ , where  $N$  is the grid resolution. In order to satisfy this equation,  $u_{0,j}$  must be set equal to  $-u_{1,j}$ . The pressure equation works out similarly. Using the forward difference approximation of the derivative,

$$\frac{p_{1,j} - p_{0,j}}{\delta x} = 0. \quad (4.14)$$

In order to satisfy this equation,  $p_{0,j}$  must be set equal to  $p_{1,j}$ . The other three boundaries are handled in the same way.

I use the fragment program in Listing 4.5 to implement both types of boundary

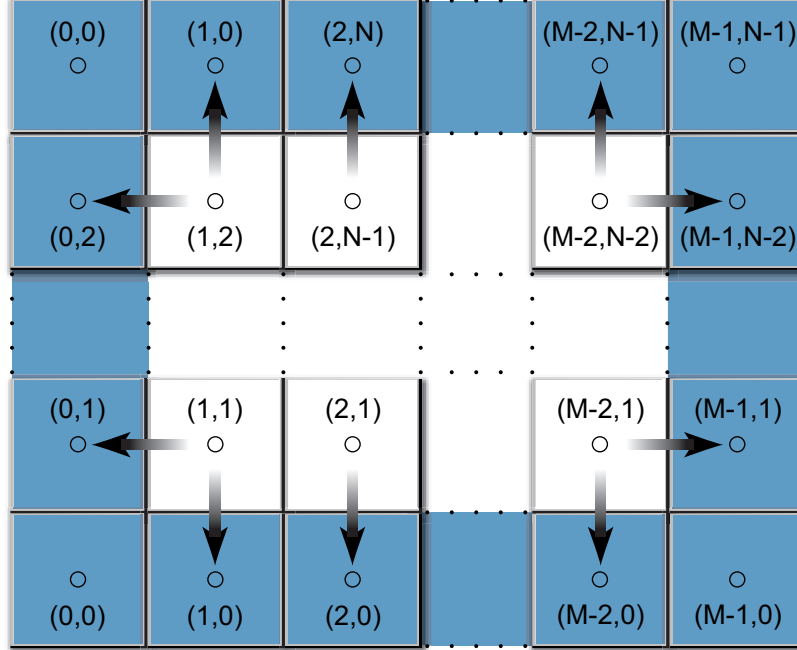


Figure 4.6: Boundary Conditions on an  $M \times N$  Grid. The arrows indicate how offsets are used to copy values from just inside the boundaries to the boundary cells.

conditions. Figure 4.6 demonstrates how the program works. The `x` parameter represents the texture (velocity or pressure) from which interior values are read. The `offset` parameter contains the correct offset to the interior cells adjacent to the current boundary. The `coords` parameter contains the position in texture coordinates of the fragment being processed, so adding `offset` to it addresses a neighboring texel. At each boundary, I set `offset` to adjust the texture coordinates to address the texel just inside the boundary. For the left boundary, I set it to  $(1, 0)$  so that it addresses the texel just to the right; for the bottom boundary, I use  $(0, 1)$ , and so on. The `scale` parameter can be used to scale the value copied to the boundary. For velocity boundaries, `scale` is set to  $-1$ , and for pressure it is set to  $1$ , to correctly implement Equations (4.13) and (4.14), respectively.

#### 4.2.5 Performance

In my tests, the results of which are shown in Figure 4.7, the basic fluid simulator presented in this chapter runs about twice as fast on an NVIDIA GeForce FX 5900 Ultra GPU as it does on an Intel Pentium 4 CPU (2GHz). The bottleneck of the simulation is iterative solution of the poisson-pressure equation. In Section 5.4.1, I

describe a *vectorized* Jacobi solver which performs fewer operations per iteration by packing four neighboring pressure values into each RGBA (Red, Green, Blue, Alpha) texel and updating them simultaneously. As shown in Figure 4.7, this increases the speedup of the GPU simulation to up to five times faster than the CPU.

## 4.2.6 Applications

In this section I discuss a variety of applications of the GPU fluid simulation techniques.

### Simulating Liquids and Gases

The most direct use of the simulation techniques is to simulate a continuous volume of liquid or gas. As it stands, the simulation only represents the velocity of the fluid, which is not very interesting. It is more interesting if there is something else in the fluid. My fluid and cloud simulations do this by maintaining additional scalar fields. In my simple 2D fluid simulation (shown in Figure 4.2), this field represents the concentration of dye carried by the fluid. (Because it is an RGB texture, it is really three scalar fields—one for each of the three dye colors.) Quantities like this are known as *passive scalars* because they are carried along by the fluid, but do not affect how it flows.

If  $d$  is the concentration of dye, then in conjunction with the Navier-Stokes equations, the evolution of the dye field is governed by the following equation:

$$\frac{\partial d}{\partial t} = -(\vec{u} \cdot \nabla)d.$$

To simulate how the dye is carried by the fluid, I apply the advection operator to the scalar field, just as I do for the velocity. If I also want to account for the diffusion of the dye in the fluid, I can add a diffusion term:

$$\frac{\partial d}{\partial t} = -(\vec{u} \cdot \nabla)d + \gamma \nabla^2 d + S \quad (4.15)$$

where  $\gamma$  is the coefficient of the diffusion of dye in the liquid. To implement dye diffusion, Jacobi iteration can be used just as it is used for viscous diffusion of velocity. I added another term to Equation (4.15),  $S$ . This term represents any sources of dye. I implement this term in the same way as external forces on the velocity—by adding dye wherever the user clicks.

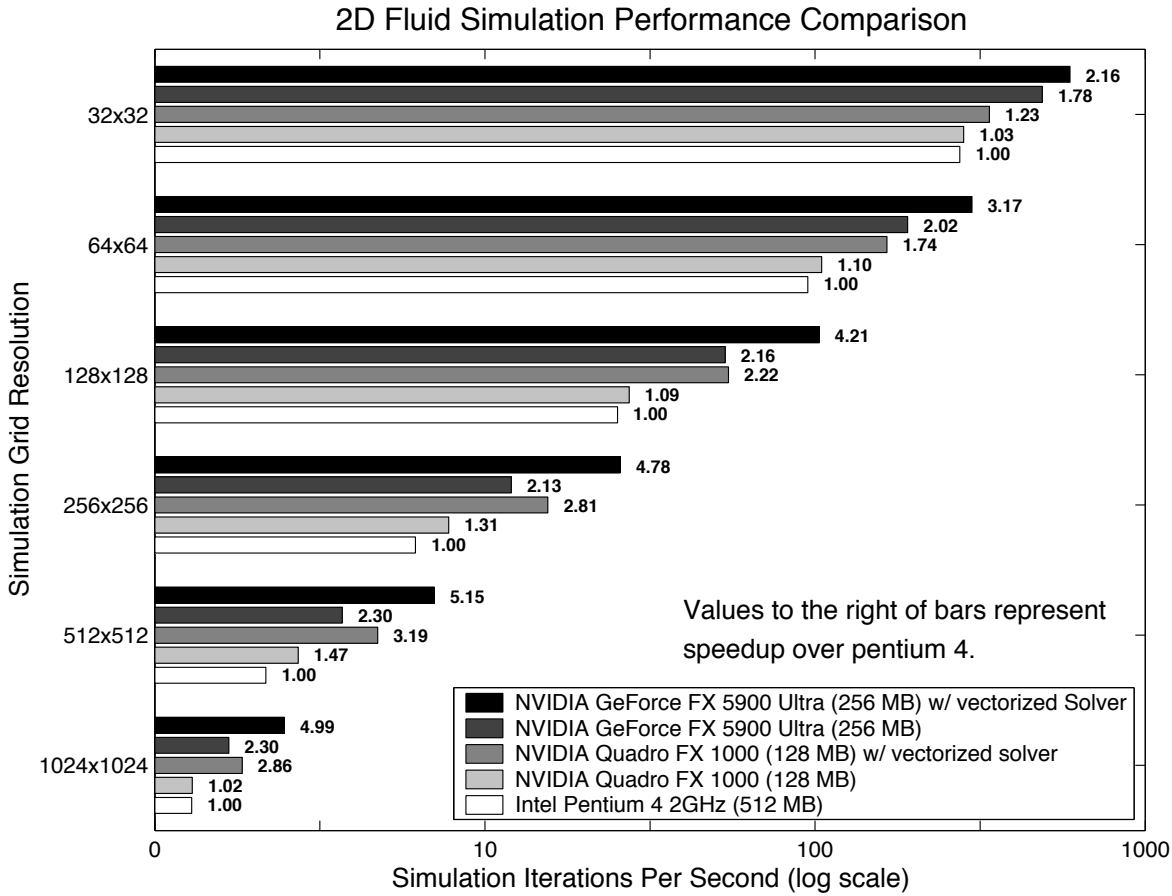


Figure 4.7: A comparison of two-dimensional fluid simulation performance on various GPUs and a CPU. The lengths of the bars represent the execution speed, in iterations per second, of the simulation running on each processor at a variety of resolutions. For comparison, the speedup each processor achieves over a 2 GHz Pentium 4 CPU is printed at the end of each bar. Two different poisson solvers were used on the GPUs. The first is the basic Jacobi solver presented in this chapter. The second is a faster, vectorized Jacobi solver that is described in Section 5.4.1. In these tests, the Jacobi solver was run for 40 iterations at each time step.

## Buoyancy and Convection

Temperature is an important factor in the flow of many fluids. Convection currents are caused by the changes in density associated with temperature changes. These currents affect our weather, our oceans and lakes, and even our coffee. To simulate these effects, I need to add buoyancy to my simulation.

A simple way to incorporate buoyancy is to add a scalar field for temperature,  $T$ , and a buoyancy operator that adds force where the local temperature is higher than a given ambient temperature,  $T_0$ :

$$f_{buoy} = \sigma(T - T_0)\hat{k}. \quad (4.16)$$

In this equation,  $\hat{k}$  is the vertical direction and  $\sigma$  is a constant scale factor. This force can be implemented in a simple fragment program that evaluates Equation (4.16) at each fragment, scales the result by the time step, and adds it to the current velocity.

## Smoke

At this point, my fluid simulation has almost everything it needs to simulate smoke. What I have presented so far is similar to the smoke simulation technique originally presented by (Fedkiw et al., 2001). In addition to calculating the velocity and pressure fields, a smoke simulation must maintain scalar fields for smoke density,  $d$ , and temperature,  $T$ . The smoke density is advected by the velocity field, just like the dye I described earlier. The buoyant force is modified to account for the gravitational pull on dense smoke:

$$f_{buoy} = (-\kappa d + \sigma(T - T_0))\hat{k},$$

where  $\kappa$  is a constant mass scale factor.

By adding a source of smoke density and heat (possibly representing a smoke stack or the tip of a cigarette) at a given location on the grid, smoke can be simulated. The paper by Fedkiw et al. describes two other differences from my basic simulation. They use a staggered grid to improve accuracy, and add a vorticity confinement force to increase the amount of swirling motion in the smoke. I use both of these techniques in my cloud simulation, which I describe in Chapter 5 along with extension to three dimensions.

### 4.2.7 Extensions

The fluid simulation presented in this section is a building block that can serve as the basis for more complex simulations. There are many ways to extend this basic simulation. I describe two of them here.

### 4.2.8 Vorticity Confinement

Fluids such as smoke and convective clouds typically contain rotational flows at a variety of scales. As Fedkiw et al. explained, numerical dissipation caused by simulation on a coarse grid damps out these interesting features (Fedkiw et al., 2001). Therefore, they used *vorticity confinement* to restore these fine-scale motions. Overby, et al. also used vorticity confinement in their cloud simulation (Overby et al., 2002), as do I. Vorticity confinement works by first computing the vorticity,  $\vec{\psi} = \nabla \times \vec{u}$ . From the vorticity a normalized vorticity gradient field  $\vec{\Psi}$  is computed:

$$\vec{\Psi} = \frac{\vec{\eta}}{|\vec{\eta}|}.$$

Here  $\vec{\eta} = \nabla |\vec{\psi}|$ . The vectors in this vector field point from areas of lower vorticity to areas of higher vorticity. The vorticity confinement force is computed from this field:

$$\vec{f}_{vc} = \varepsilon \delta x (\vec{\Psi} \times \vec{\psi}) \quad (4.17)$$

Here,  $\varepsilon$  is a user-controlled scale parameter and  $\delta x$  is the grid scale.  $\vec{f}_{vc}$  is applied (just like any other force) to the velocity field to restore the dissipated vorticity.

## Arbitrary Boundaries

I assumed previously that the fluid exists in a rectangular box with flat, solid sides. If boundaries of arbitrary shape and location are important, the simulation must account for these boundaries. Incorporating arbitrary boundaries requires applying the boundary conditions (discussed in Section 4.2.3) at arbitrary locations. This means that at each cell, the direction in which the boundaries lie must be determined in order to compute the correct boundary values. This requires more decisions to be made at each cell, leading to a slower and more complicated simulation. In fact, on a three-dimensional grid there are 26 neighboring cells to check. That may be very expensive

on current GPUs that do not support true branching in fragment programs.<sup>6</sup> Future GPUs will likely support branching in fragment programs, though, making such a technique more useful. Many interesting effects can be created this way, such as smoke flowing around obstacles, or fog rolling over land. Moving boundaries can even be incorporated, as in (Fedkiw et al., 2001). Refer to that paper as well as (Griebel et al., 1998) for implementation details.

### Free Surface Flow

Another assumption I made previously is that the fluid is continuous—the only boundaries I represent are the solid boundaries of the box. Therefore I cannot simulate things like the ocean surface, where there is an interface between the water and air. This type of interface is called a free surface. Extending the simulation to incorporate a free surface requires tracking the location of the surface as it moves through cells. Methods for implementing free surface flow can be found in (Griebel et al., 1998). As with arbitrary boundaries, this technique also requires more computation than simple continuous fluid simulation, but it is certainly implementable on current GPUs, and will become more efficient on future GPUs.

## 4.3 Simulation Techniques for DX8 GPUs

DX9 GPUs support floating point computation and storage and are fully programmable via rich vertex and fragment assembly languages. This functionality enables the type of computations described in the previous section. In contrast, DX8 graphics processors such as the NVIDIA GeForce 3 had limited programmability and supported only fixed point texture values and fragment computations. The vertex unit of DX8 GPUs has a complete assembly language, but fragment programmability consists of APIs that enable configuration of a number of switches. The wide array of texture addressing and blending modes that these switches control provides many output combinations, but the programming model is extremely rigid. Mapping complex algorithms onto these processors requires clever tricks with textures and coordinates that can often result in hard to find bugs.

The limitations of DX8 GPUs mean that they cannot be used to accurately solve real systems of PDEs, such as the fluid dynamics equations discussed in the previous

---

<sup>6</sup>However, I believe the decisions can probably be implemented using masking rather than branching.

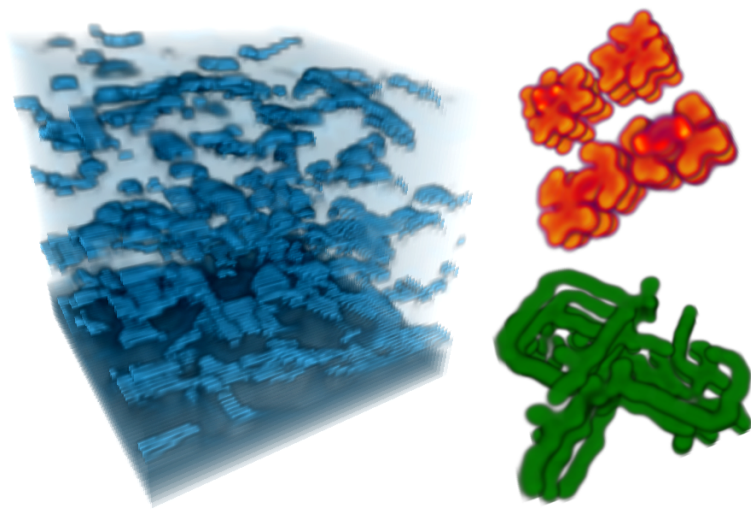


Figure 4.8: 3D coupled map lattice simulations running on a DX8 GPU. Left: boiling. Right: chemical reaction-diffusion.

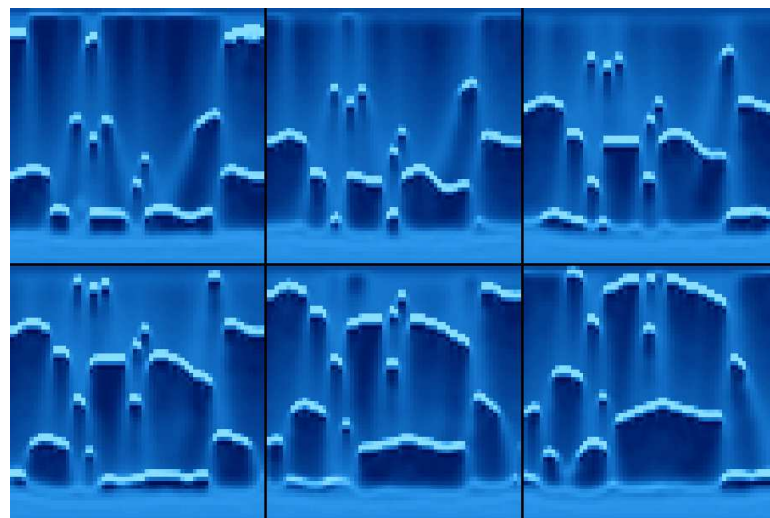


Figure 4.9: A sequence of stills (10 iterations apart) from a 2D boiling simulation running on DX8 graphics hardware.

section. For completeness, in this section I discuss the results of our attempts at performing a limited type of physically-based simulation on DX8 graphics hardware. I collaborated with Greg Coombe, Thorsten Scheuermann, and Anselmo Lastra on this work (Harris et al., 2002).

A recent approach to the simulation of dynamic phenomena, the *coupled map lattice*, uses a set of simple local operations to model complex global behavior (Kaneko, 1993). When implemented using computer graphics hardware, coupled map lattices (CML) provide a simple, fast and flexible method for the visual simulation of a wide variety of dynamic systems and phenomena. In this section I describe the implementation of CML systems with DX8-class graphics hardware, and demonstrate the flexibility and performance of these systems by presenting several fast interactive 2D and 3D visual simulations. Our CML boiling simulation runs at speeds ranging from 8 iterations per second for a 128x128x128 3D lattice to over 1700 iterations per second for a 64x64 2D lattice on an NVIDIA GeForce 4 GPU.

### 4.3.1 CML and Related Work

A coupled map lattice is a mapping of continuous dynamic state values to nodes on a lattice that interact (are ‘coupled’) with a set of other nodes in the lattice according to specified rules. Coupled map lattices were developed by Kaneko for the purpose of studying spatio-temporal dynamics and chaos (Kaneko, 1993). Since their introduction, CML techniques have been used extensively in the fields of physics and mathematics for the simulation of a variety of phenomena, including boiling (Yanagita, 1992), convection (Yanagita and Kaneko, 1993), cloud dynamics (Yanagita and Kaneko, 1997), chemical reaction-diffusion (Kapral, 1993), and the formation of sand ripples and dunes (Nishimori and Ouchi, 1993). CML techniques were recently introduced to the field of computer graphics for the purpose of cloud modeling and animation (Miyazaki et al., 2001). Lattice Boltzmann computation is a similar technique that has been used for simulating fluids, particles, and other classes of phenomena (Qian et al., 1996). Li et al. recently implemented a Lattice Boltzmann fluid simulation on a DX8-class GPU (Li et al., 2003).

A cellular automaton (CA) is a grid of discrete-state cells whose state evolves over discrete time steps according to a set of rules based on the states of neighboring cells (von Neumann, 1966; Wolfram, 1984; Toffoli and Margolus, 1987). A CML is an extension of a CA in which the discrete state values of CA cells are replaced with

continuous real values. Like CA, CML are discrete in space and time and are a versatile technique for modeling a wide variety of phenomena. Methods for animating cloud formation using cellular automata were presented in (Nagel and Raschke, 1992; Dobashi et al., 2000). Discrete-state automata typically require very large lattices in order to simulate real phenomena, because the discrete states must be filtered in order to compute real values. By using continuous-valued state, a CML is able to represent real physical quantities at each of its nodes.

While a CML model can certainly be made both numerically and visually accurate (Kaneko, 1993), the low precision of the DX8 GPUs that we used made accurate numerical simulation difficult. Therefore, our goal was instead to implement visually accurate simulation models on graphics hardware, under the assumption that continuing improvement in the speed and precision of graphics hardware would allow numerically accurate simulation in the near future.

The systems that have been found to be most amenable to CML implementation are multidimensional initial-value partial differential equations (Kaneko, 1993). These are the governing equations for a wide range of phenomena from fluid dynamics to reaction-diffusion. Based on a set of initial conditions, the simulation evolves forward in time. The only requirement is that the equation must first be explicitly discretized in space and time, which is a standard requirement for conventional numerical simulation. This flexibility means that the CML can serve as a model for a wide class of dynamic systems.

## A CML Simulation Example

To illustrate CML, I describe the boiling simulation of (Yanagita, 1992). The state of this simulation is the temperature of a liquid. A heat plate warms the lower layer of liquid, and temperature is diffused through the liquid. As the temperature reaches a threshold, the phase changes and “bubbles” of high temperature form. When phase changes occur, newly formed bubbles absorb latent heat from the liquid around them, and temperature differences cause them to float upward under buoyant force.

Yanagita implements this global behavior using four local CML operations: diffusion, phase change, buoyancy, and latent heat. Each of these operations can be written as a simple equation. Figures 4.8, 4.9 and 4.13 show this simulation running on graphics hardware, and Section 4.3.6 gives details of our implementation. I will use this boiling simulation as an example throughout this section.

### 4.3.2 Common Operations

A detailed description of the implementation of the specific simulations that we modeled using CML would require too much space, so I instead describe a few common CML operations, followed by details of their implementation. My goal in these descriptions is to impart a feel for the kinds of operations that can be performed on DX8 GPUs. The example equations used in this section assume a two-dimensional lattice. Extension to three dimensions is straightforward.

#### Diffusion and the Laplacian

The Laplacian, described in Section 4.2.2, appears often in the partial differential equations that describe natural phenomena. It is an isotropic measure of the second spatial derivative of a scalar function. Intuitively, it can be used to detect regions of rapid change, and for this reason it is commonly used for edge detection in image processing. The Laplacian appears in all of the CML simulations that we implemented. The boiling simulation described previously includes a thermal diffusion operation. We implement this using an explicit form of the diffusion operator. The low precision of GeForce 3 fragment processing would cause excessive error to build up over multiple steps of an iterative, implicit procedure. Also, because the diffusion coefficient required by the boiling simulation is very small, instability is not a concern.

It is not possible on DX8 hardware to write a short fragment program to perform computations such as the Laplacian. The *Cg* programs in Section 4.2.4 address neighboring fragments by simply adding offsets to the texture coordinates. For example, the vector `coords-half2(1,0)` represents the coordinates of the fragment just to the left of the current fragment position. On DX9 GPUs, a single texture can be bound and read multiple times using different computed texture coordinates.

To implement the same offset on a DX8 GPU, the offset must be applied before the coordinates reach the fragment end of the pipeline. The texture coordinates of each vertex must be offset so that the rasterized coordinates at each fragment will also be offset. To sample one texture multiple times using different coordinates, the same texture must be bound to multiple texture units, and different offset texture coordinates must be provided to each texture unit. Finally, to perform the arithmetic that combines these samples, texture blending operations must be configured to blend the results of the multiple texture units. To say the least, programming DX8 hardware is not straightforward.

## Directional Forces

Most dynamic simulations involve the application of force. Like all operations in a CML model, forces are applied via computations on the state of a node and its neighbors. As an example, I describe a buoyancy operator used in convection and cloud formation simulations (Miyazaki et al., 2001; Yanagita and Kaneko, 1993; Yanagita and Kaneko, 1997).

This buoyancy operator uses temperature state  $T$  to compute a buoyant velocity at a node and add it to the node's vertical velocity state,  $v$ :

$$v'_{i,j} = v_{i,j} + \frac{c_b}{2} (2T_{i,j} - T_{i+1,j} - T_{i-1,j}).$$

The subscripts represent the grid coordinates of the values. This equation expresses that a node is buoyed upward if it is warmer than its horizontal neighbors, and pushed downward if it is cooler. The strength of the buoyancy is controlled via the parameter  $c_b$ .

## Computation on Neighbors

Sometimes an operation requires more complex computation than the arithmetic of the simple buoyancy operation described above. The buoyancy operation of the boiling simulation described in Section 4.3.1 must also account for phase change, and is therefore more complicated:

$$\begin{aligned} T'_{i,j} &= T_{i,j} - \frac{c_b}{2} T_{i,j} [\rho(T_{i,j+1}) - \rho(T_{i,j-1})], \\ \rho(T) &= \tanh [\alpha(T - T_c)]. \end{aligned}$$

Here,  $c_b$  is the buoyancy strength coefficient,  $\alpha$  is a constant that scales the phase change range, and  $\rho(T)$  is an approximation of density relative to temperature,  $T$ . The hyperbolic tangent is used to simulate the rapid change of density of a substance around the phase change temperature,  $T_c$ . A change in density of a lattice node relative to its vertical neighbors causes the temperature of the node to be buoyed upward or downward. The thing to notice in this equation is that simple arithmetic will not suffice—the hyperbolic tangent function must be applied to the temperature at the neighbors above and below node  $(i, j)$ . I discuss how to compute arbitrary functions using dependent texturing in Section 4.3.4.

### 4.3.3 State Representation and Storage

Section 4.2.4 describes how textures are used for state field storage. On DX8 GPUs, the frame buffer and textures are limited to storage of 8-bit unsigned integers,<sup>7</sup> so state values must be converted to this format before being written to texture. Physical simulation also requires the use of signed values. Most texture storage, however, uses unsigned fixed point values. Although fragment-level programmability available in these GPUs uses signed arithmetic internally, the unsigned data stored in the textures must be biased and scaled before and after processing.

### 4.3.4 Implementing CML Operations

An iteration of a CML simulation consists of successive application of simple operations on the lattice. These operations consist of three steps: setup the graphics hardware rendering state, render a single quadrilateral fit to the view port, and store the rendered results into a texture. I refer to each of these setup-render-copy operations as a single *pass*. In practice, due to limited GPU resources (for example, the number of texture units), a CML operation may span multiple passes.

The setup portion of a pass simply sets the state of the hardware to correctly perform the rest of the pass. Interior and boundary fragments can be processed in the same manner as described in Section 4.2.4 for the latest GPUs.

The render-copy portion of each pass performs 4 suboperations: *Neighbor Sampling*, *Computation on Neighbors*, *New State Computation*, and *State Update*. Figure 4.10 illustrates the mapping of the suboperations to graphics hardware. Neighbor sampling and Computation on Neighbors are performed by the configurable texture mapping hardware. New State Computation performs arithmetic on the results of the previous suboperations using programmable texture blending. Finally, State Update feeds the results of one pass to the next by rendering or copying the texture blending results to a texture. State Update is performed using either copy to texture or render to texture, as I described in Section 4.2.4.

**Neighbor Sampling** Since state is stored in textures, neighbor sampling is performed by offsetting texture coordinates toward the neighbors of the texel being updated. For example, to sample the four nearest neighbor nodes of node  $(i, j)$ , the

---

<sup>7</sup>While two-channel, 16-bit textures are available on these GPUs, they do not support dynamic texture updates for this format.

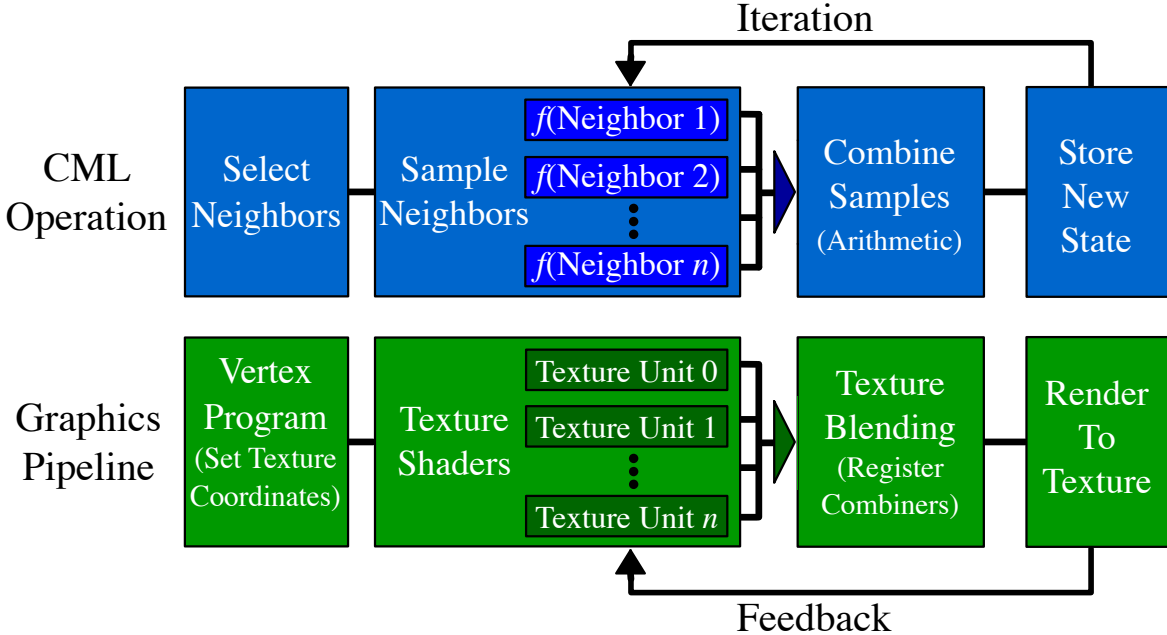


Figure 4.10: Components of a CML operation map to graphics hardware pipeline components.

texture coordinates at the corners of the quadrilateral rendered over the viewport are offset in the direction of each neighbor by the width of a single texel. Texture coordinate interpolation ensures that as rasterization proceeds, every texel's neighbors will be correctly sampled. Note that beyond sampling just the nearest neighbors of a node, weighted averages of nearby nodes can be computed by exploiting the linear texture interpolation hardware available in GPUs. Care must be taken, though, since the precision used for the interpolation coefficients is sometimes lower than the rest of the texture pipeline.

**Computation on Neighbors** As I described in Section 4.3.2, many simulations compute complex functions of the neighbors they sample. In many cases, these functions can be computed ahead of time and stored in a texture for use as a lookup table. NVIDIA GeForce 3 and 4 GPUs provide a mechanism called *texture shaders* that provide a choice among many texture addressing modes for multiple texture units. ATI Radeon 8500 provides similar functionality. I have implemented table lookups using the `DEPENDENT_GB_TEXTURE_2D_NV` texture shader mode of the GeForce 3. This mode

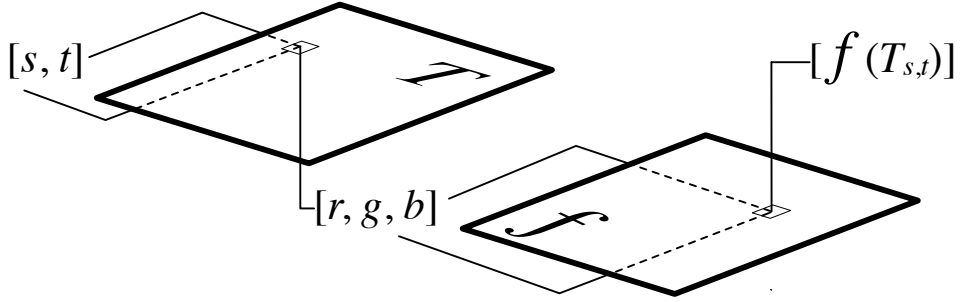


Figure 4.11: An arbitrary function can be implemented in graphics hardware by performing a table lookup using dependent texturing.

provides memory indirect texture addressing—the green and blue colors read from one texture unit are used as texture coordinates for a lookup into a second texture unit. By binding a precomputed lookup table texture to the second texture unit, arbitrary functions can be computed using the state of the nodes as input (See Figure 4.11).

**New State Computation** Once the values of neighboring texels have been sampled and optionally used for function table lookups, the next step is to compute the new state of the lattice. I use programmable hardware texture blending to perform arithmetic operations including addition, multiplication, and dot products. On the GeForce 3 and 4, I implement this using register combiners (NVIDIA Corporation, 2002b). *Register combiners* take the RGBA output of texture shaders and rasterization as input, and provide arithmetic operations, user-defined constants, and temporary registers. The result of these computations is written to the frame buffer.

### 4.3.5 Numerical Range of CML Simulations

The physically-based nature of CML simulations means that the ranges of state values for different simulations can vary widely. DX8-class graphics hardware, on the other hand, operates only on fixed point fragment values in the range  $[-1, 1]$  (and even  $[0, 1]$  at some points). This means that we must normalize the range of a simulation into  $[-1, 1]$  before it can be implemented in graphics hardware.

Because the hardware uses limited-precision fixed point numbers, some simulations will be more robust to this normalization than others. The robustness of a simulation depends on several factors. *Dynamic range* is the ratio between a simulation’s largest absolute value and its smallest non-zero absolute value. If a simulation has a high dynamic range, it may not be robust to normalization unless the precision of computation

is high enough to represent the dynamic range. I refer to a simulation’s *resolution* as the smallest absolute numerical difference that it must be able to discern. A simulation with a required resolution finer than the resolution of the numbers used in its computation will not be robust. Finally, as the arithmetic complexity of a simulation increases, it will incur more roundoff error, which may reduce its robustness when using low-precision arithmetic.

For example, the boiling simulation (Section 4.3.1) has a range of approximately  $[0, 10]$ , but its values do not get very close to zero, so its dynamic range is less than ten. Also, its resolution is fairly coarse, since the event to which it is most sensitive—phase change—is near the top of its range. For these reasons, boiling is fairly robust under normalization. Reaction-diffusion has a range of  $[0, 1]$  so it does not require normalization. Its dynamic range, however, is on the order of  $10^5$ , which is much higher than that of the 8-bit numbers stored in textures. Fortunately, by scaling the coefficients of reaction-diffusion, we can reduce this dynamic range somewhat to get interesting results. However, as we describe in Section 4.3.6, it suffers from precision errors (See Section 4.3.7 for more discussion of precision issues). With the floating point hardware available in the latest GPUs, simulations can be run within their natural ranges.

### 4.3.6 Results

I designed and built an interactive framework, “CMLlab”, for constructing and experimenting with CML simulations (Figure 4.12). The user constructs a simulation from a set of general purpose operations, such as diffusion and advection, or special purpose operations designed for specific simulations, such as the buoyancy operations described in Section 4.3.2. Each operation processes a set of input textures and produces a single output texture. The user connects the outputs and inputs of the selected operations into a directed acyclic graph. An iteration of the simulation consists of traversing the graph in depth-first fashion so that each operation is performed in order. The state textures resulting from an iteration are used as input state for the next iteration, and for displaying the simulated system. The results of intermediate passes in a simulation iteration can be displayed to the user in place of the result textures. This is useful for visually debugging the operation of a new simulation.

While 2D simulations in our framework use only 2D textures for storage of lattice state, 3D simulations can be implemented in two ways. The obvious way is to use 3D

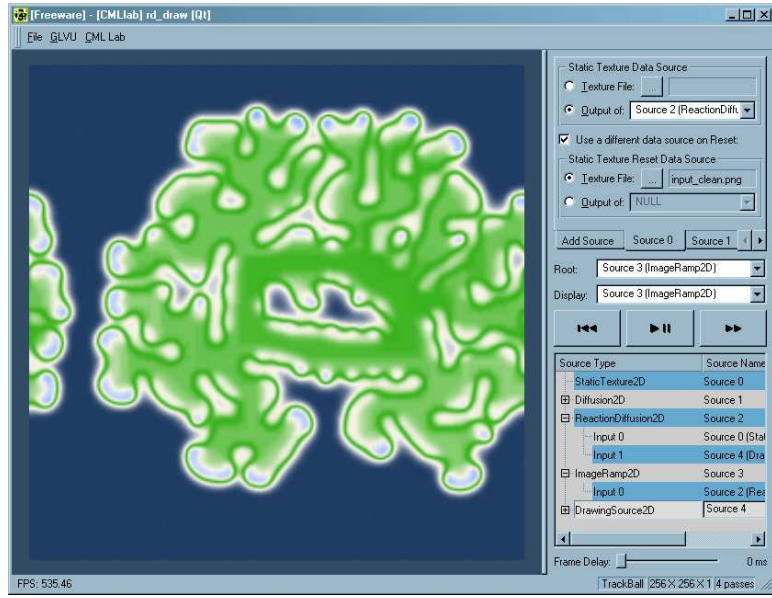


Figure 4.12: CMLlab, my interactive framework for building and experimenting with CML simulations. CMLlab provides the ability to connect various CML operations to generate unique simulations. This image shows a 2D reaction-diffusion simulation running in the CMLlab application window.

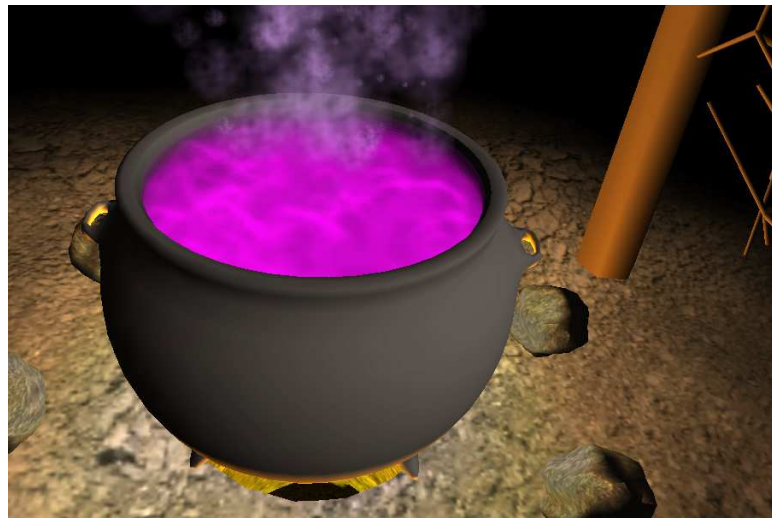


Figure 4.13: A 3D CML boiling simulation running in an interactive environment (the steam is a particle system).

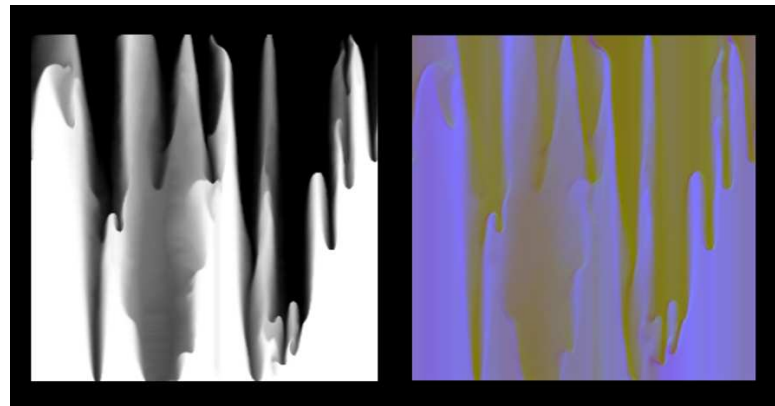


Figure 4.14: A 2D CML simulation of Rayleigh-Bénard convection. The left panel shows temperature; the right panel shows 2D velocity encoded in the blue and green color channels.

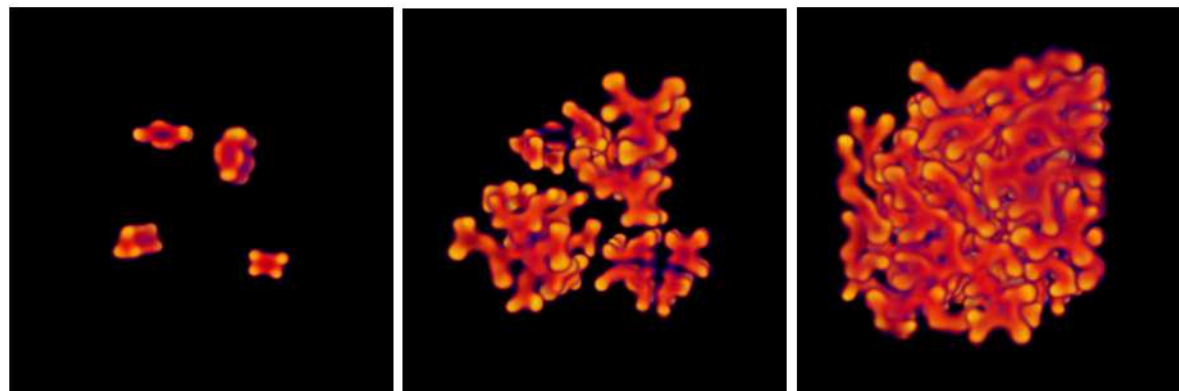


Figure 4.15: A sequence from a 3D version of the Gray-Scott reaction-diffusion model.

textures. However, the extra overhead of copying from the frame buffer to each slice of a 3D texture can make simulations run much slower. Instead, we implemented 3D simulations using a collection of 2D textures that represent slabs of the 3D volume. While this is faster than updating a 3D texture, it has disadvantages. For example, we cannot take advantage of the built in trilinear filtering and texture boundaries (clamp or repeat) that are provided in hardware for 3D textures. In the next chapter, I describe a method of using a single 2D texture to represent a 3D grid.

It is worth noting that we trade optimal performance for flexibility in the CMLLab framework. Because we want to allow a variety of models to be built from a set of operations, we often incur the expense of some extra texture copies in order to keep operations separate. Thus, our implementation is not optimal - even faster rates are achievable on the same hardware by sacrificing operator reuse.

To demonstrate the utility of hardware CML simulation in interactive 3D graphics applications, we integrated the simulation system into a virtual environment built on a 3D game engine, “Wild Magic” (Eberly, 2001). Figure 4.13 is an image of a boiling witch’s brew captured from a real-time demo we built with the engine. The demo uses our 3D boiling simulation (Section 4.3.6) and runs at 45 frames per second on an NVIDIA GeForce 4.

In the following sections I describe three of the CML simulations that we implemented. The test computer I used was a PC with a single 2.0 GHz Pentium 4 processor and 512 MB of RAM. Tests were performed on this machine with both an NVIDIA GeForce 3 Ti 500 GPU with 64 MB of RAM, and an NVIDIA GeForce 4 Ti 4600 GPU with 128 MB of RAM.

## Boiling

I implemented 2D and 3D boiling simulations as described in (Yanagita, 1992). Rather than simulate all components of the boiling phenomenon (temperature, pressure, velocity, phase of matter, surface tension, etc.), their model simulates only the temperature of the liquid as it boils. The simulation is composed of successive application of thermal diffusion, bubble formation and buoyancy, and latent heat transfer operations. The first two of these are described in Section 4.3.2, and Section 4.3.1 gives an overview of the model. For details of the latent heat transfer computation, I refer the reader to (Yanagita, 1992). Our implementation requires seven passes per iteration for the 2D simulation, and 9 passes per slice for the 3D simulation. Table 4.3.6 shows the simulation speed for a range of resolutions. For details of my boiling simulation imple-

Resolution	Iterations Per Second			Speedup	
	Software	GeForce 3	GeForce 4	GeForce 3	GeForce 4
$64 \times 64$	266.5	1252.9	1752.5	4.7	6.6
$128 \times 128$	61.8	679.0	926.6	11.0	15.0
$256 \times 256$	13.9	221.3	286.6	15.9	20.6
$512 \times 512$	3.3	61.2	82.3	18.5	24.9
$1024 \times 1024$	0.9	15.5	21.6	17.2	24
$32 \times 32 \times 32$	25.5	104.3	145.8	4.1	5.7
$64 \times 64 \times 64$	3.2	37.2	61.8	11.6	19.3
$128 \times 128 \times 128$	0.4	NA	8.3	NA	20.8

Table 4.2: A speed comparison of a hardware CML boiling simulation to a software version. “NA” means that the simulation was not performed on GeForce 3 due to memory size limitations.

mentation, see (Harris, 2002b).

## Convection

The Rayleigh-Bénard convection CML model of (Yanagita and Kaneko, 1993) simulates convection using four CML operations: buoyancy (Section 4.3.2), thermal diffusion (Section 4.3.2, temperature and velocity advection, and viscosity and pressure effect. The viscosity and pressure effect is implemented as<sup>8</sup>

$$\vec{u}' = \vec{u} + \frac{k_v}{4} \nabla^2 \vec{u} + k_p \nabla(\nabla \cdot \vec{u}),$$

where  $\vec{u}$  is the velocity,  $k_v$  is the viscosity and  $k_p$  is the coefficient of the “pressure effect” (Yanagita and Kaneko, 1993). The first two terms of this equation account for viscous diffusion of the velocity, and the last term is the flow caused by the gradient of the mass flow around the lattice (Miyazaki et al., 2001). This operation is an ad hoc simplification of the viscous diffusion and projection operations used in fluid simulation (See Section 4.2). Details of the discrete implementation of this operation are available in (Yanagita and Kaneko, 1993; Miyazaki et al., 2001).

The remaining operation is advection of temperature and velocity by the velocity field. Yanagita and Kaneko implement this using an explicit method that distributes state from a node to its neighbors according to the velocity at the node. As I noted in Section 4.2.3, this is not possible on current graphics hardware because the fragment

---

<sup>8</sup>Clearly the last term in this equation should be  $\nabla \cdot \nabla \vec{u}$ , but (Yanagita and Kaneko, 1993) chose this formulation. Their reasoning is unclear.

processors cannot perform random access writes. Instead, I used an implicit method like the one described previously. In order to implement this technique on DX8-class hardware, I used a texture shader-based advection operation. This operation advects state stored in a texture using the `GL_OFFSET_TEXTURE_2D_NV` dependent texture addressing mode of the GeForce 3 and 4. A description of this method of advection can be found in (Weiskopf et al., 2001). My 2D convection implementation (Figure 4.14) requires 10 passes per iteration. I did not implemented a 3D convection simulation because GeForce 3 and 4 do not have a 3D equivalent of the offset texture operation.

Due to the precision limitations of the graphics hardware, my implementation of convection did not behave exactly as described in (Yanagita and Kaneko, 1993). I do observe the formation of convective rolls, but the motion the flow is quite turbulent. I believe that this is a result of low-precision arithmetic.

## Reaction-Diffusion

Reaction-diffusion processes were proposed in (Turing, 1952) and introduced to computer graphics by (Turk, 1991; Witkin and Kass, 1991). They are a well-studied model for the interaction of chemical reactants, and are interesting due to their complex and often chaotic behavior. The patterns that emerge are reminiscent of patterns occurring in nature (Lee et al., 1993). Using our CMLlab environment, Greg Coombe implemented the Gray-Scott reaction-diffusion model (Pearson, 1993). This is a two-chemical system defined by the following initial value partial differential equations.

$$\frac{\partial U}{\partial t} = D_u \nabla^2 U - UV^2 + F(1 - U)$$

$$\frac{\partial V}{\partial t} = D_v \nabla^2 V + UV^2 - (F + k)V$$

Here  $F$ ,  $k$ ,  $D_u$ , and  $D_v$  are parameters given in (Pearson, 1993). Greg implemented 2D and 3D versions of this process, as shown in Figure 4.12 (2D), and Figures 4.8 and 4.15 (3D). Reaction-diffusion was relatively simple to implement in our framework because we were able to reuse the existing diffusion operator. In 2D this simulation requires two passes per iteration, and in 3D it requires three passes per slice. A 256x256 lattice runs at 400 iterations per second in our interactive framework, and a 128x128x32 lattice runs at 60 iterations per second.

The low precision of DX8 GPUs reduces the variety of patterns that the Gray-Scott model produces. We have seen a variety of results, but much less diversity than

produced by a floating point implementation. As with convection, this is caused by the effects of low-precision arithmetic.

### 4.3.7 Discussion of Precision Limitations

The low-precision of the fragment processors on DX8 GPUs limits their usefulness for physically-based simulation. The register combiners in the GeForce 3 and 4 perform arithmetic using nine-bit signed fixed point values. Without floating point, the programmer must scale and bias values to maintain them in ranges that maximize precision. This is not only difficult, it is also subject to arithmetic error. Some simulations (such as boiling) handle this error well, and behave as predicted by a floating point implementation. Others, such as reaction-diffusion, are more sensitive to precision errors.

I analyzed the error introduced by low precision and did some experiments to determine how much precision is needed for the reaction-diffusion implementation (For full details, see (Harris, 2002a)). I hypothesize that the diffusion operation is very susceptible to roundoff error, because in my experiments in CMLlab, iterated application of a diffusion operator never fully diffuses its input. I derived the error  $\epsilon_d$  induced by each application of diffusion (in 2D) to a node  $(i, j)$  as

$$\epsilon_d \approx \epsilon \left( 3 + \frac{3d}{4} + x_{i,j} \right)$$

where  $d$  is the diffusion coefficient,  $x_{i,j}$  is the value at node  $(i, j)$ , and  $\epsilon$  is the amount of roundoff error in each arithmetic operation. Since  $d$  and  $x_{i,j}$  are in the range  $[0, 1]$ , this error has an upper bound of  $|\epsilon_d| \leq 4.75\epsilon$ . With 8 bits of precision,  $\epsilon$  is at most  $2^{-9}$ . This error is fairly large, meaning that a simulation that is sensitive to small numbers will quickly diverge.

In an attempt to better understand the precision needs of more sensitive simulations, we implemented a software version of the reaction-diffusion simulation with adjustable fixed point precision. Through experimentation, we found that with 14 or more bits of fixed point precision, the behavior of this simulation is visually very similar to a single-precision floating point implementation. Like the floating point version, a diverse variety of patterns grow, evolve, and sometimes develop unstable formations that never cease to change. Figure 4.16 shows a variety of patterns generated with this 14-bit fixed point simulation.

Upon the release of the NVIDIA GeForce FX, I verified that a floating point GPU



Figure 4.16: The result of the 2D gray-scott reaction diffusion with varying parameters. By varying the fixed-point computation precision we determined that 14 bits of precision were sufficient to approximate the results of a 32-bit floating point simulation. With the advent of floating point GPUs, this is no longer necessary (see Section 4.3.7).

implementation of the Gray-Scott reaction diffusion model can generate the same rich variety of patterns as a software implementation. This model is implemented using a single Cg fragment program. I demonstrated the use of reaction-diffusion as a pattern generator for making frightening bump-mapped “disease” spots appear on a 3D character model, as shown in Figure 4.17 (Harris and James, 2003).

## 4.4 Summary

I began this chapter with a discussion of the trend that I call General-Purpose Computation on GPUs (GPGPU) and categorized GPUs according to the version of the DirectX API that they support. For completeness, the last part of the chapter (Section 4.3), describes simulation of coupled map lattice models and simple PDEs on lower-precision DX8-class GPUs. The most important part of this chapter is Section 4.2, in which I explain the “Stable Fluids” algorithm for fluid simulation, and a method for implementing it on the GPU. This technique is the core on which I build my GPU cloud simulation in the next chapter.

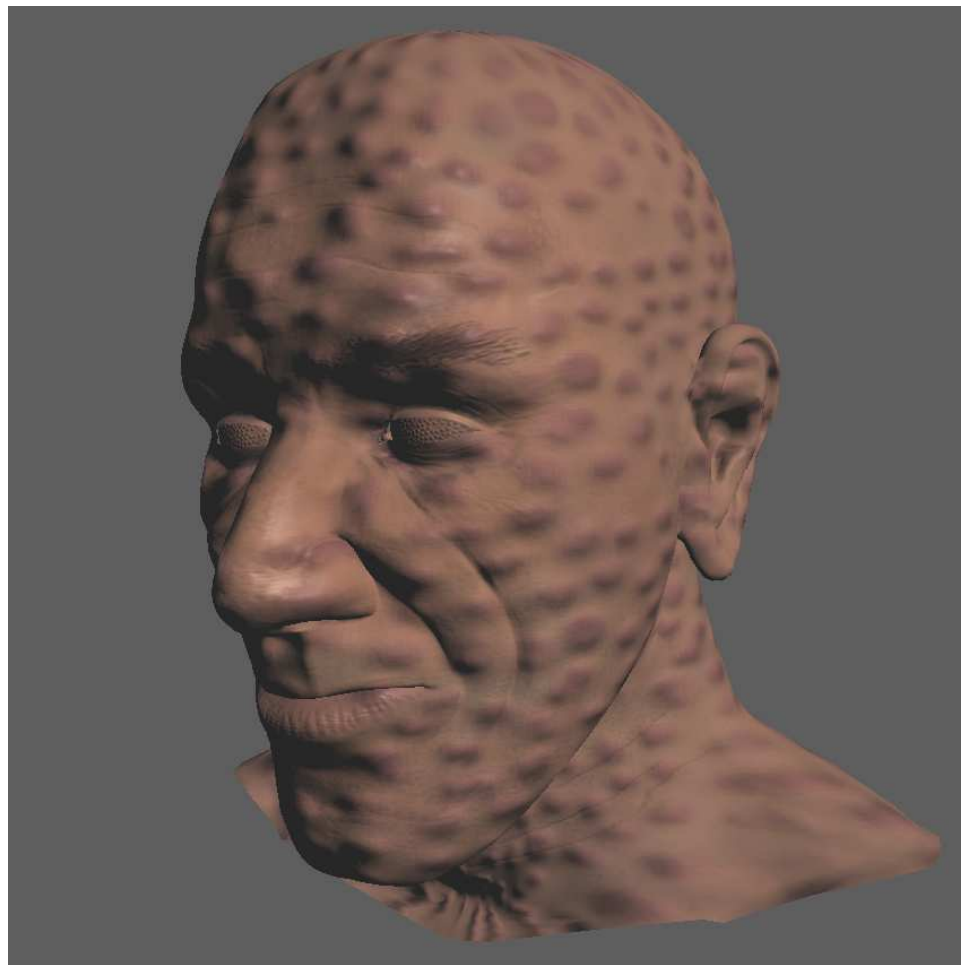


Figure 4.17: This image demonstrates a 2D Gray-Scott reaction-diffusion simulation running on an NVIDIA GeForce FX GPU. The results of the simulation are converted into bump and color maps used to create creepy moving "disease" spots.

# Chapter 5

## Simulation of Cloud Dynamics

Clouds can form in many ways. *Convective clouds* form when moist air is warmed and becomes buoyant. The air rises, carrying water vapor with it, expanding and cooling as it goes. As the temperature and pressure of the air decrease, its saturation point—the equilibrium level of evaporation and condensation—is reduced. When the water vapor content of the rising air becomes greater than its saturation point, condensation occurs, which yields the microscopic condensed cloud water particles that we see as clouds in the sky. Condensation increases the drag on the air, causing it to slow its ascent, which creates a natural limit on the vertical extent of a cloud layer. *Stratus clouds* usually form when masses of warm and cool air mix due to radiative cooling or lifting of the air over terrain (*Orographic lifting*). An example of the formation of stratus clouds by mixing is the fog that often rolls into the city of San Francisco.

I have developed a cloud dynamics simulation based on partial differential equations that model fluid flow, thermodynamics, and water condensation and evaporation, as well as various forces and other factors that influence these equations. These equations are described in detail in Chapter 2. Aided by Bill Baxter and Thorsten Scheuermann, I implemented the discrete form of these equations using programmable floating-point graphics hardware (Harris et al., 2003). All computation and rendering is performed on the GPU; the CPU provides only high-level control. In this chapter I describe the implementation of the simulation in detail, along with two useful optimizations: a representation of volume data in two-dimensional textures, and an efficient packing of scalar fields to best exploit the vector operations of the fragment processor. Figure 5.1 shows a sequence from a two-dimensional cloud simulation, and Figures 1.2 and 5.4 show 3D clouds.

In order to incorporate dynamic 3D clouds into interactive graphics applications,

the per-frame simulation cost must be small enough that it does not interfere with the application. In Section 5.5 I describe a method for amortizing the simulation cost over multiple frames, allowing the application to budget time for the simulation in each frame. This technique greatly improves interactivity, allowing a user to view the results of a simulation at 60 frames per second or higher while the simulation progresses at several iterations per second. I integrated cloud simulation with an interactive flight application (Harris and Lastra, 2001) that reduces the high cost of slice-based volume cloud rendering by using dynamically-generated impostors. I describe algorithms for efficient rendering of illuminated clouds in Chapter 6.

## 5.1 Solving the Dynamics Equations

As I described in Chapter 2, my simulation solves the Euler equations of incompressible fluid flow, (2.3) and (2.4), the water continuity equation, (2.14), and the thermodynamic equation, (2.18).

### 5.1.1 Fluid Flow

My cloud model is based on the equations of fluid flow, so my simulator is built on top of a standard fluid simulator much like the ones described by (Stam, 1999; Fedkiw et al., 2001). It solves the equations of motion using the stable two step technique described in those papers and detailed in Chapter 4. In the first step, I use the semi-Lagrangian advection technique that Stam described to compute an intermediate velocity field  $\vec{u}'$ , and add to it the buoyancy force, Equation (2.10), and vorticity confinement force, Equation (4.17). This step solves Equation (2.3) without the pressure term. In the second step, the intermediate field  $\vec{u}'$  is made incompressible (so that it satisfies both Equation (2.3) and Equation (2.4)) using the Helmholtz-Hodge decomposition (see Section 4.2.3).

Using the advection technique as for velocity, I also advect the potential temperature,  $\theta$ , and water variables,  $q_v$  and  $q_c$ . During advection, I apply different boundary conditions for each of the variables. For the velocity, I use the no-slip condition ( $\vec{u} = 0$ ) on the bottom boundary, and free-slip condition ( $\partial \vec{u} / \partial \hat{n} = 0$ ) on the top. At the sides, I set the horizontal velocities to the user-defined horizontal wind speeds. I set the top and side temperature boundaries to the user-defined ambient temperature. I use periodic side boundaries for  $q_v$  to simulate water vapor being blown in from outside

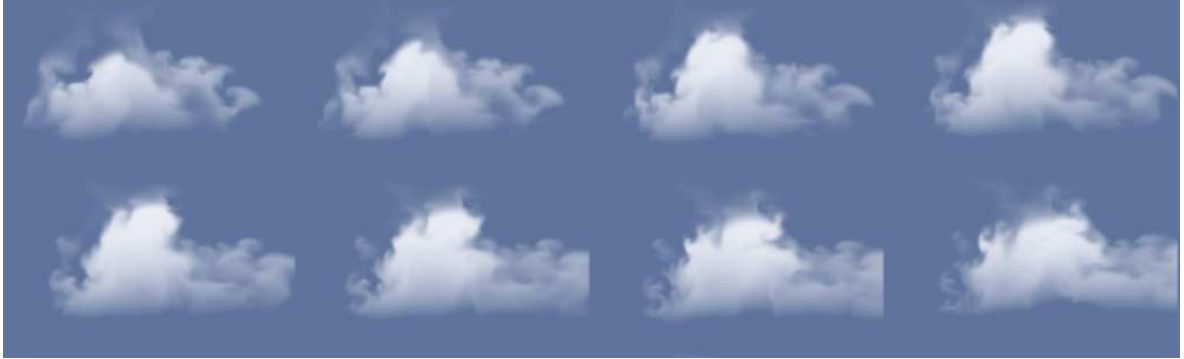


Figure 5.1: A sequence of stills (left-to-right, top-to-bottom) from my 2D cloud simulation, running on a 128x128 grid at greater than 30 frames per second.

the simulation domain, and I set all  $q_c$  boundaries and the top  $q_v$  boundary to zero. Finally, I specify input fields at the bottom boundary for both temperature and water vapor. These fields are randomly perturbed, user-specified constant values, and are the source of the temperature and water that cause clouds to form.

### 5.1.2 Water Continuity

The solution of the water continuity equations (2.14) is straightforward. The equations state that the changes in  $q_v$  and  $q_c$  are governed by advection of the quantities as well as by the amount of condensation and evaporation. I solve them in two steps. First, I advect each using the semi-Lagrangian technique mentioned before, resulting in intermediate values  $q'_v$  and  $q'_c$ . Then, at each cell, I compute the new mixing ratios as follows:

$$\begin{aligned}\Delta q'_v &= -\Delta C = \min(q_{vs} - q'_v, q'_c), \\ q_v &= q'_v + \Delta q'_v, \\ q_c &= q'_c - \Delta q'_v,\end{aligned}\tag{5.1}$$

where  $\Delta C$  is the amount of condensation over the time step, and  $q_{vs}$  is computed using equation (2.13) as described in Section 2.1.7. I compute  $T$  using equation (2.9) with the current potential temperature  $\theta$ , and the local environmental pressure computed with equation (2.11).

### 5.1.3 Thermodynamics

The left-hand side of the thermodynamic equation, (2.18), shows that like the other quantities, potential temperature is advected by the velocity field, so I compute an

intermediate value,  $\theta'$  via the semi-Lagrangian advection scheme. As mentioned in Section 2.1.8, I substitute  $-C$  for the quantity in parentheses on the right-hand side of the thermodynamic equation. This means that the temperature increases by an amount proportional to the amount of condensation, and I update it as follows:

$$\theta = \theta' + \frac{L}{c_p \Pi} \Delta C. \quad (5.2)$$

## 5.2 Implementation

I solve the cloud dynamics equations on a grid of voxels. I use a staggered grid discretization of the velocity and pressure equations as in (Foster and Metaxas, 1997; Griebel et al., 1998; Fedkiw et al., 2001). This means that pressure, temperature, and water content are defined at the center of voxels while velocity is defined on the faces of the voxels. Not only does this method reduce numerical dissipation as mentioned by Fedkiw et al., but as Griebel et al. explain, it prevents possible pressure oscillations that can arise with collocated grids (in which all variables are defined at cell centers). My experiments with collocated grids have indeed shown some undesirable pressure oscillations when buoyant forces are applied. Section 5.4 describes my implementation of voxel grids using textures.

Overall, my algorithm for solving the equations of cloud dynamics at each discrete time step is as follows.

1. Advect  $\theta$ ,  $q_v$ ,  $q_c$  and velocity,  $\vec{u}$ .
2. Compute vorticity confinement force,  $\vec{f}_{vc}$ .
3. Compute buoyant force,  $B\hat{k}$ .
4. Compute  $\vec{u}' = \vec{u}_{adverted} + (B\hat{k} + \vec{f}_{vc})\delta t$ .
5. Update  $q_v$  and  $q_c$  according to Equation (5.1).
6. Update  $\theta$  according to Equation (5.2).
7. Compute the divergence  $\nabla \cdot \vec{u}'$ .
8. Solve the Poisson-pressure equation, (4.6).
9. Compute  $\vec{u} = \vec{u}' - \nabla p$ .

My implementation of steps 1, 2, 7, and 9 follows (Fedkiw et al., 2001) nearly exactly. I refer the reader to the appendix of that paper for the discrete form of the equations. Step 3 can be implemented directly from equation (2.10). However, I find that providing the user with a scale factor applied to  $q_H$  provides useful control over

the buoyancy of clouds. In my implementation, steps 5 and 6 are performed in a single fragment program, because I store the water and temperature variables in a single texture. For the same reason, I advect the potential temperature and water variables simultaneously. I solve the remaining step, the Poisson-pressure equation, using a standard iterative relaxation solver applied to equation (4.6).

Fedkiw, et al. use the conjugate gradient method with an incomplete Choleski preconditioner to solve the Poisson-pressure equation (Fedkiw et al., 2001). While this is a straightforward solver to implement and run on a CPU, my implementation uses fragment programs that run on the GPU. Implementation of conjugate gradient on the GPU is feasible (Bolz et al., 2003; Krüger and Westermann, 2003), but many passes are required just to compute the large vector inner products required by the algorithm ( $O(\log_2 N)$  passes, where  $N$  is the grid resolution). For this reason, I chose to use a simple solver such as Jacobi or Red-Black Gauss Seidel relaxation (Golub and Van Loan, 1996). These solvers can be implemented to run in one and two render passes, respectively, using only a few lines of *Cg* code. Therefore I can run more iterations in a given amount of time than with a more complex method, which helps make up for the slower convergence of the chosen solver. Section 5.4.1 discusses the efficient implementation of these solvers.

I typically use a grid scale ( $\delta x$ ) of 50–100 m. I choose an altitude range, and then set the grid scale so that the grid covers that range. For example, if I want to represent a 3.2 km altitude range<sup>1</sup>, then I set  $\delta x$  to 100 m on a  $32 \times 32 \times 32$  grid, or 50 m on a  $64 \times 64 \times 64$  grid.

### 5.3 Hardware Implementation

As I mentioned before, the cloud simulator performs all numerical computation in the programmable, floating point fragment unit of a graphics processor. State fields, such as  $p$  and  $\vec{u}$ , are stored in textures. For efficiency, I store  $\theta$ ,  $q_v$ , and  $q_c$  in different channels of the same texture. Computation is performed as described in Chapter 4. State textures are updated using a render pass that draws a quadrilateral fit to the viewport. I implement computations using fragment programs written in the *Cg* shading language (Mark et al., ). The fragment programs implement the steps described in Section 5.2 using texturing operations to read data from the grids. At the end of a render pass, the state texture is updated as described in Section 4.2.4.

---

<sup>1</sup>The base of cumulus clouds is typically 1–2 km in fair, humid weather (Rogers and Yau, 1989).

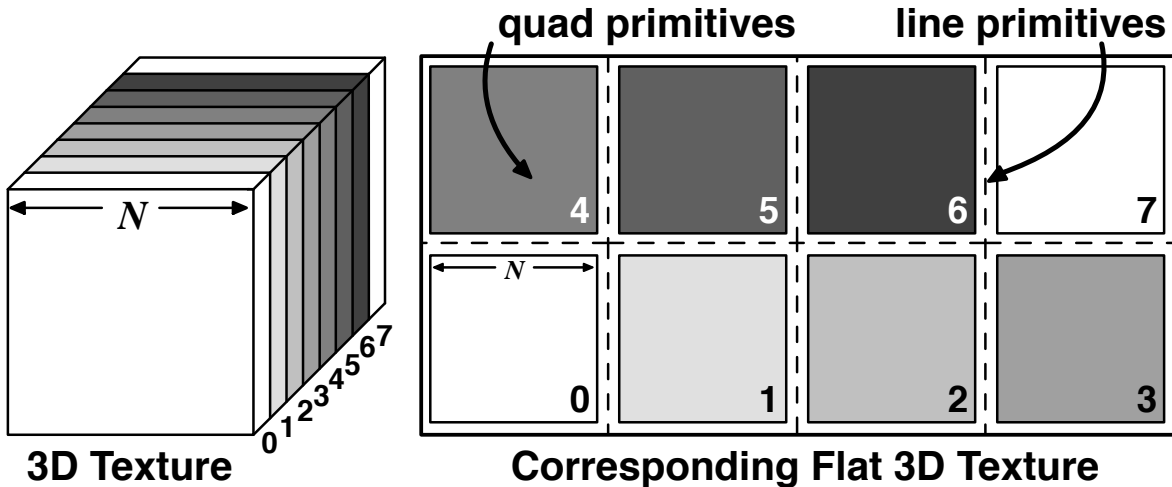


Figure 5.2: A Flat 3D Texture is a 2D texture made up of the tiled slices of a 3D texture. Flat 3D Textures allow all slices of the volume to be updated in a single rendering pass.

## 5.4 Flat 3D Textures

Section 4.3.6 describes how I used stacks of 2D textures to represent 3D volumes on DX8 GPUs, because of the expense of updating a 3D texture. To apply a simulation operation to the grid—for example to compute the buoyancy force—the volume must be updated slice by slice. At each slice, the operation is applied, and the texture for that slice is updated, requiring a texture copy or a context switch associated with render to texture.

On DX9 GPUs, it is possible to avoid the overhead of a texture update per volume slice. For cloud simulation, I represent grids using what I call a “flat” 3D texture. A flat 3D texture is a 2D texture that contains the tiled slices of a 3D volume, as shown in Figure 5.2. In the figure, the white borders represent the boundary cells of each slice, and the white boxes in the lower left and upper right represent the boundary slices on the ends of the volume along the slicing axis. Updating a flat 3D texture is much like the 2D texture update described in the previous section. I render the interior of each slice (the gray squares) using a quad primitive, and I render the boundaries using line primitives. I use one fragment program for all of the interior quad primitives, and another for the boundary lines and the two “end cap” (lower left and upper right) quads.

The advantage of true 3D textures over flat 3D textures is that addressing them is easy, since the GPU supports it. With flat 3D textures, however, the  $r$  (depth) texture

coordinate must be converted into a 2D offset in each fragment program in order to do a texture lookup. In practice, I precompute a 1D lookup texture that contains the offsets for each slice, and use this as an indirection table indexed by the  $r$  coordinate.

Flat 3D textures can be updated in a single render pass—only one texture update is required for the entire volume. This means that a 3D simulation can be implemented in the same number of passes as an equivalent 2D simulation (ignoring changes in the computation itself). Flat 3D textures provide a performance advantage over true 3D textures on current hardware. While the amount of data copied or updated is the same, in my experience, the total slice update overhead is much greater for true 3D textures. Also, because more fragments are processed in a single pass, flat 3D textures make better use of the parallelism of the fragment processor. Finally, flat 3D textures provide a quick, inexpensive way to preview the results of a 3D simulation, since they can be easily rendered as a 2D image.

### 5.4.1 Vectorized Iterative Solvers

Iterative solution of the Poisson equation for pressure is one of the most expensive operations in numerical fluid and cloud simulation. For simulation on the GPU, the choice of solver is limited by the inability of fragment programs to both read and write the same memory in the same pass. This rules out Gauss-Seidel and Successive Over-relaxation (SOR), which have been used in many previous graphics applications of fluid simulation. Bill Baxter and I have, however, implemented several solvers and conducted an investigation to determine the most efficient of these given the constraints of graphics hardware. The results are given in Table 5.1.

Our Jacobi solver stores pressure as a single-channel floating point texture. The Jacobi fragment program also takes a divergence texture as input, and computes an updated pressure value as output for each fragment by sampling neighboring pressure values and subtracting the input divergence. After this single pass the output texture is used as input for the next iteration of the solver.

Red-Black Gauss-Seidel is a variation on Jacobi that splits the cells into two sets such that new Red cell values only depend on Black cell inputs, and vice versa (see Figure 5.3). All the Red values can be updated using only the old Black values, and then the Black values can be updated using the new Red values. Using the most recently-updated half of the cells for updates improves the convergence rate.

To implement Red-Black efficiently we pack four pressure values into a single RGBA

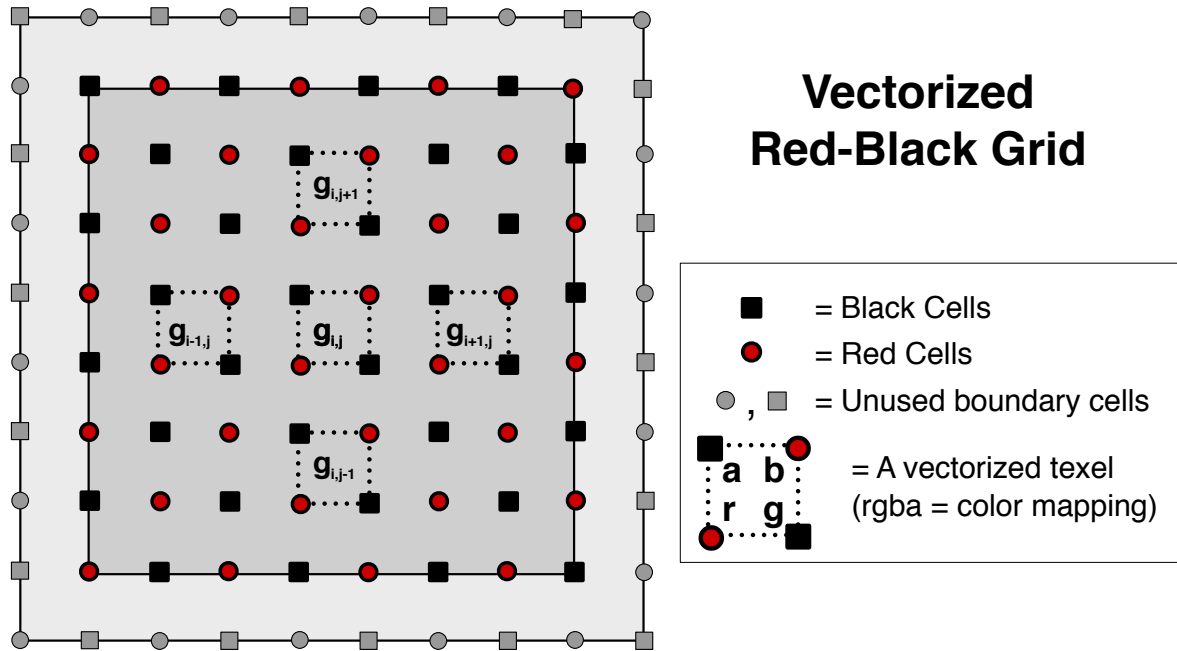


Figure 5.3: Efficient iterative Poisson solvers can be implemented by packing multiple scalar values into each texel. The cross pattern demonstrates the sampling pattern for vectorized Jacobi and Red-Black iteration.



Figure 5.4: Simulated clouds in the SkyWorks interactive flight application.

Poisson Solver	Convergence per ms <sup>a</sup>	Convergence <sup>b</sup>	Time <sup>c</sup> (ms)
Jacobi 2D	0.50	0.078	45.9
Red-Black 2D	0.85	0.124	45.3
Vectorized Jacobi 2D	1.0	0.079	17.3
Jacobi 3D	NC	NC	110 <sup>d</sup>
Vectorized Jacobi 3D	NC	NC	49.0

<sup>a</sup> Normalized convergence per millisecond achieved with a 17 ms time budget.

<sup>b</sup> Relative convergence after 100 iterations.

<sup>c</sup> Time for execution of 100 iterations.

<sup>d</sup> Estimated from register usage, program length, and fragment count for 3D Jacobi program.

Table 5.1: A comparison of the convergence rates of various iterative solvers running on the GPU. All grids were  $128 \times 128$  or  $32 \times 32 \times 16$ . (NC  $\equiv$  “Not Computed”.)

texel, as shown in Figure 5.3. This allows us to reduce the overall number of texture lookups required for each half-pass of Red-Black. Without packing, the Red pass would require 5 texture lookups per pressure update (corresponding to the 5 cells of a 5-point discrete Laplacian) in 2D, and 7 lookups in 3D. By packing pressure in a vectorized format the same 5 or 7 texture lookups enable us to update 4 pressure values instead of just one, as can be seen in Figure 5.3. With the 5 samples shown, the 4 pressure values in  $g_{i,j}$  can be updated. This is a significant savings; however, we incur extra overhead since the Black cells must be explicitly passed through on a Red pass and vice versa, so that both Red and Black are written every pass, and we also incur the overhead of two rendering passes for one solver iteration. Still, Red-Black converges faster than a basic Jacobi solver given a fixed time budget.

The same vectorization technique used to accelerate the Red-Black solver can also be used to accelerate the Jacobi solver. With vectorization, two full Jacobi iterations take less time than a full Red-Black iteration, and give better convergence. The result is that vectorized Jacobi gives the best convergence under a fixed time budget of any of the hardware solvers we tested (See Table 5.1).

## 5.5 Interactive Applications

Cloud simulation is a computationally intensive process that is usually done offline. But simulations of phenomena such as clouds have the potential to provide rich dynamic content for interactive applications, so one of my goals has been to create a simulation that will work well online.

As a test of this, I integrated cloud simulation into my cloud rendering engine, *SkyWorks* (Harris and Lastra, 2001). *SkyWorks* was designed to render scenes full of static clouds very fast. As I describe in Chapter 6, it precomputes the illumination of the clouds, and then uses this illumination to render the clouds at run time. To reduce the cost of rendering the clouds, it uses dynamically generated impostors (Schaufler, 1995).

### 5.5.1 Simulation Amortization

Real-time visualization of simulated 3D clouds requires that the per-frame simulation cost be small enough that it does not interfere with the application. If I were to perform a complete simulation time step every frame, the application’s frame rate would drop below the frame rate of the cloud simulation. As an example, a simulation on a grid of resolution  $64^3$  updates at under four iterations per second. This is not an acceptable frame rate for a flight simulator.

To avoid this problem, we (Bill Baxter and I) built into the simulation system a method for automatically dividing the work of a simulation time step over multiple frames. This is fairly straightforward to do with a GPU simulation because each operation is a render pass. We instrumented our simulator with the ability to measure the time taken by any render pass. Every so often (usually just at startup and at the user’s request) we run a complete simulation step with these timers active, and we record the time for each step. Then, in each frame of the application, the application budgets a certain amount of time for the simulation, and the simulator attempts to stay as close to that budget as possible by executing just as many passes as will fit in the time budget.

This technique makes a tremendous difference in the performance of application. In *SkyWorks*, the user can fly around and through dynamic clouds at 40-80 frames per second while the simulation updates 1-5 times per second. Since the simulation time step can be set at a few seconds (thanks to the stable fluid simulation), clouds can update in approximately “real time”.

Resolution	Iterations Per Second			
	P4 <sup>a</sup>	Quadro FX <sup>b</sup>	GeForce FX 5800 <sup>c</sup>	GeForce FX 5900 <sup>d</sup>
16 × 16	518.67	368.32	585.48	642.67
32 × 32	239.64	364.30	583.09	620.35
64 × 64	73.38	164.37	256.34	289.18
128 × 128	16.59	49.01	74.44	89.49
256 × 256	3.84	13.03	19.22	21.35
512 × 512	0.98	3.29	4.82	5.22
1024 × 1024	0.25	0.69	1.02	1.28

<sup>a</sup> Intel Pentium 4 2.0 GHz CPU w/ 512 MB RAM.

<sup>b</sup> NVIDIA Quadro FX 1000 GPU w/ 128 MB RAM.

<sup>c</sup> NVIDIA GeForce FX 5800 Ultra GPU w/ 128 MB RAM.

<sup>d</sup> NVIDIA GeForce FX 5900 Ultra GPU w/ 256 MB RAM.

Table 5.2: Performance data for two-dimensional cloud simulation on a CPU and three different GPUs.

Still, this system is not perfect, because it is very difficult to accurately time an operation in the graphics pipeline. In order to get the best interactivity, the simulator must only rarely go over budget. To ensure this, we try to get worst case timings for each operation by forcing the pipeline to flush before stopping the timer. But this is not realistic, because under normal conditions (i.e. without forced flushes) there is more parallelism in the GPU. Therefore, a better method—perhaps with hardware support—of timing GPU operations would be useful.

## 5.6 Results

My GPU simulation system enables fast, physically-based cloud simulation on larger volumes than have been used previously in computer graphics applications. On volumes of resolution  $32 \times 32 \times 32$  and  $64 \times 64 \times 64$ , the simulator achieves update rates of approximately 27.4 and 3.9 iterations per second, respectively, on an NVIDIA GeForce FX 5900 Ultra. Tables 5.2 and 5.3 provide detailed performance data (in iterations per second) for two- and three-dimensional cloud simulation at a variety of resolutions. I ran the simulations on an Intel Pentium 4 CPU with 512MB of RAM and on three different NVIDIA GPUs: a Quadro FX 1000 with 128MB of RAM, a GeForce FX 5800

Resolution	Iterations Per Second			
	P4 <sup>a</sup>	Quadro FX <sup>b</sup>	GeForce FX 5800 <sup>c</sup>	GeForce FX 5900 <sup>d</sup>
16 × 16 × 16	49.55	34.84	82.64	69.54
32 × 32 × 32	5.13	16.02	24.44	27.43
64 × 64 × 64	0.57	2.20	3.36	3.87
128 × 128 × 32	0.24	1.01	1.47	2.08
128 × 128 × 64	0.12	0.48	0.71	1.02
128 × 128 × 128	0.07	NC <sup>e</sup>	NC <sup>e</sup>	0.37

<sup>a</sup> Intel Pentium 4 2.0 GHz CPU w/ 512 MB RAM.

<sup>b</sup> NVIDIA Quadro FX 1000 GPU w/ 128 MB RAM.

<sup>c</sup> NVIDIA GeForce FX 5800 Ultra GPU w/ 128 MB RAM.

<sup>d</sup> NVIDIA GeForce FX 5900 Ultra GPU w/ 256 MB RAM.

<sup>e</sup> Not computed due to memory size limitations.

Table 5.3: Performance data for three-dimensional cloud simulation on a CPU and three different GPUs. Two of the GPUs had only 128 MB of RAM, and therefore could run a maximum simulation size of  $128 \times 128 \times 64$ . The other GPU had 256MB of RAM, and could run a maximum simulation size of  $128 \times 128 \times 128$ .

Ultra with 128MB of RAM, and a GeForce FX 5900 Ultra with 256MB of RAM.

Figures 5.5 and 5.6 show the relative performance of the simulations on the four different processors. The figures show that in all tests, GPU simulations outperformed the CPU simulation. In the bar charts, the speedup of each simulation over the CPU simulation is printed at the end of the bar representing the speed of the simulation in iterations per second. At the lowest-resolution, the CPU slightly outperforms the slowest GPU, but the resolution is so low as to not be of practical use. The maximum speedup attained was 5.6 in 2D, and 8.7 in 3D, both on the GeForce FX 5900 Ultra.

Note that I was unable to run some of the highest-resolution 3D simulations on all GPUs. This is because of the data size of the simulations. A single  $128 \times 128 \times 128$  grid requires 32MB of storage (because each grid cell holds 4 32-bit values). My simulator requires at least 4 of these grids to store the state and temporary values, plus auxiliary rendering buffers. Therefore, the largest simulation possible on GPUs with only 128MB of RAM is  $128 \times 128 \times 64$ . The GeForce FX 5900 Ultra GPU with 256MB of RAM is able to execute a  $128 \times 128 \times 128$  simulation.

Simulation amortization has proven very valuable for visualizing the results of simulations. Combined with my efficient illumination algorithm and the use of impostors for

Advected Quantity	Average time per pass (ms)	
	Colocated Grid	Staggered Grid
Scalar 2D	0.71	0.87
Velocity 2D	0.67	2.40
Total 2D	1.39	3.28
Scalar 3D	NC	2.34
Velocity 3D	NC	8.28
Total 3D	NC	10.61
Split Velocity 3D (3 passes)	NC	5.90
Total 3D with Split Velocity	NC	8.24

Table 5.4: Cost comparison for various implementations of the advection operation. (NC  $\equiv$  “not computed”.)

rendering (see Chapter 6), this technique allows the user to move around and through clouds like the ones in Figures 1.2 and 5.4 at high frame rates (the grid resolutions in these figures are  $64 \times 32 \times 32$  and  $64 \times 32 \times 64$ , respectively).

The advection portion of the simulation is one of its bottlenecks. This is especially true in the case of staggered grid advection. Bill Baxter and I compared the performance of advection under various conditions, shown in Table 5.4. We found that in large 3D staggered grid simulations, the advection step could cause a large, regular jump in the otherwise smooth frame rate when performing amortized simulation. We solved this problem by splitting advection into three less expensive passes (one for each dimension). This increase in granularity enables a more balanced per-frame simulation cost, since the velocity computation can be spread over more than one frame.

Because velocity is stored in three separate color channels of a texture, we use the color mask functionality of OpenGL to ensure that each advection pass writes only a single color channel. This way, only one texture update is necessary for all three passes. Splitting advection has another advantage. Fragment program performance on GeForce FX decreases with the number of registers used. Therefore even though the total instruction count for the split version is slightly higher, the shorter fragment programs execute faster because they use fewer registers. Therefore the total cost of split advection is lower, as shown in Table 5.4.

## 5.7 Summary

This chapter describes my cloud simulation system. My simulation algorithm uses the GPU to solve the dynamics equations (Section 5.1). In order to improve performance on 3D simulations, I use flat 3D textures, which allow the entire volume to be updated in a single pass (Section 5.4). I improve performance on the most intensive step of the simulation—solving the Poisson-pressure equation—by using a vectorized iterative solver that packs four scalar values into each color channel of a texture in order to reduce computation (Section 5.4.1). To enable integration of my simulation with interactive applications such as flight simulators, I use a technique called simulation amortization (Section 5.5). This spreads the computation of each simulation time step over multiple frames, so that the rendering frame rate remains high and relatively consistent. The result of these components is a fast cloud dynamics simulation that produces realistic clouds in real time. In the next chapter I discuss techniques for illuminating and rendering these clouds.

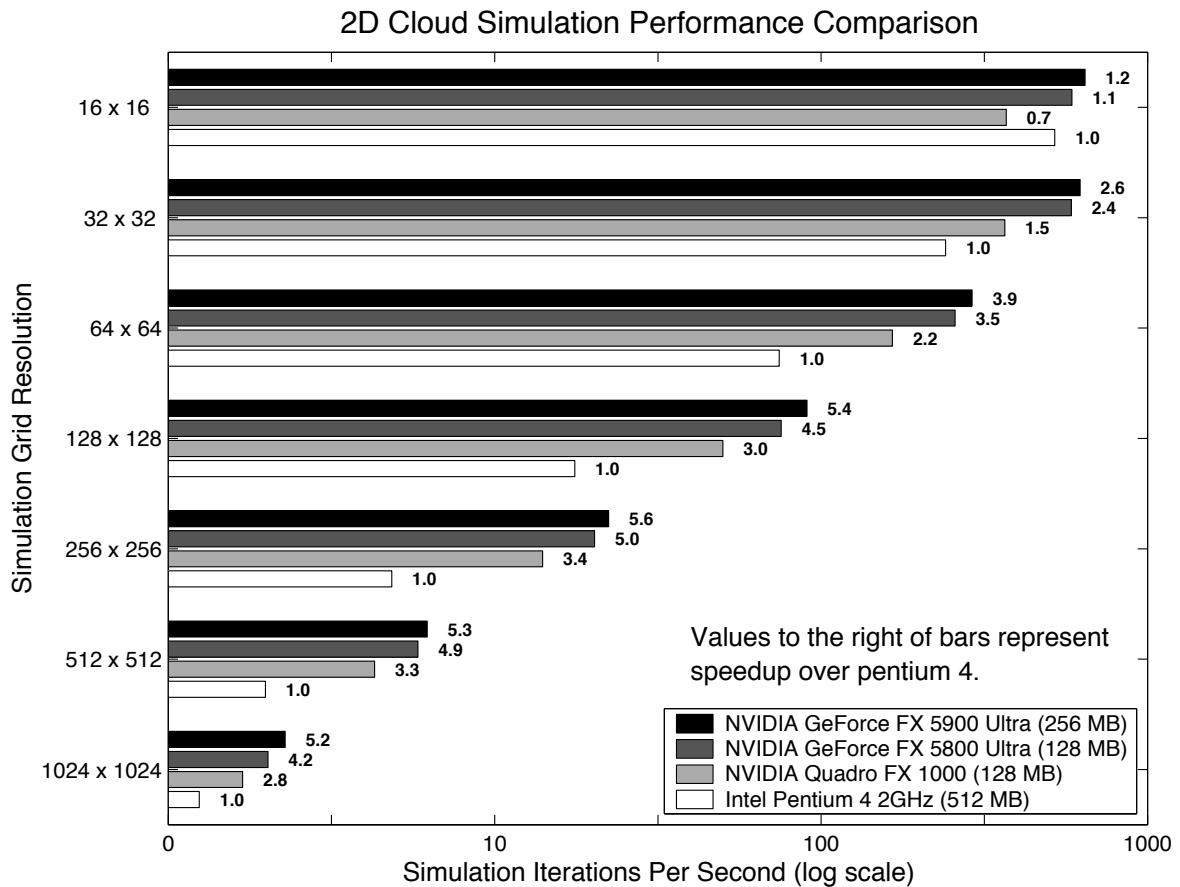


Figure 5.5: A comparison of two-dimensional cloud simulation performance on various GPUs and a CPU. The lengths of the bars represent the execution speed, in iterations per second, of the simulation running on each processor at a variety of resolutions. For comparison, the speedup each processor achieves over a 2 GHz Pentium 4 CPU is printed at the end of each bar. In these tests, the Jacobi solver was run for 40 iterations at each time step.

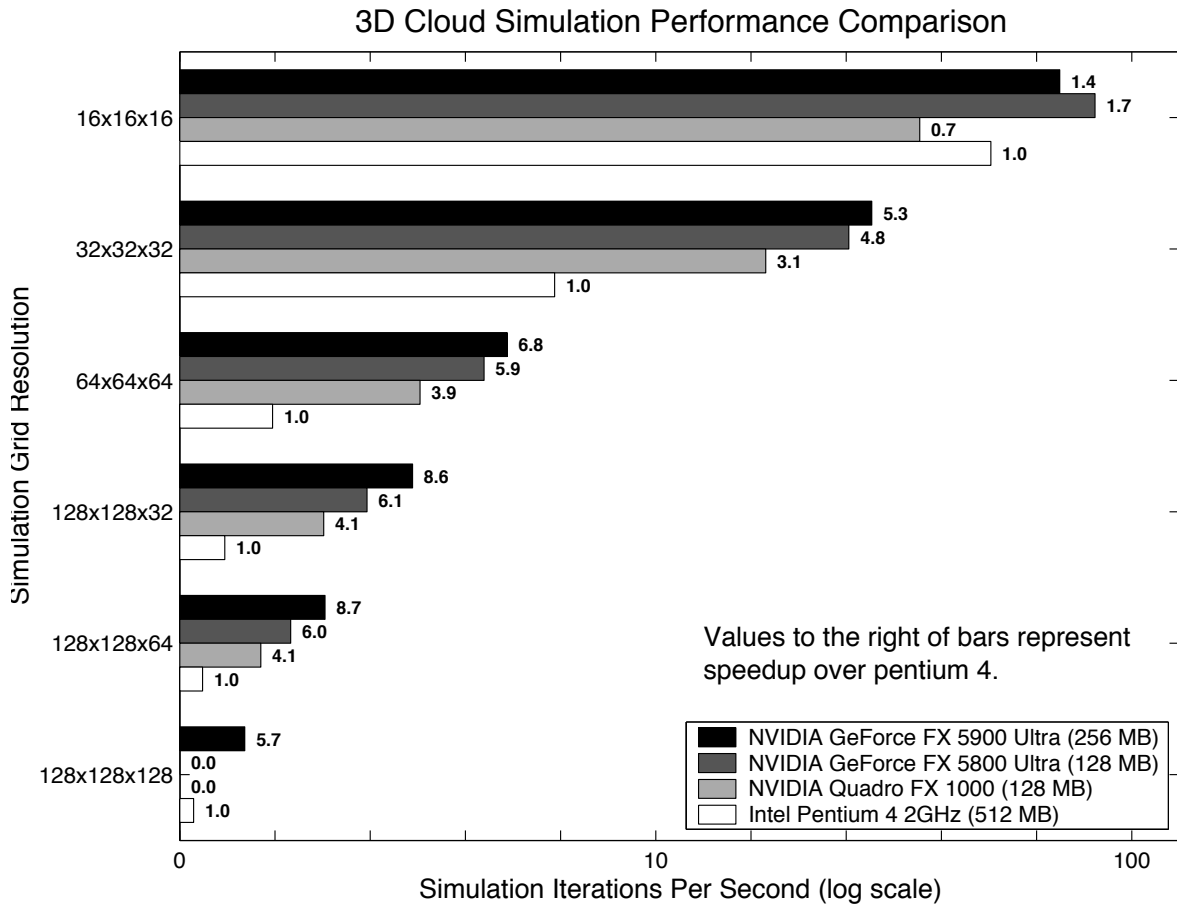


Figure 5.6: A comparison of three-dimensional cloud simulation performance on various GPUs and a CPU. The lengths of the bars represent the execution speed, in iterations per second, of the simulation running on each processor at a variety of resolutions. For comparison, the speedup each processor achieves over a 2 GHz Pentium 4 CPU is printed at the end of each bar. The highest resolution simulation was not run on the GPUs with only 128 MB of RAM because the simulation data would not fit in memory. In these tests, the Jacobi solver was run for 40 iterations at each time step.

# Chapter 6

## Cloud Illumination and Rendering

Chapters 2 through 5 provide detailed information about simulating cloud dynamics using graphics hardware. In order to create beautiful and realistic images from these simulations, I must simulate another aspect of cloud physics—cloud radiometry. Volumetric clouds are expensive to render, and generating images fast enough for interactive applications is difficult. In this chapter I describe algorithms for simulating cloud radiometry and a method for accelerating cloud rendering using dynamically generated impostors.

### 6.1 Cloud Illumination Algorithms

In Section 2.2, I defined the essential radiometry terms necessary to simulate the interaction of light with clouds. From these basics, in this section I derive simplified equations and present algorithms for computing the illumination of clouds. In the previous two chapters, I described techniques for simulating the dynamics of clouds. The result of the simulation is a voxel grid of cloud water concentrations. In contrast, my initial work on cloud rendering dealt with static clouds represented using a collection of particles (Harris and Lastra, 2001). Therefore, I begin with a derivation of a generic illumination algorithm that can be modified to compute the illumination of both cloud representations.

Particle systems simply and efficiently represent clouds. Particles in my static cloud model represent a roughly spherical volume in which a Gaussian distribution governs the density falloff from the center of the particle. Each particle in the cloud is described using its center, radius, density, and color. By filling space with particles of varying size and density I have achieved good approximations of real clouds. Clouds in my

system are built with an editing application that allows a user to place large spheres to define the large-scale shape of the cloud. The application then randomly fills this cloud volume with particles of various size and density according to configurable parameters. I render cloud particles using splatting (Westover, 1990), by drawing screen-oriented quadrilaterals texture-mapped with a Gaussian density texture.

The dynamic clouds that I described in Chapter 5 are represented in voxel volumes. Rendering voxel datasets is quite different from particle rendering. While several methods for rendering them exist (Levoy, 1988; Lacroix and Levoy, 1994; Cabral et al., 1994), the slice-based rendering method of (Wilson et al., 1994) is popular because many current GPUs support fast rendering from 3D volume textures. Section 6.1.6 discusses sliced volume rendering.

### 6.1.1 Light Scattering Illumination

Scattering illumination models simulate the emission and absorption of light by a medium as well as scattering through the medium. Section 2.2.3 defines single and multiple scattering. Single scattering models simulate scattering through the medium in a single direction. In computer graphics, this is usually the view direction, because the light scattered to the viewpoint creates the image of the cloud. Multiple scattering models are more physically accurate, but must account for scattering in all directions (or a sampling of all directions), and therefore are much more complicated and expensive to evaluate. The cloud rendering algorithm presented by Dobashi et al. approximates cloud illumination with single scattering (Dobashi et al., 2000). This approximation has been used previously to render clouds and other participating media (Blinn, 1982b; Kajiya and Von Herzen, 1984; Klassen, 1987; Max, 1995).

In a multiple scattering simulation that samples  $N$  directions on the sphere, each additional order of scattering that is simulated multiplies the number of simulated paths by  $N$ . Fortunately, as demonstrated by Nishita et al., the contribution of most of these paths is insignificant to cloud rendering (Nishita et al., 1996). Nishita et al. found that scattering illumination is dominated by the first and second orders, and therefore they only simulated up to the 4th order. They reduced the directions sampled in their evaluation of scattering to sub-spaces of high contribution, which are composed mostly of directions near the direction of forward scattering and those directed at the viewer. I simplify even further, and approximate multiple scattering only in a small solid angle around the light direction, and anisotropic single scattering in the eye direction.

I refer to multiple scattering in the light direction as *multiple forward scattering*. As I discussed in Section 2.2.5, the multiple forward scattering approximation is especially useful for clouds. Scattering by the large<sup>1</sup> water droplets that compose clouds is dominated by scattering in the forward direction. Therefore, even though this approximation ignores most of the sphere of exitant light directions, it still captures the essential portion of the scattering.

My cloud rendering method is a two-pass algorithm similar to the one presented in (Dobashi et al., 2000): I compute multiple forward scattering and absorption in the first pass, and use the results of this pass to render the clouds (thus computing scattering toward the viewpoint) in the second pass. The algorithm of Dobashi et al., used only an isotropic first order scattering approximation. If realistic values are used for the scattering and extinction coefficients of clouds shaded with only a first order scattering approximation, the clouds appear very dark (Max, 1995). This is because much of the illumination in a cloud is a result of multiple scattering. Figures 6.2 and 6.3 show the difference in appearance between clouds shaded with and without the multiple forward scattering approximation.

### 6.1.2 Validity of Multiple Forward Scattering

Figure 2.2 provides a visual demonstration that scattering by water droplets is strongly peaked in the forward direction. Some simple analysis provides more concrete support for the validity of the multiple forward scattering approximation.

The accuracy of the approximation is the fraction of the total scattering intensity that lies inside the solid angle of integration. To compute this accuracy, I integrated the scattering intensity over various solid angles (from 0 to  $4\pi$  steradians) centered about the forward direction, and divided the result by the integral over the full sphere. The plots in Figure 6.1 demonstrate that for a solid angle of integration of only 0.001 steradians,<sup>2</sup> the multiple forward scattering approximation accounts for more than half of the total scattering intensity. In other words, more than 50% of the incident light intensity is scattered into a small cone in the forward direction that accounts for less than 0.008% of the sphere of all exitant directions.

---

<sup>1</sup>Large relative to the wavelength of light, and to other particles in the atmosphere, such as air molecules and tiny dust particles.

<sup>2</sup>This is the solid angle subtended by a right circular cone with a vertex angle of less than 2 degrees.

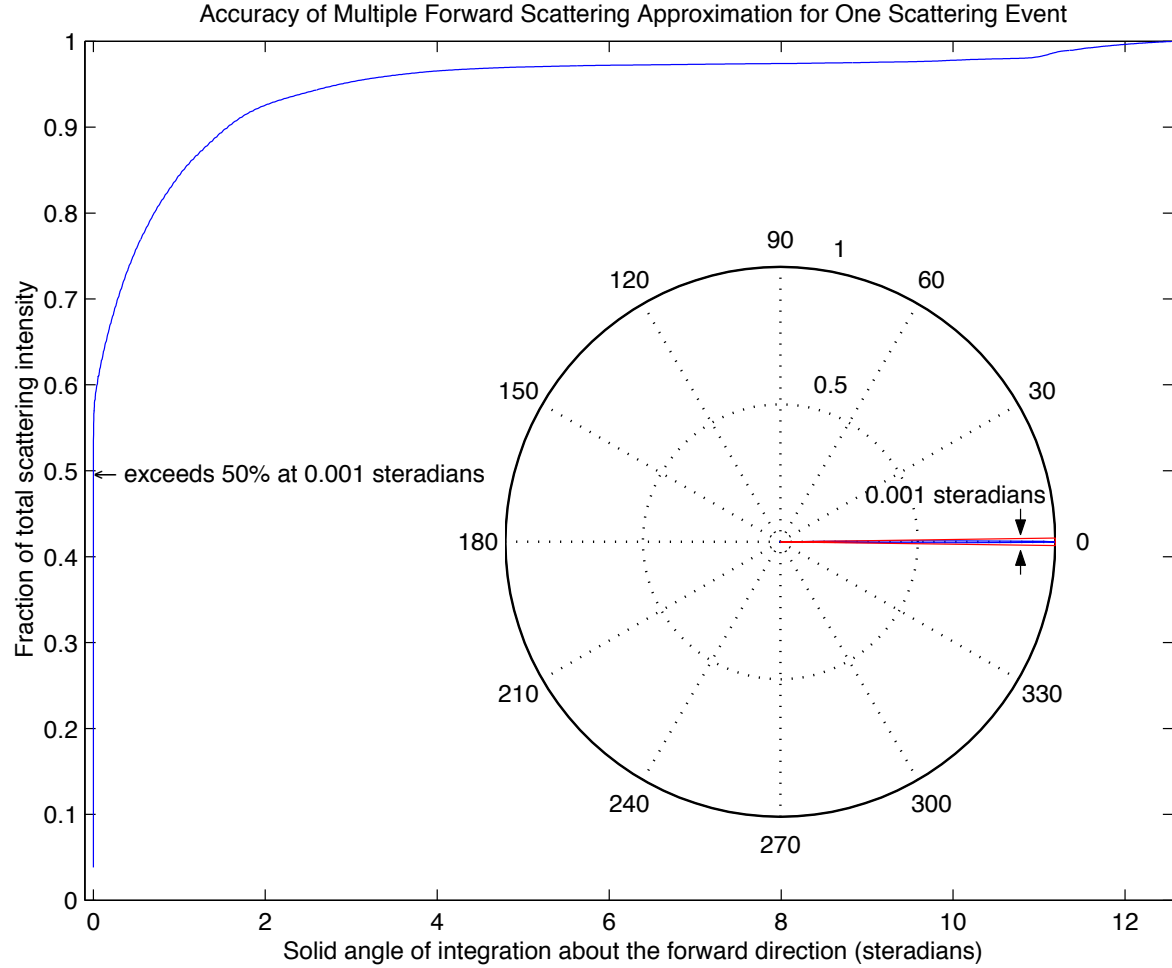


Figure 6.1: This figure demonstrates the validity of the multiple forward scattering approximation. The main plot shows the fraction of the total scattered intensity (for light of wavelength  $0.65\mu\text{m}$  incident on a  $25\mu\text{m}$  water droplet) for solid angles of integration between 0 and  $4\pi$  steradians (centered about the forward direction). The subplot is identical to Figure 2.2, and shows the scattering intensity on a linear scale. The arrow on the main plot shows that a solid angle of integration of only 0.001 steradians accounts for over 50% of the total scattering intensity. A wedge corresponding to this solid angle is overlaid on the polar plot to indicate that it captures the main forward peak. The data for these plots were calculated using *Mieplot* software (Laven, 2003).



Figure 6.2: These static particle-based clouds are illuminated with the single scattering approximation (in other words, no scattering is computed in the illumination pass), and are therefore unrealistically dark.



Figure 6.3: These clouds are illuminated using my multiple forward scattering algorithm. Multiple forward scattering propagates light much farther into the clouds.



Figure 6.4: These static particle-based clouds were rendered with isotropic scattering, and therefore lack the bright edges visible in real clouds.



Figure 6.5: These clouds were rendered with an anisotropic scattering phase function applied at each particle. The edges of the clouds are bright due to the strong forward scattering.

### 6.1.3 Computing Multiple Forward Scattering

As defined in Section 3.3.5, my cloud illumination algorithm is a *line integral method*, as is the algorithm of Dobashi et al. These algorithms traverse the cloud volume along the forward light direction, integrating extinction and in-scattering as they go.

I subdivide straight line paths through the cloud volume into  $N$  discrete steps. For static, particle-based clouds, the volume is not regularly sampled, so the distance between steps is non-uniform. Dynamic, voxel-based clouds are regularly sampled. My line integral algorithm works well for either representation, although it is more accurate for voxel clouds.

The first pass of the algorithm computes the amount of light in direction  $\vec{\omega}$  incident on each sample (particle or voxel) position. If sample  $n$  has position  $\vec{x}_n$ , then the incident radiance,  $L(\vec{x}_n, \vec{\omega})$ , is composed of direct (transmitted in direction  $\vec{\omega}$ ) and in-scattered light that does not undergo extinction on its way to  $\vec{x}_n$ . I modify the light transport equation (2.28), to obtain an equation for the radiance incident on sample position  $\vec{x}_n$ :

$$L(\vec{x}_n, \vec{\omega}) = L(0, \vec{\omega})T(0, D_n) + \int_0^{D_n} g(\vec{x}(s))T(s, D_n)ds. \quad (6.1)$$

Here,  $D_n$  is the depth of particle  $n$  in the cloud along the light direction,  $L(0, \vec{\omega})$  is the incident radiance,  $T(s, s') = e^{-\tau(s, s')}$  is the transmittance, and

$$g(\vec{x}) = K_s \int_{4\pi} P(\vec{\omega}, \vec{\omega}') L(\vec{x}, \vec{\omega}') d\vec{\omega}'. \quad (6.2)$$

$K_s$  is the scattering coefficient, and the function  $g(\vec{x})$  represents the light from all incident directions  $\vec{\omega}'$  scattered into direction  $\vec{\omega}$  at the point  $\vec{x}$ .  $P(\vec{\omega}, \vec{\omega}')$  is the phase function, introduced in Section 2.2.5. I assume that the scattering coefficient and phase function of the cloud are constant over changes in position, but in practice, it would be feasible to allow them to vary.

A full multiple scattering algorithm must compute the integral in  $g(\vec{x})$  using a sampling of all incident directions. As I discussed before, my algorithm computes only multiple scattering around the light direction,  $\vec{\omega}_l$ , so  $\vec{\omega}$  and  $\vec{\omega}'$  are both approximately  $\vec{\omega}_l$ . I assume that this direction sample actually covers a very small, but not infinitesimal solid angle,  $\gamma$ . Therefore, if I assume that the phase function and incident radiance are constant over  $\gamma$ , then Equation (6.2) can be approximated by  $g(\vec{x}) = \gamma K_s P(\vec{\omega}_l, \vec{\omega}_l) L(\vec{x}, \vec{\omega}_l) / 4\pi$ .

I subdivide the light path from 0 to  $D_n$  into  $N$  discrete segments,  $s_j$ . By approxi-

mating the integrals with Riemann Sums, I obtain

$$L_k = L(0, \vec{\omega})T_0^{k-1} + \sum_{i=0}^{k-1} g_i T_{i+1}^{k-1} \quad (6.3)$$

for the radiance incident on sample  $k$ , where the notation  $T_a^b$  represents the discrete transmittance<sup>3</sup>:

$$T_a^b = e^{\left(\sum_{i=a}^b -\tau_i\right)} = \prod_{i=a}^b e^{-\tau_i}.$$

The source term,  $g_i$ , is the discrete form of (6.2), using the multiple forward scattering approximation:

$$g_i = GL_i = \frac{\gamma K_s P(\vec{\omega}_l, \vec{\omega}_l)}{4\pi} L_i, \quad (6.4)$$

Where  $L_i = L(\vec{x}_i, \vec{\omega}_l)$ .  $G$  is a constant over the entire illumination computation.

In order to easily transform (6.3) into an algorithm that can be implemented in graphics hardware, I reformulate it as a recurrence relation:

$$L_k = \begin{cases} g_{k-1} + T_{k-1} L_{k-1}, & 2 \leq k \leq N \\ L_0, & k = 1. \end{cases} \quad (6.5)$$

$L_0 = L(0, \vec{\omega}_l)$  and  $T_k = e^{-\tau_k}$  is the transparency of sample  $k$ , so (6.5) expands to (6.3). This representation can be more intuitively understood. It states that starting outside the cloud and tracing along the light direction, the light incident on any sample  $k$  is equal to the intensity of light scattered to  $k$  from sample  $k-1$  plus the intensity transmitted through  $k-1$  (as determined by its transmittance,  $T_{k-1}$ ). Notice that if  $g_{k-1}$  is expanded in (6.5) then  $L_{k-1}$  is a factor in both terms. Section 6.1.6 explains how I combine color feedback (Section 4.2.4) with hardware blending to evaluate this recurrence.

### 6.1.4 Eye Scattering

In addition to approximating multiple forward scattering, I also implement single scattering toward the viewer. The recurrence for this is subtly different:

$$E_k = S_k + T_k E_{k-1} \quad (6.6)$$

---

<sup>3</sup>For  $a > b$ ,  $T_a^b = 1$

This equation states that the radiance,  $E_k$ , exiting any sample in the eye direction is equal to the radiance transmitted through it,  $T_k E_{k-1}$ , plus the light that it scatters into the eye direction,  $S_k$ . In the first pass, I compute the radiance  $L_k$  incident on each sample from the light source. The second pass generates the cloud image, so it must compute the portion of this radiance that is scattered toward the viewer. When  $S_k$  is replaced by  $K_s P(\vec{\omega}, \vec{\omega}_l) L_k / 4\pi$ , where  $\vec{\omega}$  is the eye direction, this recurrence approximates scattering toward the viewer.

It is important to mention that Equation (6.6) computes light emitted from particles using results ( $L_k$ ) computed in Equation (6.5). Because radiance is multiplied by the phase function in both recurrences, one might think that the same light is scattered twice at a single point. This is not the case, because Equation (6.5) computes radiance *incident* on each sample, and Equation (6.6) computes radiance *exitant* from each sample. In Equation (6.5),  $L_{k-1}$  is multiplied by the phase function to determine the amount of light that sample  $k - 1$  scatters in the forward (light) direction, and in (6.6)  $L_k$  is multiplied by the phase function to determine the amount of light that sample  $k$  scatters into the view direction. Even if the viewpoint is directly opposite the light source, because the light incident on sample  $k$  is stored and used in the scattering computation, scattering is never computed twice at a single point.

### 6.1.5 Phase Function

In Section 2.2.5 I discussed the scattering phase function. The phase function  $P(\vec{\omega}, \vec{\omega}')$  is very important to the appearance of clouds. Clouds exhibit anisotropic scattering of light—otherwise the multiple forward scattering approximation would not be accurate. The phase function determines the scattering distribution for a given particle or medium. The images in this section were generated using the simple Rayleigh scattering phase function, Equation (2.21). Rayleigh scattering favors scattering in the forward and backward directions, but occurs in nature only for aerosols of very small particles. Figures 6.4 and 6.5 demonstrate the differences between clouds shaded with and without anisotropic scattering. Anisotropic scattering gives the clouds their characteristic “silver lining” when viewed looking into the sun.

Most phase functions are easy to implement, so I have tried several, including Rayleigh, Schlick (Blasi et al., 1993), Henyey-Greenstein (Equation (2.22)), and Cornette-Shanks (Cornette and Shanks, 1992). These are listed in order of increasing physical accuracy in approximating scattering from the large water droplets of real clouds

(Premož et al., 2003). Rayleigh scattering, taken at face value, only accurately approximates scattering for particles much smaller than the wavelength of light. However, I have reasons for using it for clouds. First, it is very simple and can be computed much more cheaply than the others. This is important because it must be computed once per sample. Another reason to use it is that while real cloud droplets scatter most strongly in the forward direction, they do scatter some light into the rest of the sphere. After many scattering events, while the radiance is greatest in the forward direction, it is quite diffuse. Because Rayleigh scattering favors both forward, backward, and to a smaller extent, other directions of scattering, it ensures that clouds are not entirely dark when viewed opposite the forward direction, even though I compute multiple scattering only in the forward direction.

### 6.1.6 Cloud Rendering Algorithms

Armed with recurrences (6.5) and (6.6) and a standard graphics API such as OpenGL or Direct3D, computation of cloud illumination is straightforward. My algorithms are similar to the one presented in (Dobashi et al., 2000), with two phases: an illumination phase and a rendering phase. I describe two algorithms. The first, for static clouds represented as particles, runs the illumination phase once per scene at load time, and then runs the rendering phase in real time. The second, for dynamic clouds represented in a voxel grid, runs the illumination phase once every time step of the simulation, and runs the rendering phase in real time. The key to the illumination algorithm for both cases is the use of hardware blending and color feedback.

Blending operates by computing a weighted average of the frame buffer contents (the *destination*) and an incoming fragment (the *source*), and storing the result in the frame buffer. This weighted average is written

$$c_r = f_s c_s + f_d c_d. \quad (6.7)$$

Here  $f$  indicates a configurable multiplicative factor, and  $c$  is a fragment color. The subscripts  $r$ ,  $s$ , and  $d$  indicate *result*, *source*, and *destination*, respectively. By letting  $c_r = L_k$ ,  $f_s = 1$ ,  $c_s = g_{k-1}$ ,  $f_d = T_{k-1}$ , and  $c_d = L_{k1}$ , it is clear that Equations (6.5) and (6.7) are equivalent if the contents of the frame buffer before blending represent  $L_0$ . This is not quite enough, though. Because  $L_{k-1}$  is a factor of  $g_{k-1}$ . To solve the recurrence for sample  $k$  along a straight line path through the cloud, I must first determine the radiance incident on sample  $k - 1$ , so that  $g_{k-1}$  can be properly assigned

to  $c_s$  in Equation (6.7). To do this, I employ feedback.

## Static Cloud Illumination

For static clouds represented as a particle system, I use the following procedure to compute Equation (6.5), given in pseudocode in Algorithm 1. The cloud particles are first sorted in order of increasing distance from the light source. Then, the graphics API (Direct3D or OpenGL) is configured so that rendering the particles in order will result in a correct computation of Equation (6.5). The blending function is set so that  $f_s = 1$  and  $f_d = T_{k-1}$  (see Equation (6.7)). This is done by using `ONE` for the source blending factor and `ONE_MINUS_SRC_ALPHA` as the destination blending factor, because opacity (one minus transmittance) is stored in the *alpha channel* of each fragment. The view frustum is tightly fit to the cloud, directed along the light direction, and the projection matrix is set to orthographic, because the sun is distant enough that its rays may be assumed to be parallel. The frame buffer is cleared to pure white to represent the unattenuated radiance incident on the leading edge of the cloud.

After configuring the API, the particles are rendered in sorted order. They are rendered as small squares of side length equal to the diameter of each particle, textured with a gaussian splat. Hardware blending causes each particle to darken the covered pixels in the frame buffer by an amount proportional to attenuation of light by the particle, and lighten them by an amount proportional to forward scattering by the particle. Just before rendering each particle, the amount of incident radiance must be read and stored for the particle, so that it can be used both to compute forward scattering and later to display the cloud. I do this by computing a square region of pixels that covers the solid angle  $\gamma$ , and reading these pixels back from the frame buffer to host memory. The average intensity of these pixels is scaled by  $\gamma/4\pi$ . This is the radiance incident on sample  $k$  from sample  $k - 1$ . This radiance is pre-multiplied by the scattering coefficient and stored. The opacity of the particle is also computed and stored in the alpha channel. The particle is then rendered using the radiance scaled by the phase function as its color.

## Static Cloud Rendering

The display algorithm for static clouds is very similar to the illumination algorithm. The blending and texturing state are the same for both. In the display pass, the cloud is viewed using an unmodified camera frustum (in other words, the camera used to

---

**Algorithm 1** Pseudocode for computation of the illumination of static particle clouds.
 

---

```

view cloud from light position
particles.sort(<, distance to light)
tightly fit orthographic view frustum to cloud volume
clear frame buffer to white

blendFunc(src, dest) ←(ONE, ONE_MINUS_SRC_ALPHA)
textureMode ← MODULATE

 $\gamma \leftarrow$  solid angle of pixels to read

for all particles  $p_k$  do { $p_k$  has radius, color, and alpha}
  Compute pixels  $n_p$  needed to cover solid angle  $\gamma$ 
  Read  $n_p$  pixels in square around projected center of  $p_k$ 

   $L \leftarrow$  Average radiance of  $n_p$  pixels
   $p_k.\text{color} \leftarrow K_s * L * \text{light.color} * \gamma / 4\pi$ 
   $p_k.\text{alpha} \leftarrow 1 - \exp(-K * r_k)$ 

  render quad with color  $p_k.\text{color} * \text{phase}(\omega_l, \omega_l)$ , side length  $2 * p_k.\text{radius}$ 
end for
{Note: sort(<, distance from  $x$ ) means sort in ascending order by distance from  $x$ ,  

and  $>$  means sort in descending order.}
  
```

---

render the entire scene), and the particles are rendered in sorted order from back to front. This pass requires no frame buffer reads, because the radiance incident on each particle has been computed and stored. The phase function is applied to each particle before it is rendered. The direction from the viewer to the particle is determined, and is used with the light direction to compute the phase function (see 2.2.5). The result is multiplied by the stored particle color before rendering the particle. Listing 2 shows pseudocode for the display algorithm.

---

**Algorithm 2** Pseudocode for rendering static particle clouds.

---

```

view cloud from camera position
particles.sort(>, distance to eye)

blendFunc(src, dest) ←(ONE, ONE_MINUS_SRC_ALPHA)
textureMode ← MODULATE

 $\omega \leftarrow \text{normalize}(\text{view.position} - p_k.\text{position})$ 

for all particles  $p_k$  do { $p_k$  has radius  $r_k$ , color, alpha}
    render quad with color  $p_k.\text{color} * \text{phase}(\omega, \omega_l)$ , side length  $2 * p_k.\text{radius}$ 
end for

```

---

**Skylight** The most awe-inspiring images of clouds are the multi-colored spectacle of a beautiful sunrise or sunset. These clouds are often not illuminated directly by the sun at all, but by skylight—sunlight that is scattered by the atmosphere. The linear nature of light accumulation enables approximate computation of skylight on static clouds using a trivial extension to my algorithm. I simply shade clouds from multiple light sources and store the resulting particle colors ( $L_k$  in the algorithm) from all shading iterations. At render time, I evaluate the phase function at each particle once per light, and accumulate the results. By doing so, I approximate global illumination of the clouds. Two lights were used in Figure 6.6 to keep rendering cost low, but an arbitrary number can be used.

This technique is better than the standard ambient contribution often used in rendering, since it is directional and results in shadowing in the clouds as well as anisotropic scattering from multiple light directions and intensities. I obtain good results by guiding the placement and color of these lights using the images that make up the sky dome I place in the distance over my environments. Figure 6.6 demonstrates this with a scene at sunset in which I use two light sources—one orange and one pink—to create sunset

lighting. In addition to illumination from multiple light sources, I allow an optional ambient term to provide some compensation for lost scattered light due to the multiple forward scattering approximation.

## Dynamic Clouds

The algorithms I just described are intended for static clouds. The frame buffer reads used in the illumination phase are expensive, so I perform the illumination computation only once per scene. The rendering phase is inexpensive, because it simply renders the particles with simple blending. Dynamic clouds require that I modify the algorithm to support voxel clouds and to avoid reading data back to the host. Dynamic texturing (see Section 4.2.4) enables both of these.

**Oriented Light Volumes** To represent the illumination of a cloud volume, I use what I call an *Oriented Light Volume (OLV)*. An OLV stores radiance values in a 3D texture that is decoupled from the voxels in which the cloud water mixing ratios are stored (see Chapter 5). It is oriented so that its  $z$ -axis points toward the light position, and is tightly fit to the cloud voxel volume, as shown in Figure 6.7. Orienting the OLV along the light direction greatly simplifies the computation of the radiance at each of its voxels. The resolution of the light volume is independent of the cloud volume. Because the illumination of a cloud typically lacks high-frequency detail, I usually use an OLV with resolution half (in each dimension) that of the cloud volume. In order to properly explain my dynamic cloud illumination and rendering algorithms, I must first discuss sliced volume rendering.

**Sliced Volume Rendering** Volumetric datasets are common in computer graphics, especially in the area of medical imaging. These datasets are often acquired using medical scanning equipment that produces voxel volumes just like the volumes I use to represent cloud data. Several techniques for rendering voxel datasets have been developed (Levoy, 1988; Lacroix and Levoy, 1994; Cabral et al., 1994). With the advent of hardware support for 3D texturing, a common technique is *sliced volume rendering* (Wilson et al., 1994). This technique samples the volume using an array of parallel quadrilateral *slices* that are evenly-spaced in the view direction. The slices are rendered in order (either back-to-front or front-to-back), textured using the 3D texture, and blended in order to capture the transparency of the volume.



Figure 6.6: An example of shading from two light sources to simulate sky light. The static particle-based clouds in this scene were illuminated by two light sources, one orange and one pink. Anisotropic scattering simulation accentuates the light coming from different directions.

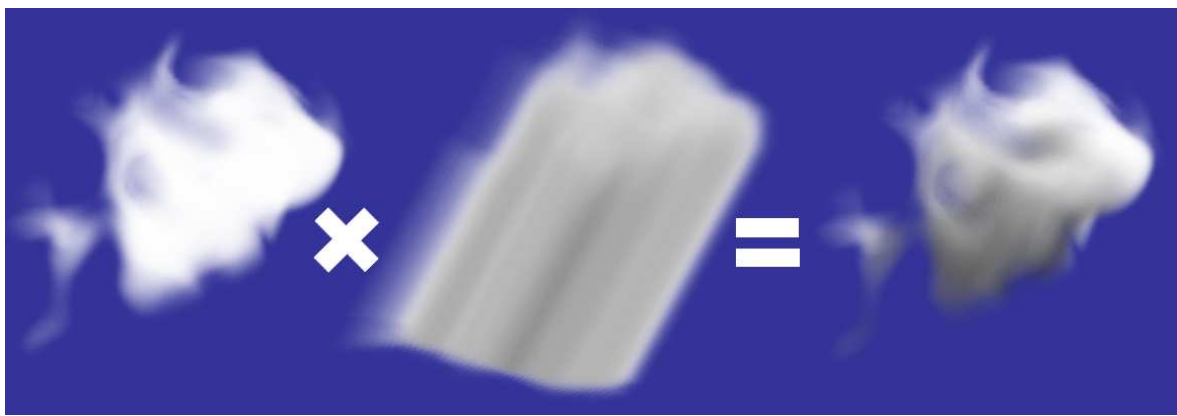


Figure 6.7: An example oriented light volume (OLV) illumination of a 3D cloud. Left: the cloud density volume without illumination. Middle: the OLV. Right: the cloud density volume illuminated via modulation by the OLV.

To texture the volume slices, the texture coordinates at the corners of each quadrilateral are generated so that they represent a 3D position in texture space. Because the viewpoint can change, the slicing planes can cut the volume in arbitrary directions, so the texture coordinates must be computed dynamically. Graphics APIs like OpenGL provide automatic texture coordinate generation functionality that converts 3D world-space positions into texture-space positions. The programmer need only enable the correct texture generation modes and render the slices. The generated texture coordinates are trilinearly interpolated by the hardware to correctly sample along the slicing polygon. This is the technique that I use to render dynamic cloud volumes, as well as to compute their illumination.

**Dynamic Cloud Illumination** Because they are derived from the same mathematics, the algorithm for computing the radiance of each texel in the OLV texture is similar to the algorithm I described previously for static clouds. It is shown in pseudocode in Algorithm 3. This algorithm uses the same blending and texturing settings as the algorithm for static clouds, but avoids frame buffer reads by using the OLV texture itself to compute the forward-scattered radiance. It does this by updating each slice of the 3D texture in order along the light direction by rendering into the frame buffer, and then copying the frame buffer into the 3D texture slice.

The view frustum, projection matrix, and blending function are set as in the static cloud algorithm. The texture coordinate generation modes and texture matrix are set as shown in Algorithm 3. A translation is applied to the texture matrix on texture unit 1 so that all texture lookups for a slice will address the previously computed slice, thus propagating radiance through the volume as in Recurrence (6.5). The frame buffer is cleared to pure white. The cloud water content texture is activated on texture unit 0, and the OLV texture is activated on unit 1. The four corners of a quadrilateral are computed such that they match the four corners of the frustum, parallel to the view plane. The depth ( $z$ -coordinate) of the corners is initialized to 0, so that the plane touches the leading edge of the cloud volume. Texture coordinates are computed to address a single slice of the OLV texture.

At each iteration, the frame buffer image is first copied into the current slice of the OLV texture. Then, a quadrilateral slice is rendered at the current slice depth. Texturing and blending results in darkening of each pixel of the frame buffer by an amount proportional to attenuation of light by the previous slice sample, and lightening by an amount proportional to forward in-scattering from the previous slice sample. This

technique directly implements Equation (6.5). On the next iteration, this slice will be used to compute the illumination of the next slice, due to the texture matrix translation. The depths of the quadrilateral corners are incremented by the distance between slices.

**Display pass** Once the OLV texture is computed, it can be used to generate a cloud image. To do this, the cloud volume is sliced in the view direction, rather than the light direction. The slices are rendered from back to front, and no texture copies are performed. During this pass, texturing from the OLV texture directly incorrectly assumes that its axes are the same as the world-space axes. To use the OLV texture correctly, the orientation portion (the upper-left  $3 \times 3$  portion) of the texture matrix for texture unit 1 must be set to the orthonormal basis formed by the three axis vectors of the OLV—this is a matrix that rotates the automatically generated texture coordinates from the cloud density texture space into the OLV texture space. Texture coordinate generation is enabled as in the illumination pass. The combination of automatic texture coordinate generation and the texture matrix correctly transform all illumination texture sample positions into the texture space of the OLV. Figure 6.7 demonstrates how multiplication of the cloud volume by the OLV results in an illuminated cloud.

I discussed the application of the phase function to particles in Section 6.1.6. For voxel clouds, the phase function must be applied per pixel. In order to do so, a fragment program must be used when performing the sliced volume rendering. The fragment program computes the direction to the eye at each fragment, and uses that along with the light direction (a parameter) to compute the phase function. The difficulty is that this program is run for every fragment drawn when rendering the cloud volume. For a cloud that fills a large window, the cost is prohibitive, because every pixel of every slice of the cloud invokes the fragment program.

In my tests, even the simple Rayleigh phase function was too expensive. Therefore, the simulated clouds in the images in chapter 5 do not exhibit anisotropy. One possible optimization would be to precompute a lookup table for the phase function to save computation. In fact, the lookup table could be stored in a cube map. A cube map is a set of 6 textures, one for each of the faces of a cube, which are indexed together using 3D texture coordinate. In this case the view direction would be used as texture coordinates, and the texture matrix would be used to account for changing light directions. This would replace most of the computation with a texture lookup.

---

**Algorithm 3** Pseudocode for computation of the illumination of dynamic volume clouds. This algorithm computes an OLV texture.

---

view cloud from light position  
 tightly fit orthographic view frustum to cloud volume  
 set viewport resolution to OLV slice resolution  
 clear frame buffer to white

$n \leftarrow$  number of OLV slices  
 $d \leftarrow$  OLV slice spacing  
 $z \leftarrow 0$

Enable user clip planes at each edge of cloud volume

`blendFunc(src, dest)  $\leftarrow$  (ONE, ONE_MINUS_SRC_ALPHA)`

{These settings will compute 3D texture coordinates from object space coordinates.  
They should be set for texture units 0 and 1.}

TexGen Mode  $\leftarrow$  OBJECT\_LINEAR  
 TexGen OBJECT\_PLANE\_S  $\leftarrow$  (0.5, 0.0, 0.0, 0.5)  
 TexGen OBJECT\_PLANE\_T  $\leftarrow$  (0.0, 0.5, 0.0, 0.5)  
 TexGen OBJECT\_PLANE\_R  $\leftarrow$  (0.0, 0.0, 0.5, 0.5)  
 Enable TexGen on texture units 0 and 1

{Translate OLV texture lookups to previous slice to get incident radiance}  
 Set Texture Matrix on texture unit 1 to translate (0, 0, 1 / n)

Bind cloud density texture to texture unit 0, textureMode  $\leftarrow$  MODULATE  
 Bind OLV texture to texture unit 1, textureMode  $\leftarrow$  MODULATE

$\text{slicequad} \leftarrow$  viewport-sized quad parallel to view plane  
 $\text{slicequad.color} \leftarrow K_s * \text{light.color} * \text{phase}(\omega_l, \omega_l)$   
 $\text{slicequad.alpha} \leftarrow 1 - \exp(-K * d)$

---

**for**  $i = 1$  to  $n$  **do** {Render slices from front to back.}  
 Copy frame buffer to OLV texture slice  $i$   
 Display slicequad at depth  $z$   
 $z \leftarrow z + d$   
**end for**

---

---

**Algorithm 4** Pseudocode for rendering dynamic volume clouds using an OLV for illumination.

---

Use scene rendering camera and viewport settings

$n \leftarrow$  number of OLV slices  
 $d \leftarrow$  OLV slice spacing  
 $z \leftarrow$  distance to opposite side of cloud volume

$\text{blendFunc(src, dest) } \leftarrow (\text{ONE}, \text{ONE_MINUS_SRC_ALPHA})$

Enable user clip planes at each edge of cloud volume

{These settings will compute 3D texture coordinates from object space coordinates.  
They should be set for texture units 0 and 1.}  
TexGen Mode  $\leftarrow$  OBJECT\_LINEAR  
TexGen OBJECT\_PLANE\_S  $\leftarrow (0.5, 0.0, 0.0, 0.5)$   
TexGen OBJECT\_PLANE\_T  $\leftarrow (0.0, 0.5, 0.0, 0.5)$   
TexGen OBJECT\_PLANE\_R  $\leftarrow (0.0, 0.0, 0.5, 0.5)$   
Enable TexGen on texture units 0 and 1

{Rotate OLV texture lookups into world space from OLV space}  
Set Texture Matrix on texture unit 0 to rotate OLV to align with  $\omega_l$

Bind cloud density texture to texture unit 0, textureMode  $\leftarrow$  MODULATE  
Bind OLV texture to texture unit 1, textureMode  $\leftarrow$  MODULATE

slicequad  $\leftarrow$  viewport-sized quad parallel to view plane  
slicequad.color 1  
slicequad.alpha  $\leftarrow 1 - \exp(-K * d)$

Enable fragment program to compute Recurrence (6.6)

---

**for**  $i = 1$  to  $n$  **do** {Render slices from back to front.}  
    Display slicequad at depth  $z$   
     $z \leftarrow z - d$   
**end for**

---

## 6.2 Efficient Cloud Rendering

The cloud rendering algorithms I just described produce beautiful results, but they can burden the GPU when rendering many static clouds or high-resolution dynamic cloud volumes. The interactive applications for which I developed the algorithms require complicated cloud scenes to be rendered at fast interactive rates. Clouds are only one component of a complex application, and therefore can only use a small percentage of a frame time, with frame rates of thirty per second or higher.

Rendering many cloud particles or volume slices results in high rates of pixel overdraw. Clouds have inherently high depth complexity, and require blending, making rendering expensive even for current hardware with the highest pixel fill rates. In addition, as the viewpoint approaches a cloud, the cloud's projected area increases, becoming greatest when the viewpoint is within the cloud. Thus, pixel overdraw is increased and rendering slows as the viewpoint nears and enters clouds.

In order to render complex cloudy scenes at high frame rates, I need a way to bypass fill rate limitations, either by reducing the amount of pixel overdraw performed, or by amortizing the rendering of clouds over multiple frames. Dynamically generated impostors allow me to do both.

An impostor replaces an object in the scene with a semi-transparent polygon texture-mapped with an image of the object it replaces, as shown in Figure 6.8 (Maciel and Shirley, 1995; Schaufler, 1995; Shade et al., 1996). The image is a rendering of the object from a viewpoint  $V$  that is valid (within some error tolerance) for viewpoints near  $V$ . Impostors used for appropriate points of view give a very close approximation to rendering the object itself. An impostor is valid (with no error) for the viewpoint from which its image was generated, regardless of changes in the viewing *direction*. Impostors may be precomputed for an object from multiple viewpoints, requiring much storage, or they may be generated only when needed. I use the latter technique, called *dynamically generated impostors* by (Schaufler, 1995).

I generate impostors using the following procedure. A view frustum is positioned so that its viewpoint is at the position from which the impostor will be viewed (the *capture point*), and it is tightly fit to the bounding volume of the object (see Figure 6.9). I then render the object into an image used to texture the impostor polygon.

I use impostors to amortize the cost of rendering clouds over multiple frames by exploiting the frame-to-frame coherence inherent in three-dimensional scenes. The relative motion of objects in a scene decreases with distance from the viewpoint, and

objects close to the viewpoint present a similar image for some time. This lack of sudden changes in the image of an object enables the re-use of impostor images over multiple frames. I compute an estimate of the error in an impostor representation that I use to determine when the impostor needs to be updated. Schaufler presented two worst-case error metrics for this purpose (Schaufler, 1995). The first, which I call the *translation error*, computes error caused by translation from the capture point. The second—the *zoom error*—computes error introduced by moving straight toward the object.

I use the same translation error metric as Schaufler, but I replace his zoom error metric by a texture resolution error metric. For the translation error metric, I simply compute the angle  $\phi_{trans}$  induced by translation relative to the capture point (see Figure 6.9), and compare it to a specified tolerance. The texture resolution error metric compares the current impostor texture resolution to the required resolution for the texture, computed using the following equation (Schaufler, 1995).

$$res_{tex} = res_{screen} * \frac{object\ size}{object\ distance} \quad (6.8)$$

If either the translation error is greater than an error tolerance angle or the current resolution of the impostor is less than the required resolution, I regenerate the impostor from the current viewpoint at the correct resolution. I find that a tolerance angle of about  $0.15^\circ$  reduces impostor “popping” to an imperceptible level while maintaining good performance. For added performance, tolerances up to  $1^\circ$  can be used with only a little excessive popping.

Impostors were originally intended to replace geometric models. Since these models have high frequencies in the form of sharp edges, impostors have usually been used only for distant objects. Nearby objects must have impostor textures of a resolution at or near that of the screen, and their impostors require frequent updates. I use impostors for clouds no matter where they are in relation to the viewer. Clouds have fewer high frequency edges than geometric models, so artifacts caused by low texture resolution are less noticeable. Clouds have very high fill rate requirements, so cloud impostors are beneficial even when they must be updated every few frames.

### 6.2.1 Head in the Clouds

Impostors can provide a large reduction in overdraw even for viewpoints inside the cloud, where the impostor must be updated every frame. The “foggy” nature of clouds makes it difficult for the viewer to discern detail when inside them. In addition, in games and flight simulators, the viewpoint is often moving. I have found that these factors allow me to reduce the resolution of impostor textures for clouds containing the viewpoint by up to a factor of 4 in each dimension. However, impostors cannot be generated in the same manner for these clouds as for distant clouds, since the view frustum cannot be tightly fit to the bounding volume as described above. Instead, I use the same frustum used to display the whole scene to generate the texture for the impostor, and display the impostor as a screen-space rectangle sized to fill the screen.

### 6.2.2 Objects in the Clouds

In order to create effective interactive cloudy scenes, objects must be allowed to pass in and through the clouds, and I must render this effect realistically. Impostors pose a problem because they are two-dimensional. Objects that pass through impostors appear as if they are passing through images floating in space, rather than through fluffy, volume-filling clouds.

One way to solve this problem would be to detect clouds that contain objects and render their particles directly to the frame buffer. By doing so, however, I lose the benefits of impostors. Instead, I detect when objects pass within the bounding volume of a cloud, and split the impostor representing that cloud into multiple layers. If only one object resides in a certain cloud, then that cloud is rendered as two layers: one for the portion of the cloud that lies approximately behind the object with respect to the viewpoint<sup>4</sup>, and one for the portion that lies approximately in front of the object. If two objects lie within a cloud, then I use three layers, and so on. Since cloud particles and slices must be sorted for rendering, splitting the cloud into layers adds little expense. This “impostor splitting” results in a set of alternating impostor layers and objects. The set is rendered from back to front, with depth testing enabled for objects, and disabled for impostors. The result is an image of a cloud that realistically contains objects, as shown on the right side of Figure 6.10.

Impostor splitting provides an additional advantage over direct rendering of clouds

---

<sup>4</sup>I consider particles or slices to be behind an object if they are farther from the eye than its center point.



Figure 6.8: An outside view of dynamically generated impostor images applied to view-oriented billboard polygons (represented by the yellow outlines). From the point of view of the camera frustum shown in white, the clouds appear three-dimensional.

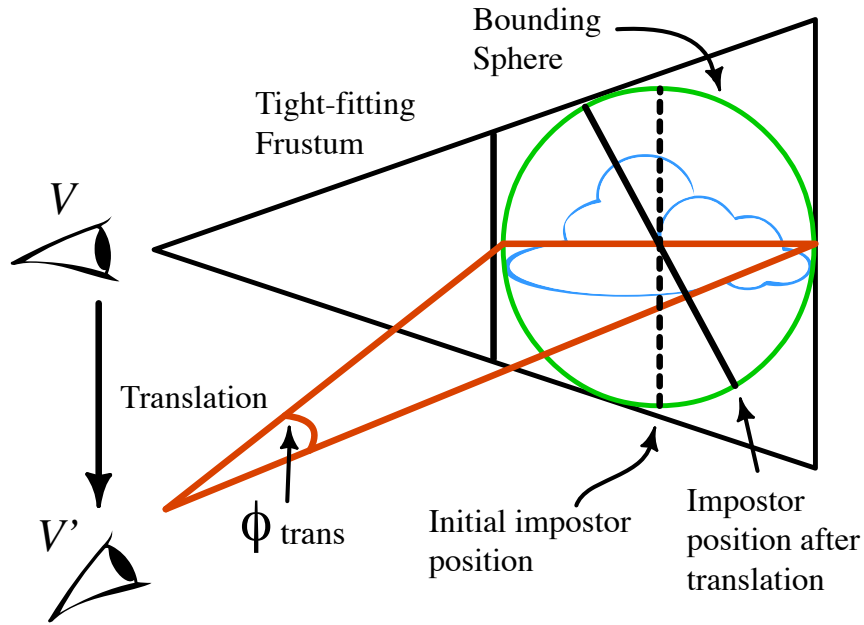


Figure 6.9: An impostor is generated for a viewpoint  $V$ . Error is introduced when the viewpoint is translated to  $V'$ . The impostor is reused until the angle  $\phi_{trans}$  becomes larger than a user-specified tolerance.



Figure 6.10: An airplane in the clouds. Left: particles directly rendered into the scene cause visible artifacts where the particle geometry intersects the airplane geometry. Right: impostor splitting removes the artifacts, because the airplane is composited between two impostor layers without depth testing.

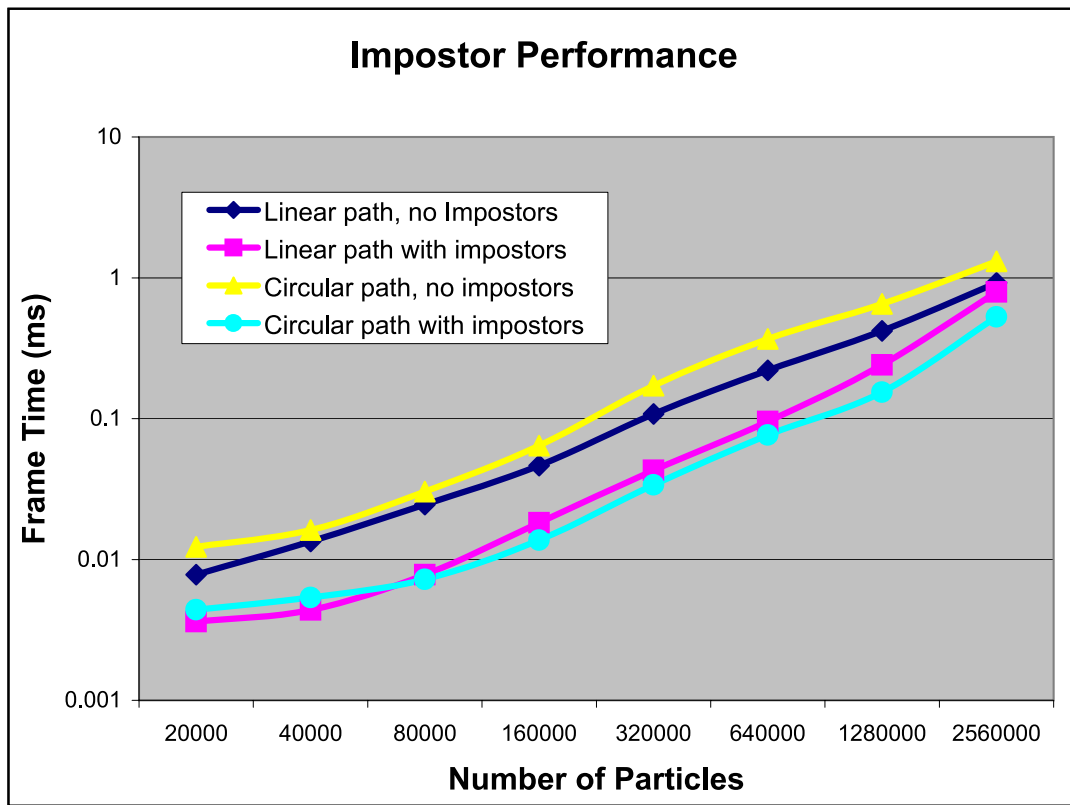


Figure 6.11: This graph plots the performance (circa 2000) of rendering scenes of increasing numbers of particles with and without impostors. Scenes were composed of randomly placed, non-overlapping 200-particle clouds.

that contain objects. When rendering cloud particles and slices directly, the polygons used to render them may intersect the geometry of nearby objects. These intersections cause artifacts that break the volumetric illusion of the cloud. Impostor splitting avoids these artifacts (see Figure 6.10).

## 6.3 Results

I have built a framework for rendering clouds called *Skyworks* that uses dynamically generated impostors as I described in the previous section. The impostors are independent of the type of clouds to which they are applied. I have used them for both static particle-based clouds and dynamic voxel-based clouds.

### 6.3.1 Impostor Performance

I originally tested the performance of impostors in the spring of 2000 on a Windows PC. On this machine, my system achieved high frame rates by using impostors and view-frustum culling to accelerate rendering. I rendered scenes containing over one hundred thousand particles at high frame rates (greater than 50 frames per second). As long as the viewpoint moved slowly enough to keep impostor update rates low, I was able to render a scene of more than 1.2 million particles at about 10 to 12 frames per second. Slow movement is a reasonable assumption for flight simulators and games because the user's aircraft is typically much smaller than the clouds through which it is flying, so the frequency of impostor updates remains low.

I performed several tests of my cloud system. The test machine was a PC with 256 MB of RAM, an 800 MHz Intel Pentium III processor, and an NVIDIA GeForce 256<sup>5</sup> GPU with 32MB of video RAM. The tests rendered scenes of increasing cloud complexity (from 100 to 12,800 clouds of 200 particles each) with and without using impostors. I also tested the performance for different types of movement. The first test moved the camera around a circular path, and the second moved the camera through the clouds in the direction of view. The results of my tests are shown in Figure 6.11. The chart shows that using impostors improves frame rates over the large range of scene complexity covered by the tests, and that even for scenes with several hundred thousand particles I achieved interactive frame rates.

---

<sup>5</sup>The NVIDIA GeForce 256 GPU was the first with the name ‘GeForce’. Thus, it is an earlier, slower processor than any of the other GeForce GPUs, including the GeForce 4 and GeForce FX.

More recently, I ran a test that rendered more than 1200 clouds of over 3000 particles each (for a total of more than four million particles) at 30 to 150 frames per second on a 2 GHz Pentium 4 PC with an NVIDIA GeForce 4 Ti 4600 GPU. Recent GPUs are very fast, but the speed improvements of impostors remain important. The latest GPUs could easily handle thousands of particles without impostors, but more complex scenes with millions of particles still pose a problem. Sliced-based volume rendering benefits greatly from my impostor system, because of the high overdraw of direct rendering.

### 6.3.2 Illumination Performance

For static clouds, the illumination phase is a preprocess. On the Pentium III PC system described above, scenes with a few thousand particles could be illuminated in less than a second, and scenes of a few hundred thousand particles required about five to ten seconds per light source. On today's PCs, the illumination phase is a few times faster.

The OLV illumination algorithm for dynamic clouds is executed whenever a simulation time step completes. To ensure a smooth frame rate, I use simulation amortization for the illumination computation just as I do for the simulation. In a stand-alone (unamortized) test on an NVIDIA Quadro FX 1000 GPU, I found that for a  $128 \times 128 \times 128$  cloud volume, computation of  $128 \times 128 \times 128$ ,  $64 \times 64 \times 64$ , and  $32 \times 32 \times 32$  OLVs required about 100 ms, 16 ms, and 4 ms, respectively.

## 6.4 Summary

This chapter presented the last stage in my cloud system—illumination and rendering of volumetric clouds. Using the light transport equations from Chapter 2, I derived a general cloud illumination algorithm (Section 6.1.3). Based on this general algorithm, I described algorithms for illuminating static particle-based clouds and dynamic voxel-based clouds (Section 6.1.6). These algorithms integrate multiple forward scattering and attenuation of light through clouds, resulting in realistic, self-shadowed cloud volumes. To improve rendering performance, I use dynamically generated impostors (Section 6.2). I presented extensions to traditional impostors that allow them to be used for clouds containing the viewpoint (Section 6.2.1) and other objects (Section 6.2.2). The end result of these algorithms is realistic, real-time cloud rendering. In the next chapter, I conclude with a summary of my dissertation work, including limitations and ideas for future work.

# Chapter 7

## Conclusion

In this dissertation I have described a system for real-time simulation and rendering of realistic, dynamic clouds suitable for interactive applications such as flight simulators and games. These applications demand realism, but they cannot afford to sacrifice speed to achieve it. I developed my algorithms and techniques with these requirements in mind. My algorithms are not only efficient; they also provide ways to trade quality for performance, and to amortize computation over many rendering frames in order to preserve high frame rates.

The main results of my dissertation work are as follows.

- I have adapted equations from the cloud dynamics literature into a realistic dynamics model for clouds that is suitable for visual simulation. The components of the model, including fluid dynamics, thermodynamics, and water continuity, interact to form the complex convective fluid motion and phase changes that govern the formation, evolution, and dissipation of clouds. (Chapter 2)
- I have demonstrated a high-performance simulation of the cloud dynamics model implemented on graphics hardware. In the process, I have developed the idea of flat 3D textures, a novel representation for 3D textures that allows an entire 3D texture to be updated in a single pass, making better use of GPU parallelism. (Chapter 5)
- I have implemented a technique for amortizing the cost of dynamics simulation over multiple rendering frames, allowing applications to run at high frame rates while simulating clouds. (Section 5.5)

- I have derived and implemented efficient algorithms for simulating multiple forward light scattering in two types of cloud models: static particle-based clouds and dynamic voxel-based clouds. (Chapter 6)
- I have demonstrated that dynamically generated impostors are especially well suited to accelerating cloud rendering. I have shown that with some simple modifications, impostors can even be applied to clouds that contain other objects. (Section 6.2)
- In addition to my cloud simulation and rendering algorithms, I have demonstrated a variety of other physically-based simulations executed on GPUs. These include Navier-Stokes fluid flow, chemical reaction-diffusion, and coupled map lattice models for boiling and Rayleigh-Benard convection. I implemented the last three of these on DX8-class GPUs that lack floating point support and have limited instruction sets. (Chapter 4)

Thus, I have demonstrated that realistic clouds can be simulated and rendered in real time using efficient algorithms implemented entirely on programmable graphics processors. To my knowledge, my work is the first in computer graphics to simulate both cloud dynamics and radiometry in real time.

## 7.1 Limitations and Future Work

In this section I list the major limitations of my work, and address most of them with ideas for future work. The multiple facets of my dissertation suggest several directions for future exploration, including visual and physical improvements for clouds, creative control, and new directions and applications for general-purpose computation on GPUs.

### 7.1.1 Cloud Realism

The most obvious direction for the future is to continue to improve the quality and realism of clouds. A number of limitations and problems with my current simulation provide goals for future work.

#### Visual Detail

The most important limitation of my cloud simulation system is the scale and detail that it can support. It is not currently possible to simulate a sky full of clouds. The domain

size of most of the simulations that I have run is about 3–5 km in each dimension. While twice that would be sufficient to simulate tall clouds (and 3 times that would cover the entire troposphere—15 km tall), the horizontal scale is not large enough. When flying, one quickly exceeds such a distance. For a flight simulator, clouds must extend as far as the user desires to fly. The grid cells I use in my simulations are 50–100 m. This level of detail is already noticeably blocky when flying near them, and it is hard to see the swirls and vortices that can be seen in my relatively higher-resolution 2D simulations. Currently, increasing detail requires decreasing scale, and vice versa.

The basic reason for scale and detail limitations is that volumetric data require immense computation and storage resources. Fortunately, GPUs are rapidly increasing both of these resources. I expect GPUs to be able to handle 4–16 times larger simulations in 2–3 years. This will help, but it will not solve the problem of populating the skies with dynamic clouds. More creative techniques will be required.

An additional problem is that convergence of linear solvers is more difficult on large grids (Briggs et al., 2000). Therefore, it might be necessary to use a more sophisticated solver. The multigrid method is especially good at achieving good convergence on large grids, and can be implemented on the GPU (Bolz et al., 2003; Goodnight et al., 2003).

A possible method of creating higher detail at lower cost is to use procedural noise techniques. Much work has been done in the past on generating clouds using noise (Lewis, 1989; Ebert, 1997; Ebert et al., 2002; Schpok et al., 2003). Recently, Perlin and Neyret made the observation that while noise is a very useful primitive for creating texture detail, it does not work well for describing flowing detail. It lacks “swirling” and advection behavior. To overcome this, they presented a few simple extensions to Perlin Noise (Perlin, 1985) that make the noise appear to flow more realistically (Perlin and Neyret, 2001). Very recently, Neyret has also presented a method for overcoming problems of basic advection of textures to add detail to flows (Neyret, 2003). I think an interesting avenue of research would be to combine techniques for advecting procedural noise with my physical cloud simulation. It may be possible to add believable detail to clouds much more cheaply than can be simulated at high resolution.

Problems of scale can be approached from a number of directions. One technique, that may also help add detail, is to explore adaptive and hierarchical simulation techniques. Such a technique would spend less computation and storage on areas where clouds are not forming, and more in areas of high cloud detail. One technique would be to use multiple small simulation volumes to represent individual clouds, and update them less frequently (see Section 7.1.2 for more thoughts about representing individual

clouds).

A level-of-detail approach could be used to spend fewer resources in the distance and outside of the user's field of view, and concentrate on what is near and visible. The difficulty with such techniques would be keeping the dynamics consistent—if the user looks away, and then back, the clouds should look the same. Like simulation amortization, this is another opportunity to draw on the relatively slow motion of clouds. It may be the case that the user will not notice inconsistencies in cloud formations if changes are not drastic. Stephen Chenney has done work on maintaining simulation consistency under dynamics culling (Chenney and Forsyth, 1997).

Another approach is to use periodic boundaries. This can be done on the scale of a single simulation volume. Currently, I use periodic boundaries only for water vapor, not condensed water, because I wanted to avoid clouds appearing periodic on my small simulation grids. However, I never determined if the repetition is noticeable when the user is immersed in the cloud volume. Alternatively, if multiple simulation volumes are used, then individual clouds may be “warped” from behind the user into the distance ahead. This technique is often used for objects in the continuous worlds of games.

## Visual Consistency

Because of the large time steps that I use, and because simulation amortization separates cloud updates by many rendering frames, the transition between time steps is quite visible, in the form of “pops” between time steps. A simple way to avoid this is to maintain both the current cloud texture and the previous texture, and to blend between them over several frames at each transition. This would smooth out the popping, possibly making it imperceptible. Another technique might be to use the current velocity field to advect the current cloud texture a little each frame. This is only an approximation, but it may look better than blending. However, it would be much more expensive than blending, and may prohibit interactive rendering.

Another problem of visual consistency concerns impostors. The impostors that I use are intended to represent individual objects. When clouds are close together, their impostors may intersect, causing parts of the clouds to appear to pop in front and behind each other. For static clouds, I solved this problem by making sure no two cloud bounding spheres overlapped. For dynamic clouds, the same technique could be used, but I have not needed it because I have only simulated at most one cloud volume at a time. A better solution might be to use a hierarchical impostor technique, such as the “hierarchical image cache” of (Shade et al., 1996). This way, clouds may be

placed anywhere, because particle overlaps are not a problem. Such a technique would be beneficial for large cloud volumes, too. Currently, I use a single impostor for the entire cloud volume. As the cloud volume resolution increases, impostor updates will become more expensive. A hierarchy will help reduce this expense.

## The Physical Model

There are many ways in which my cloud simulation can be made more physically realistic. Atmospheric physicists typically use much more complex and detailed models than I have used (Houze, 1993; Rogers and Yau, 1989). I kept my model simple to facilitate high simulation rates.

One possible addition to the model would be to use a more detailed water continuity model. The two state model that I use cannot represent precipitation (which may be interesting for flight simulation), because it only models cloud water. Adding rain water would require a model for the coalescence of small water droplets into larger ones, and for the effects on velocity and cloud water content of falling rain. Also, there is a whole class of clouds that my model cannot represent: clouds that are composed of tiny ice crystals or a mix of water and ice. This would add more phase changes to the model—freezing, melting, deposition, and sublimation. The literature on cloud microphysics can be drawn upon for more details (Houze, 1993; Rogers and Yau, 1989).

Another detail that I left out of my simulation is the idea of Cloud Condensation Nuclei (CCN). Water typically condenses on surfaces. Spontaneous condensation of pure water in air, called *homogeneous nucleation*, requires relative humidity of several hundred percent or higher (Rogers and Yau, 1989). Clouds typically condense at just above 100 percent, because they condense on CCN, which are small particles in the air. Some CCN, such as salt particles over the ocean, allow water to condense at much lower saturation levels. Therefore, modeling the effect and concentration of CCN on cloud formation would be an interesting step. Overby et al. used a simple constant factor to approximate the effects of CCN (Overby et al., 2002).

My current cloud model assumes that clouds exist alone. There are no solid boundaries other than the ground, and no interior boundaries in the simulation domain. In order to represent the effects of terrain (such as tall mountains) on the clouds, arbitrary boundary conditions would need to be evaluated. Interior boundaries are common in fluid dynamics simulations. Such boundaries can be implemented as described in (Griebel et al., 1998). Once this is done, it would be very interesting to incorporate moving boundaries, as (Fedkiw et al., 2001) did for smoke. In this way, one could

simulate the effects of aircraft on the clouds, because the moving boundaries of the aircraft would change the air flow.

Finally, I have not compared the results of a GPU cloud simulation to measured data from real clouds. Model verification is a common feature of cloud dynamics research in the atmospheric sciences. Data collected from mountain observatories and from flight through clouds is available (Rogers and Yau, 1989). This data could be used for comparison, depending on the level of detail of the simulation. This leads to another interesting direction—moving beyond visual simulation to accurate numerical simulation. To do so may require higher precision computation, as I discuss in Section 7.1.3.

## Radiometry

Improvements in the radiometry simulation may be beneficial. My multiple forward scattering approximation produces good results for interactive applications, but as more computational power becomes available, it may be desirable to spend some of it on a more realistic scattering model. One existing problem is the expense of computing the phase function for voxel-based clouds. A method for reducing this cost is needed (see Section 6.1.6).

My dynamics model does not take into account the effects of radiometry on cloud dynamics. Sunlight has warming effects on clouds and on the earth below. When clouds grow thick, they shadow the earth, which cools it, and reduces updrafts. This effects the air currents, the movement of water vapor, and the formation and motion of clouds. My illumination model results in a shadow map (for the particle-based algorithm) or volume (OLV) that could be used to shadow terrain below the clouds, and possibly determine which areas are warmer than others.

### 7.1.2 Creative Control

Games are developed by both programmers and artists. Because games often tell stories and have strong visual themes, artistic control of all features is essential. Therefore, methods of controlling physically-based cloud simulations (not to mention simulations of other phenomena) are a useful direction for future work. My simulation provides simple controls over atmospheric parameters; but these require an understanding of how clouds form. More intuitive controls—“more wispy”, “more lumpy”—would be an interesting idea to pursue.

My static particle-based clouds provide much more artistic control than my dynamic clouds simply because they must be constructed by hand (or at least their general shape must be constructed—see Section 6.1). The nice thing about this is that the artist has control over each individual cloud. With a dynamic simulation, the control applies to a *field* in which clouds—possibly multiple clouds—may form. It would be nice to have control over the number, shape, and size of clouds that form in a simulated field. The ability for an artist to say “place a single, dynamic fair-weather cumulus cloud here” would be very powerful.

### 7.1.3 GPGPU and Other phenomena

General-purpose computation on GPUs is an area of research that I find very interesting. I think that GPUs will see increasing use in computer games for procedural texturing and physically-based simulation. Also, the low cost, high speed, and parallelism of GPUs makes them ideal in many ways for scientific computing. Imagine giant clusters of PCs with powerful GPUs crunching through massive physical and numerical simulations.

In order to achieve this, some limitations must be removed. For example, current GPUs support only single-precision (32-bit) floating point numbers. This precision is currently more than enough for the rendering required by computer games, but many scientific simulations require double precision. It is unclear whether or not demand for this precision from the scientific computing community would be enough to convince GPU manufacturers to support it.

I look forward to seeing many different phenomena simulated on GPUs—possibly at interactive rates that weren’t achievable before. For example, my cloud simulation model, with the exception of moving interior boundaries, is a superset of the model used by (Fedkiw et al., 2001) for smoke simulation. While it may not execute in real time, GPU simulation is likely faster than simulation on the CPU. More research into GPU techniques for simulating dynamic phenomena such as fluids is needed.



# Bibliography

- Andrews, D. G. (2000). *An Introduction to Atmospheric Physics*. Cambridge University Press, Cambridge.
- ATI Technologies, Inc. (2003). *ATI Radeon 9800*.  
<http://www.ati.com/products/radeon9800/radeon9800pro/index.html>.
- Bhate, N. and Tokuta, A. (1992). Photorealistic volume rendering of media with directional scattering. In *Proceedings of the 3rd Eurographics Workshop on Rendering*, pages 227–245.
- Blasi, P., Le Saëc, B., and Schlick, C. (1993). A rendering algorithm for discrete volume density objects. In *Proceedings of Eurographics 1993*, pages 201–210.
- Blinn, J. F. (1982a). A generalization of algebraic surface drawing. In *Proceedings of SIGGRAPH 1982*, pages 273–274.
- Blinn, J. F. (1982b). Light reflection functions for simulation of clouds and dusty surfaces. In *Proceedings of SIGGRAPH 1982*, Computer Graphics, pages 21–29.
- Bohn, C.-A. (1998). Kohonen feature mapping through graphics hardware. In *Proceedings of the 3rd Int. Conference on Computational Intelligence and Neurosciences*.
- Bohren, C. F. (1987). Multiple scattering of light and some of its observable consequences. *American Journal of Physics*, 55(6):524–533.
- Bolz, J., Farmer, I., Grinspun, E., and Schröder, P. (2003). Sparse matrix solvers on the GPU: Conjugate gradients and multigrid. In *Proceedings of SIGGRAPH 2003*, pages 917–924.
- Briggs, W. L., Henson, V. E., and McCormick, S. F. (2000). *A Multigrid Tutorial, Second Edition*. SIAM, second edition.
- Cabral, B., Cam, N., and Foran, J. (1994). Accelerated volume rendering and tomographic reconstruction using texture mapping hardware. In *Proceedings of the 1994 Symposium on Volume Visualization*, pages 91–98.
- Carr, N. A., Hall, J. D., and Hart, J. C. (2002). The ray engine. In *Proceedings of the ACM SIGGRAPH/EUROGRAPHICS conference on Graphics hardware*, pages 37–46.
- Carr, N. A., Hall, J. D., and Hart, J. C. (2003). GPU algorithms for radiosity and subsurface scattering. In *Proceedings of the ACM SIGGRAPH/EUROGRAPHICS conference on Graphics hardware*, pages 51–59.

- Chandrasekhar, S. (1960). *Radiative Transfer*. Dover, New York.
- Chenney, S. and Forsyth, D. (1997). View dependent culling of dynamic systems in virtual environments. In *Proceedings of the 1997 symposium on Interactive 3D graphics*, pages 55–58.
- Chorin, A. J. and Marsden, J. E. (1993). *A Mathematical Introduction to Fluid Mechanics, Third Edition*. Springer, New York.
- Cohen, M. F. and Wallace, J. R. (1993). *Radiosity and Realistic Image Synthesis*. Morgan Kaufmann.
- Coombe, G., Harris, M. J., and Lastra, A. (2003). Radiosity on graphics hardware. Technical Report TR03-020, University of North Carolina.
- Cornette, W. and Shanks, J. (1992). Physically reasonable analytic expression for the single-scattering phase function. *Applied Optics*, 31:3152–3160.
- Dobashi, Y., Kaneda, K., Yamashita, H., Okita, T., and Nishita, T. (2000). A simple, efficient method for realistic animation of clouds. In *Proceedings of SIGGRAPH 2000*, pages 19–28.
- Dobashi, Y., Nishita, T., Yamashita, H., and Okita, T. (1999). Using metaballs to model and animate clouds from satellite images. *The Visual Computer*, 15:471–482.
- Eberly, D. H. (2001). *3D Game Engine Design*. Morgan Kaufmann Publishers.
- Ebert, D. S. (1997). Volumetric modeling with implicit functions: a cloud is born. In *ACM SIGGRAPH 97 Visual Proceedings: The art and interdisciplinary programs of SIGGRAPH '97*, page 245.
- Ebert, D. S., Musgrave, F. K., Peachey, D., Perlin, K., and Worley, S. (2002). *Texturing & Modeling: A Procedural Approach, Third Edition*. Morgan Kaufman.
- Ebert, D. S. and Parent, R. E. (1990). Rendering and animation of gaseous phenomena by combining fast volume and scanline A-buffer techniques. In *Proceedings of SIGGRAPH 1990*, pages 357–366.
- Elinas, P. and Stürzlinger, W. (2001). Real-time rendering of 3D clouds. *The Journal of Graphics Tools*, 5(4):33–45.
- England, J. N. (1978). A system for interactive modeling of physical curved surface objects. In *Proceedings of SIGGRAPH 1978*, pages 336–340.
- Eyles, J., Molnar, S., Poulton, J., Greer, T., and Lastra, A. (1997). Pixelflow: The realization. In *Proceedings of the ACM SIGGRAPH/EUROGRAPHICS workshop on Graphics hardware*, pages 57–68.

- Fedkiw, R., Stam, J., and Jensen, H. W. (2001). Visual simulation of smoke. In *Proceedings of SIGGRAPH 2001*, pages 15–22.
- Fernando, R., editor (2004). *GPU Gems: Programming Techniques, Tips and Tricks for Real-Time Graphics*. Addison Wesley Professional.
- FlightGear (2003). *FlightGear Flight Simulator*. <http://www.flightgear.org/>.
- Foster, N. and Metaxas, D. (1997). Modeling the motion of a hot, turbulent gas. In *Proceedings of SIGGRAPH 1997*, pages 181–188.
- Gardner, G. Y. (1985). Visual simulation of clouds. In *Proceedings of SIGGRAPH 1985*, pages 297–303.
- Golub, G. H. and Van Loan, C. F. (1996). *Matrix Computations, Third Edition*. The Johns Hopkins University Press, Baltimore.
- Goodnight, N., Woolley, C., Lewin, G., Luebke, D., and Humphreys, G. (2003). A multigrid solver for boundary value problems using graphics hardware. In *Proceedings of the ACM SIGGRAPH/EUROGRAPHICS conference on Graphics hardware*, pages 102–111.
- Govindaraju, N., Redon, S., Lin, M. C., and Manocha, D. (2003). Cullide: Interactive collision detection between complex models in large environments using graphics hardware. In *Proceedings of the ACM SIGGRAPH/EUROGRAPHICS conference on Graphics hardware*, pages 25–32.
- Griebel, M., Dornseifer, T., and Neunhoeffer, T. (1998). *Numerical Simulation in Fluid Dynamics : A Practical Introduction*. SIAM Monographs on Mathematical Modeling and Computation. Society for Industrial and Applied Mathematics, Philadelphia.
- Guha, S., Krishnan, S., Munagala, K., and Venkatasubramanian, S. (2003). Application of the two-sided depth test to CSG rendering. In *Proceedings of the 2003 symposium on Interactive 3D graphics*, pages 177–180.
- Hamblyn, R. (2001). *The Invention of Clouds*. Picador USA.
- Harris, M. J. (2002a). Analysis of error in a CML diffusion operation. Technical Report TR02-015, University of North Carolina.
- Harris, M. J. (2002b). Implementation of a CML boiling simulation using graphics hardware. Technical Report TR02-016, University of North Carolina.
- Harris, M. J., Baxter, W. V., Scheuermann, T., and Lastra, A. (2003). Simulation of cloud dynamics on graphics hardware. In *Proceedings of the ACM SIGGRAPH/EUROGRAPHICS conference on Graphics hardware*, pages 92–101.

- Harris, M. J., Coombe, G., Scheuermann, T., and Lastra, A. (2002). Physically-based visual simulation on graphics hardware. In *Proceedings of the ACM SIGGRAPH/EUROGRAPHICS conference on Graphics hardware*, pages 109–118.
- Harris, M. J. and James, G. (2003). Simulation and animation using hardware accelerated procedural textures. In *Proceedings of Game Developers Conference 2003*.
- Harris, M. J. and Lastra, A. (2001). Real-time cloud rendering. In *Proceedings of Eurographics 2001*, pages 76–84.
- Heidrich, W., Westermann, R., Seidel, H.-P., and Ertl, T. (1999). Applications of pixel textures in visualization and realistic image synthesis. In *Proceedings of the 1999 symposium on Interactive 3D graphics*, pages 127–134.
- Henyey, L. and Greenstein, J. (1941). Diffuse radiation in the galaxy. *The Astrophysical Journal*, 90:70–83.
- Hillesland, K., Molinov, S., and Grzeszczuk, R. (2003). Nonlinear optimization framework for image-based modeling on programmable graphics hardware. In *Proceedings of SIGGRAPH 2003*, pages 925–934.
- Hoff, K. E., Culver, T., Keyser, J., Lin, M., and Manocha, D. (1999). Fast computation of generalized voronoi diagrams using graphics hardware. In *Proceedings of SIGGRAPH 1999*, pages 277–286.
- Hoff, K. E., Zaferakis, A., Lin, M., and Manocha, D. (2001). Fast and simple 2D geometric proximity queries using graphics hardware. In *Proceedings of the 2001 Symposium on Interactive 3D Graphics*, pages 145–148.
- Houze, R. (1993). *Cloud Dynamics*. International Geophysics Series. Academic Press, San Diego.
- Howard, L. (1804). *On the Modifications of Clouds*. J. Taylor, London.
- iROCK Games (2002). *Savage Skies*. Bam! Entertainment.
- James, G. (2001a). *NVIDIA Game Of Life Demo*.  
[http://developer.nvidia.com/view.asp?IO=ogl\\_gameoflife](http://developer.nvidia.com/view.asp?IO=ogl_gameoflife).
- James, G. (2001b). *NVIDIA Procedural Texture Physics Demo*.  
[http://developer.nvidia.com/view.asp?IO=ogl\\_dynamic\\_bumpreflection](http://developer.nvidia.com/view.asp?IO=ogl_dynamic_bumpreflection).
- James, G. (2001c). Operations for hardware-accelerated procedural texture animation. In Deloura, M., editor, *Game Programming Gems 2*, pages 497–509. Charles River Media.

- Jensen, H. W. (1996). Global illumination using photon maps. In *Proceedings of the 7th Eurographics Workshop on Rendering*, pages 21–30.
- Jensen, H. W. and Christensen, P. H. (1998). Efficient simulation of light transport in scenes with participating media using photon maps. In *Proceedings of SIGGRAPH 1998*, pages 311–320.
- Jobard, B., Erlebacher, G., and Hussaini, M. Y. (2001). Lagrangian-eulerian advection for unsteady flow visualization. In *Proceedings of IEEE Visualization 2001*.
- Kajiya, J. T. and Von Herzen, B. P. (1984). Ray tracing volume densities. In *Proceedings of SIGGRAPH 1984*, pages 165–174.
- Kaneko, K., editor (1993). *Theory and applications of coupled map lattices*. Nonlinear Science: theory and applications. Wiley.
- Kapral, R. (1993). Chemical waves and coupled map lattices. In Kaneko, K., editor, *Theory and Applications of Coupled Map Lattices*, pages 135–168. Wiley.
- Kedem, G. and Ishihara, Y. (1999). Brute force attack on UNIX passwords with SIMD computer. In *Proceedings of The 8th USENIX Security Symposium*.
- Kim, T. and Lin, M. C. (2003). Visual simulation of ice crystal growth. In *Proceedings of the 2003 ACM SIGGRAPH/Eurographics Symposium on Computer Animation*, pages 86–97.
- Klassen, R. V. (1987). Modeling the effect of the atmosphere on light. *ACM Transactions on Graphics*, 6(3):215–237.
- Kniss, J., Premože, S., Hansen, C., and Ebert, D. S. (2002). Interactive translucent volume rendering and procedural modeling. In *Proceedings of IEEE Visualization 2002*, pages 109–116.
- Krishnan, S., Mustafa, N. H., and Venkatasubramanian, S. (2002). Hardware-assisted computation of depth contours. In *Proceedings of the thirteenth annual ACM-SIAM symposium on Discrete algorithms*.
- Krüger, J. and Westermann, R. (2003). Linear algebra operators for GPU implementation of numerical algorithms. In *Proceedings of SIGGRAPH 2003*.
- Lacroute, P. and Levoy, M. (1994). Fast volume rendering using a shear-warp factorization of the viewing transformation. In *Proceedings of SIGGRAPH 1994*, pages 451–458.
- Larsen, E. S. and McAllister, D. K. (2001). Fast matrix multiplies using graphics hardware. In *Proceedings of the 2001 ACM/IEEE conference on Supercomputing (CDROM)*.

- Laven, P. (2003). *MiePlot Software*. <http://philiplaven.com/MiePlot.htm>.
- Lee, K. J., McCormick, W. D., Ouyang, Q., and Swinn, H. L. (1993). Pattern formation by interacting chemical fronts. *Science*, 261:192–194.
- Lefohn, A. E., Kniss, J., Hansen, C., and Whitaker, R. T. (2003). Interactive deformation and visualization of level set surfaces using graphics hardware. In *Proceedings of IEEE Visualization 2003*.
- Lefohn, A. E. and Whitaker, R. T. (2002). A GPU-based, three-dimensional level set solver with curvature flow. Technical Report UUCS-02-017, University of Utah.
- Lengyel, J., Reichert, M., Donald, B. R., and Greenberg, D. P. (1990). Real-time robot motion planning using rasterizing computer graphics hardware. In *Proceedings of SIGGRAPH 1990*, pages 327–335.
- Levoy, M. (1988). Display of surfaces from volume data. *IEEE Computer Graphics & Applications*, 8(3):29–37.
- Lewis, J. P. (1989). Algorithms for solid noise synthesis. In *Proceedings of SIGGRAPH 1989*, pages 263–270.
- Li, W., Wei, X., and Kaufman, A. (2003). Implementing lattice boltzmann computation on graphics hardware. Technical Report 010416, State University of New York at Stony Brook.
- Lindholm, E., Kilgard, M., and Moreton, H. (2001). A user programmable vertex engine. In *Proceedings of SIGGRAPH 2001*, pages 149–158.
- Maciel, P. W. C. and Shirley, P. (1995). Visual navigation of large environments using textured clusters. In *Proceedings of the 1995 symposium on Interactive 3D graphics*, pages 95–ff.
- Mark, W. R., Glanville, R. S., Akeley, K., and Kilgard, M. J. Cg: A system for programming graphics hardware in a C-like language. In *Proceedings of SIGGRAPH 2003*, pages 896–907.
- Max, N. (1994). Efficient light propagation for multiple anisotropic volume scattering. In *Proceedings of the 5th Eurographics Workshop on Rendering*, pages 87–104.
- Max, N. (1995). Optical models for direct volume rendering. *IEEE Transactions on Visualization and Computer Graphics*, 1(2):99–108.
- Microsoft (2003). *DirectX API*. <http://www.microsoft.com/directx>.
- Mie, G. (1908). Bietage zur optik truver medien speziell kolloidaler metallosungen. *Annallen der Physik*, 25(3):377.

- Miyazaki, R., Yoshida, S., Dobashi, Y., and Nishita, T. (2001). A method for modeling clouds based on atmospheric fluid dynamics. In *Proceedings of Pacific Graphics 2001*, pages 363–372.
- Mustafa, N. H., Koutsofios, E., Krishnan, S., and Venkatasubramanian, S. (2001). Hardware assisted view dependent map simplification. In *Proceedings of the 17th Annual Symposium on Computational Geometry*.
- Nagel, K. and Raschke, E. (1992). Self-organizing criticality in cloud formation? *Physica A*, 182:519–531.
- Neyret, F. (1997). Qualitative simulation of cloud formation and evolution. In *Proceedings of the 8th Eurographics Workshop on Computer Animation and Simulation*, pages 113–124.
- Neyret, F. (2003). Advection textures. In *Proceedings of the 2003 ACM SIGGRAPH/Eurographics Symposium on Computer Animation*, pages 147–153.
- Nishimori, H. and Ouchi, N. (1993). Formation of ripple patterns and dunes by wind-blown sand. *Physical Review Letters*, 71(1):197–200.
- Nishita, T., Dobashi, Y., and Nakamae, E. (1996). Display of clouds taking into account multiple anisotropic scattering and sky light. In *Proceedings of SIGGRAPH 1996*, pages 379–386.
- NVIDIA Corporation (2001). *GeForce 3*. <http://www.nvidia.com/page/ geforce3.html>.
- NVIDIA Corporation (2002a). *GeForce 4 Ti*.  
<http://www.nvidia.com/page/ geforce4ti.html>.
- NVIDIA Corporation (2002b). *NVIDIA OpenGL Extension Specifications*.  
[http://developer.nvidia.com/view.asp?IO=nvidia\\_opengl\\_specs](http://developer.nvidia.com/view.asp?IO=nvidia_opengl_specs).
- NVIDIA Corporation (2003). *GeForce FX*.  
[http://www.nvidia.com/page/fx\\_desktop.html](http://www.nvidia.com/page/fx_desktop.html).
- Olano, M. and Lastra, A. (1998). A shading language on graphics hardware: The pixelflow shading system. In *Proceedings of SIGGRAPH 1998*, pages 159–168.
- Overby, D., Melek, Z., and Keyser, J. (2002). Interactive physically-based cloud simulation. In *Proceedings of Pacific Graphics 2002*, pages 469–470.
- Patmore, C. (1993). Simulated multiple scattering for cloud rendering. In *Graphics, Design and Visualization, Proceedings of the IFIP TC5/WG5.2/WG5.10 CSI International Conference on Computer Graphics*, pages 29–40.
- Pearson, J. E. (1993). Complex patterns in a simple system. *Science*, 261:189–192.

- Peercy, M. S., Olano, M., Airey, J., and Ungar, P. J. (2000). Interactive multi-pass programmable shading. In *Proceedings of SIGGRAPH 2000*, pages 425–432.
- Perlin, K. (1985). An image synthesizer. In *Proceedings of SIGGRAPH 1985*, pages 287–296.
- Perlin, K. and Neyret, F. (2001). Flow noise. In *SIGGRAPH 2001 Technical Sketches and Applications*, page 187.
- Poddar, B. and Womack, P. (2001). *WGL\_ARB\_render\_texture OpenGL extension specification*.  
[http://oss.sgi.com/projects/ogl-sample/registry/ARB/wgl\\_render\\_texture.txt](http://oss.sgi.com/projects/ogl-sample/registry/ARB/wgl_render_texture.txt).
- Potmesil, M. and Hoffert, E. M. (1989). The pixel machine: A parallel image computer. In *Proceedings of SIGGRAPH 1989*, pages 69–78.
- Premož, S., Harris, M. J., Hoffman, N., and Preetham, A. J. (2003). Light and color in the outdoors. In *SIGGRAPH 2003 Course Notes (#1)*.
- Proudfoot, K., Mark, W. R., Tzvetkov, S., and Hanrahan, P. (2001). A real-time procedural shading system for programmable graphics hardware. In *Proceedings of SIGGRAPH 2001*, pages 159–170.
- Purcell, T. J., Buck, I., Mark, W. R., and Hanrahan, P. (2002). Ray tracing on programmable graphics hardware. In *Proceedings of SIGGRAPH 2002*, pages 703–712.
- Purcell, T. J., Donner, C., Cammarano, M., Jensen, H. W., and Hanrahan, P. (2003). Photon mapping on programmable graphics hardware. In *Proceedings of the ACM SIGGRAPH/EUROGRAPHICS conference on Graphics hardware*, pages 41–50.
- Qian, Y., Succi, S., and Orszag, S. (1996). Recent advances in lattice boltzmann computing. In Stauffer, D., editor, *Annual Reviews of Computational Physics III*, pages 195–242. World Scientific.
- Reeves, W. (1983). Particle systems—a technique for modeling a class of fuzzy objects. In *Proceedings of SIGGRAPH 1983*, pages 359–375.
- Reeves, W. and Blau, R. (1985). Approximate and probabilistic algorithms for shading and rendering structured particle systems. In *Proceedings of SIGGRAPH 1985*, pages 313–322.
- Rhoades, J., Turk, G., Bell, A., State, A., Neumann, U., and Varshney, A. (1992). Real-time procedural textures. In *Proceedings of the 1992 Symposium on Interactive 3D Graphics*, pages 95–100.

- Rogers, R. R. and Yau, M. K. (1989). *A Short Course in Cloud Physics, Third Edition*. International Series in Natural Philosophy. Butterworth Heinemann, Burlington, MA.
- Rushmeier, H. E. and Torrance, K. E. (1987). The zonal method for calculating light intensities in the presence of a participating medium. In *Proceedings of SIGGRAPH 1987*, pages 293–302.
- Schaufler, G. (1995). Dynamically generated impostors. In *Proceedings of the GI Workshop “Modeling—Virtual Worlds—Distributed Graphics”*, pages 129–135.
- Schpok, J., Simons, J., Ebert, D. S., and Hansen, C. (2003). A real-time cloud modeling, rendering, and animation system. In *Proceedings of the 2003 ACM SIGGRAPH/Eurographics Symposium on Computer Animation*, pages 160–166.
- Segal, M. and Akeley, K. (2001). *The OpenGL Graphics System: A Specification (Version 1.3)*. <http://www.opengl.org>.
- Shade, J., Lischinski, D., Salesin, D. H., DeRose, T., and Snyder, J. (1996). Hierarchical image caching for accelerated walkthroughs of complex environments. In *Proceedings of SIGGRAPH 1996*, pages 75–82.
- Srivastava, R. (1967). A study of the effect of precipitation on cumulus dynamics. *Journal of Atmospheric Science*, 24:36–45.
- Stam, J. (1995). Multiple scattering as a diffusion process. In *Proceedings of the 6th Eurographics Workshop on Rendering*, pages 41–50.
- Stam, J. (1999). Stable fluids. In *Proceedings of SIGGRAPH 1999*, pages 121–128.
- Stam, J. (2003). Real-time fluid dynamics for games. In *Proceedings of the Game Developers Conference*.
- Steiner, J. (1973). A three-dimensional model of cumulus cloud development. *Journal of Atmospheric Science*, 30:414–435.
- Stewart, N., Leach, G., and John, S. (2003). Improved CSG rendering using overlap graph subtraction sequences. In *Proceedings of the International Conference on Computer Graphics and Interactive Techniques in Australasia and South East Asia (GRAPHITE 2003)*, pages 47–53.
- Strutt, J. W. (1871). On the light from the sky, its polarization and colour. *Philos. Mag.*, 41:107–120, 274–279.
- Strzodka, R. (2002). Virtual 16 bit precise operations on RGBA8 textures. In *Proceedings of Vision, Modeling, and Visualization*.

- Strzodka, R. and Rumpf, M. (2001). Level set segmentation in graphics hardware. In *Proceedings of the International Conference on Image Processing*.
- Takeda, T. (1971). Numerical simulation of a precipitating convective cloud: the formation of a “long-lasting” cloud. *Journal of Atmospheric Science*, 28:350–376.
- Thompson, C. J., Hahn, S., and Oskin, M. (2002). Using modern graphics architectures for general-purpose computing: A framework and analysis. In *Proceedings of the International Symposium on Microarchitecture (IEEE MICRO)*, pages 306–320.
- Toffoli, T. and Margolus, N. (1987). *Cellular Automata Machines*. The MIT Press, Cambridge, Massachusetts.
- Trendall, C. and Steward, A. J. (2000). General calculations using graphics hardware, with applications to interactive caustics. In *Proceedings of the Eurographics Workshop on Rendering*, pages 287–298.
- Turing, A. M. (1952). The chemical basis of morphogenesis. *Transactions of the Royal Society of London*, (B237):37–72.
- Turk, G. (1991). Generating textures on arbitrary surfaces using reaction-diffusion. In *Proceedings of SIGGRAPH 1991*, pages 289–298.
- van de Hulst, H. (1981). *Light Scattering by Small Particles*. Dover.
- Veach, E. (1997). *Robust Monte Carlo Methods for Light Transport Simulation*. Ph.d. dissertation, Stanford University.
- von Neumann, J. (1966). *Theory of Self-Reproducing Automata*. University of Illinois Press. Edited and completed by A.W. Burks.
- Weiskopf, D., Hopf, M., and Ertl, T. (2001). Hardware-accelerated visualization of time-varying 2D and 3D vector fields by texture advection via programmable per-pixel operations. In *Proceedings of Vision, Modeling, and Visualization*, pages 439–446.
- Weisstein, E. W. (1999). *CRC Concise Encyclopedia of Mathematics*. CRC Press.
- Westover, L. (1990). Footprint evaluation for volume rendering. In *Proceedings of SIGGRAPH 1990*, pages 367–376.
- Wilson, O., Van Gelder, A., and Wilhelms, J. (1994). Direct volume rendering via 3D textures. Technical Report UCSC-CRL-94-19, University of California at Santa Cruz.

- Witkin, A. and Kass, M. (1991). Reaction-diffusion textures. In *Proceedings of SIGGRAPH 1991*, pages 299–308.
- Wojnaroski, J. (2003). Personal communication.
- Wolfram, S. (1984). Cellular automata as models of complexity. *Nature*, (311):419–424.
- Yanagita, T. (1992). Phenomenology of boiling: A coupled map lattice model. *Chaos*, 2(3):343–350.
- Yanagita, T. and Kaneko, K. (1993). Coupled map lattice model for convection. *Physics Letters A*, 175:415–420.
- Yanagita, T. and Kaneko, K. (1997). Modeling and characterization of cloud dynamics. *Physical Review Letters*, 78(22):4297–4300.
- Yang, R., Welch, G., and Bishop, G. (2002). Real-time consensus-based scene reconstruction using commodity graphics hardware. In *Proceedings of Pacific Graphics 2002*.